Assen Zlatarov University
Burgas, Bulgaria

ANNUAL

VOLUME L, BOOK 1, 2021

TECHNICAL AND NATURAL SCIENCES

ASSEN ZLATAROV UNIVERSITY
BURGAS, BULGARIA

ANNUAL

Vol. L, BOOK 1, 2021

TECHNICAL AND NATURAL SCIENCES

Assen Zlatarov University

ASSEN ZLATAROV UNIVERSITY
BURGAS, BULGARIA

ANNUAL

Vol. L, BOOK 1, 2021

TECHNICAL AND NATURAL SCIENCES

BURGAS ● 2021

VOLUME L (1). CONTENTS

PROBABLE ENVIRONMENTAL FATE OF BENZOTHIOPHENE AND ITS ASYMMETRIC DIBENZOTHIOPHENE ISOMERS

Yana Koleva, Viktoria Trifonova, Hristivelina Zhecheva
E-mail: *yanuriana@abv.bg*

ABSTRACT

Sulphur organic compounds are present in crude oil, and they cause many problems. They are deleterious to the refining of petroleum, because they poison catalysts and cause corrosion. Noxious sulphur dioxide is produced during the combustion of sulphur-containing fuels. They are toxic and some of them are suspected mutagens and/or carcinogens. Better knowledge of the forms in which sulphur occurs in fossil fuels might aid the development of methods for its removal. The aim of this work was to predict the environmental fate of benzothiophene and its derivatives (asymmetric dibenzothiophene isomers) using the CompTox Chemistry Dashboard.

Key words: *benzothiophene, asymmetric dibenzothiophene isomer, environmental fate, CompTox Chemistry Dashboard*

INTRODUCTION

In recent years, sulphur compounds produced in the production and use of fuels have gradually become one of the main pollutants which affect air quality. Sulphur compounds mainly exist in diesel oil in the form of derivatives of thiophene and benzothiophene (BT). Therefore, it is an important issue to reduce the content of sulphur-containing compounds such as thiophene, benzothiophene, dibenzothiophene (DBT) and 4,6-dimethyldibenzothiophene (DMDBT) to very low levels to prevent air pollution during the combustion of commercial diesel or gasoline [1].

Benzo[b]thiophene and dibenzothiophene, accompanied by their alkyl derivatives, are by far the most common aromatic sulphur compounds in crude oils and solvent extracts of many marine sedimentary rocks [2-5]. They have not been found in organisms and water column particulate matter and appear only in a steadily increasing concentration with organic matter (OM) maturation, attesting to their formation upon diagenesis/catagenesis. The abundance of benzo[b]thiophenes decreases at more advanced maturity, as they are replaced by dibenzothiophene and its alkyl derivatives [3, 4, 6, 7].

After anthropogenic chemicals have been utilized, they are disposed of and can enter the environment with possible detrimental effects on human and ecosystem health. The environmental fate of chemicals is not only relevant for existing (legacy) compounds [8] but also for the development of new compounds [9]. The main processes governing the fate of chemicals can be grouped as sorption, abiotic degradation, bioaccumulation and biodegradation, which depend on the chemical and biological species involved or environmental conditions applied. Of these fate processes, biodegradation is often the most important factor in removal, and hence, is considered important in design, development and registration of a chemical [10].
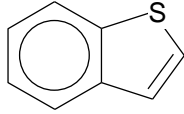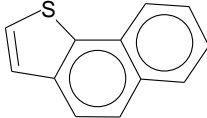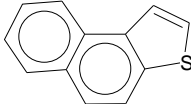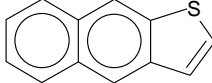
The aim of this work is to predict the environmental fate of benzothiophene and its derivatives (asymmetric dibenzothiophene isomers) using the CompTox Chemistry Dashboard.

EXPERIMENTAL

Compound. Benzothiophene and asymmetric dibenzothiophene isomers are by far the most common aromatic sulphur compounds in crude oils and solvent extracts of many marine sedimentary rocks [11]. Their CAS number, name of the compound and structural formulas are presented in Table 1 [12].

Table 1.CAS number, name and structural formula of benzothiophene and asymmetric dibenzothiophene isomers

No	CAS number	Name of compound	Structural formula
1	95-15-8	Benzo[b]thiophene	
2	234-41-3	Naphtho[1,2-b]thiophene	
3	233-02-3	Naphtho[2,1-b]thiophene	
4	268-77-9	Naphtho[2,3-b]thiophene	

CompTox Chemistry Dashboard. The Dashboard is a freely accessible web-based application and data hub providing access to data associated with chemical substances. It accesses data from nine component databases housing generic data types. The Dashboard also integrates data from other platforms (specifically PubChem and PubMed) via web services and visualization widgets. The Dashboard represents a first step in building a comprehensive chemical substance-centric informatics architecture to provide flexible access to data, models and analysis tools in support of EPA's research programs [13, 14].

Environmental fate and transport. The environmental fate and transport tab contains experimental and predicted properties sourced from online databases or predicted using EPI Suite, NICEATM, TEST and OPERA models. Included are properties such as the adsorption coefficient, atmospheric hydroxylation rate, biodegradation half-life, fish biotransformation half-life, as well as parameters to assess bioaccumulation potential, such as bioaccumulation factors (BAF) and bioconcentration factors (BCF). The properties are predominantly predicted values derived using OPERA models. EPI Suite models also are available for predicting bioconcentration and bioaccumulation factors, as well as the adsorption coefficient, and TEST and NICEATM models are available for predicting BCF. Experimental values for fish biotransformation half-life, BAF and BCF, were taken from the curated PHYSPROP database [13, 14].

RESULTS AND DISCUSSION

In the present work, the CompTox Chemistry Dashboard has been used to predict the environmental fate of benzothiphene and its three derivatives (asymmetric dibenzothiophene isomers).

The data of prediction (environmental fate) of benzo[b]thiophene are presented in Table 2.

Table 2. Several predicted properties for benzo[b]thiophene

Property	Experimental average	Predicted average	Experimental median	Predicted median	Experimental range	Predicted range	Unit
Bioconcentration Factor	750	63.3		63.3	750	22.3 to 104	-
Atmospheric Hydroxylation Rate	-	4.31e-11			-	4.31e-11	cm^3/molecule*sec
Biodegradation Half-Life	25.0	25.0		25.0	25.0	25.0	days
Fish Biotransformation Half-Life (Km)	-	0.237			-	0.237	days
Soil Adsorption Coefficient (Koc)	3.02e+3	3.01e+3			3.02e+3	3.01e+3	L/kg

There are experimental data of benzo [b] thiophene for Bioconcentration Factor (750), Biodegradation Half-Life (25.0) and Adsorption Coefficient (Koc) (3.02e+3). The bioconcentration factor of benzo [b] thiophene was predicted. The average value (22.3, 104, 63.3) is 63.3. Its median value is 63.3 and range is from 22.3 to 104. The Atmospheric Hydroxylation Rate of benzo [b] thiophene was predicted (predicted value is 4.31e-11 cm^3/molecule*sec) by OPERA. The biodegradation half-life of benzo [b] thiophene is estimated by OPERA. Its predicted value is 25.0 days (experimental average is 25.0). The property Fish biotransformation half-life (Km) of benzo[b]thiophene is estimated by OPERA. Its predicted value is 0.237 days. An OPERA model for determination of adsorption-coefficient (Koc) on soil for bexarotene is applied. Its predicted value is 3.01e+3 L/kg (experimental average is 3.02e+3 L/kg).

The data of prediction (environmental fate) of naphtho [1,2-b] thiophene are presented in Table 3.

There are no experimental data of naphtho [1,2-b] thiophene for all properties. The bioconcentration factor of naphtho [1,2-b] thiophene was predicted. The average value (118, 398, 258) is 258. Its median value is 258 and range is from 118 to 398. The Atmospheric Hydroxylation Rate of naphtho [1,2-b] thiophene was predicted (predicted value is 4.79e-11 cm^3/molecule*sec) by OPERA. The biodegradation half-life of naphtho [1,2-b] thiophene is estimated by OPERA. Its predicted value is 44.6 days. The property Fish biotransformation half-life (Km) of naphtho [1,2-b] thiophene is estimated by OPERA. Its predicted value is 0.344 days. An OPERA model for determination of adsorption-coefficient (Koc) on soil for naphtho [1,2-b] thiophene is applied. Its predicted value is 6.24e+3 L/kg.

The data of prediction (environmental fate) of naphtho [2,1-b] thiophene are presented in Table 4.

Table 3. Several predicted properties for naphtho [1,2-b] thiophene

Property	Experi-mental average	Pre dicted aver-age	Experi-mental me dian	Pre dicted me dian	Exper-imental range	Pre dicted range	Unit
Bioconcentra-tion Factor	-	258		258	-	118 to 398	-
Atmospheric Hydroxyla-tion Rate	-	4.79e-11			-	4.79e-11	cm^3/m ole-cule*s ec
Biodegrada-tion Half-Life	-	44.6			-	44.6	days
Fish Biotrans formation Half-Life (Km)	-	0.344			-	0.344	days
Soil Adsorp-tion Coeffi-cient (Koc)	-	6.24e+3			-	6.24e+3	L/kg

Table 4. Several predicted properties for naphtho [2,1-b] thiophene

Property	Experi-mental average	Pre dicted aver-age	Experi-mental me dian	Pre dicted me dian	Exper-imental range	Pre dicted range	Unit
Bioconcentra-tion Factor	-	286		286	-	223 to 349	-
Atmospheric Hydroxyla-tion Rate	-	4.77e-11			-	4.77e-11	cm^3/ mole-cule* sec
Biodegrada-tion Half-Life	-	38.7			-	38.7	days
Fish Biotrans formation Half-Life (Km)	-	0.344			-	0.344	days

| Soil Adsorption tion Coefficient (Koc) | - | 1.24e+4 | | | - | 1.24e+4 | L/kg |

There are no experimental data of naphtho [2,1-b] thiophene for all properties. The bioconcentration factor of naphtho [2,1-b] thiophene was predicted. The average value (223, 349, 286) is 286. Its median value is 286 and range is from 223 to 349. The Atmospheric Hydroxylation Rate of naphtho [2,1-b] thiophene was predicted (predicted value is 4.77e-11 cm^3/molecule*sec) by OPERA. The biodegradation half-life of naphtho [2,1-b] thiophene is estimated by OPERA. Its predicted value is 38.7 days. The property Fish biotransformation half-life (Km) of naphtho [2,1-b] thiophene is estimated by OPERA. Its predicted value is 0.344 days. An OPERA model for determination of adsorption-coefficient (Koc) on soil for naphtho[2,1-b]thiophene is applied. Its predicted value is 1.24e+4 L/kg.

The data of prediction (environmental fate) of naphtho [2,3-b] thiophene are presented in Table 5.

There are no experimental data of naphtho [2,3-b] thiophene for all properties. The bioconcentration factor of naphtho [2,3-b] thiophene was predicted. The average value (223, 265, 244) is 244. Its median value is 244 and range is from 223 to 265. The Atmospheric Hydroxylation Rate of naphtho [2,3-b] thiophene was predicted (predicted value is 4.77e-11 cm^3/molecule*sec) by OPERA. The biodegradation half-life of naphtho [2,3-b] thiophene is estimated by OPERA. Its predicted value is 29.5 days. The property Fish biotransformation half-life (Km) of naphtho [2,3-b] thiophene is estimated by OPERA. Its predicted value is 0.342 days. An OPERA model for determination of adsorption-coefficient (Koc) on soil for naphtho [2,3-b] thiophene is applied. Its predicted value is 1.28e+4 L/kg.

Table 5. Several predicted properties for naphtho[2,3-b]thiophene

Property	Experimental average	Predicted average	Experimental median	Predicted median	Experimental range	Predicted range	Unit
Bioconcentration Factor	-	244		244	-	223 to 265	-
Atmospheric Hydroxylation Rate	-	4.77e-11			-	4.77e-11	cm^3/molecule* sec
Biodegradation Half-Life	-	29.5			-	29.5	days
Fish Biotransformation Half-Life (Km)	-	0.342			-	0.342	days
Soil Adsorption Coefficient (Koc)	-	1.28e+4			-	1.28e+4	L/kg

CONCLUSION

The hazardous sulphur compounds are evolved from the sour crude oil or sour natural gas over an extended period of time, and the evolution of these compounds produces a serious environmental and safety problem. There are no experimental data about the environmental fate and transport of the benzothiophene derivatives (the asymmetric dibenzothiophene isomers) that are by far the most common aromatic sulphur compounds in crude oils. Therefore, alternative *In Silico* methods, such as the CompTox Chemistry Dashboard, are used to assess their toxicological behaviour.

ACKNOWLEDGEMENT

REFERENCES

1. Fallah R, et al. (2014). *Effect of aromatics on the adsorption of thiophenic sulphur compounds from model diesel fuel by activated carbon cloth*. Fuel Process Technol. 119:278–85.

2. Radke, M., D. Welte, H. Willsch (1986). *Maturity parameters based on aromatic hydrocarbons: Influence of the organic matter type*. In: Leythaeuser, D., Rullkoʼtter, J. (Eds.), Advances in Organic Geochemistry 1985, Organic Geochemistry 10, pp. 51–63.

3. Radke, M., H. Willsch (1991). *Occurrence and thermal evolution of methylated benzo- and dibenzothiophenes in petroleum source rocks of Western Germany*. In: Manning, D.A. (Ed.), Advances and Applications in Energy and the Natural Environment, Organic Geochemistry. Manchester University Press, pp. 480–484.

4. Radke, M., H. Willsch (1994). *Extractable alkyldibenzothiophenes in Posidonia Shale (Toarcian) source rocks: relationship of yields to petroleum formation and expulsion*. Geochimica et Cosmochimica Acta 58, pp.5223–5244.

5. Rospondek, M., J. de Leeuw, M. Baas, P. van Bergen, H. Leereveld (1994). *The role of organically bound sulphur in stratiform ore sulphide deposits*. Organic Geochemistry12, pp.1181–1191.

6. Orr, W. (1974). *Changes in sulphur content and isotopic ratios of sulphur during petroleum generation*. Study of Big Horn Palaeozoic oils. American Association of Petroleum Geologists' Bulletin 58, pp.2295–2318.

7. Santamariʼa-Orozco, D., B. Horsfield, R. di Primio, D. Welte (1998). *Influence of maturity on distributions of benzo- and dibenzothiophenes in Tithonian source rocks and crude oils*, Sonda de Campeche, Mexico. Organic Geochemistry 29, pp.423–439.

8. Amending Directives 2000/60/EC and 2008/105/EC as regards priority substances in the field of water policy (2012). European Commission. Directive of the European Parliament and of the Council: Brussels.

9. EMA, Guideline on the chemistry of active substances (2015). European Medicines Agency, Committee for Medicinal Products for Human Use (CHMP): London, United Kingdom.

10. Pavan, M. and A.P. Worth, Review of QSAR Models for Ready Biodegradation. 2006.

11. Rospondek, M. J., L. Marynowski, M. Gora (2007). *Novel arylatedpolyaromaticthiophenes: Phenylnaphtho[b]thiophenes and naphthylbenzo[b]thiophenes as markers of organic matter diagenesis buffered by oxidising solutions*, Organic Geochemistry 38, pp.1729–1756.

12. ChemIDplus Advanced: https://chem.nlm.nih.gov/chemidplus/.

13. USA EPA; CompTox Chemistry Dashboard:https://comptox.epa.gov/dashboard/

14. Williams et al. (2017). *The CompTox Chemistry Dashboard: a community data resource for environmental chemistry*, Journal of Cheminformatics 9: 61.

STATISTICAL ESTIMATION OF THE DAILY VALUES OF PM10 CONCENTRATIONS FOR THE MUNICIPALITY OF BURGAS

Zdravka Nikolaeva
E-mail: z.v.burieva@gmail.com

ABSTRACT

The article provides statistical processing and evaluation of daily data on the concentration of PM10 in the ambient air by calendar quarters for the automatic measuring station (AMS) in Dolno Ezerovo, 2020. An important problem for Burgas are the relatively high levels of this atmospheric pollutant, which is defined as very dangerous for the health of the population. Calculated are: mean, standard error, median, mode, standard deviation, sample variance, range, minimum and maximum value. A model for calculation of monthly concentrations is derived. The tests and inspections performed show that the tested modelling is suitable for evaluation, analysis and forecast.

Key words: *air pollution, PM10, statistical processing, regression analysis, coefficient of determination, F-statistics*

INTRODUCTION

Dust is a major atmospheric air pollutant. Its harmful health effect depends mainly on the size and chemical composition of the suspended dust particles.

The main sources of dust are the industry, transport and energy production. For the Municipality of Burgas, the pollution is from the loading and unloading activities of bulk cargo at the port of Burgas, the burning of solid fuels in the utilities sector during the heating seasons, road traffic and quarries for open pit mining [1, 2].

Preservation of clean air [3] is one of the most important tasks and a basic duty of the whole society and is based on the principles of sustainable development. As a member of the European Union, Bulgaria has fully synchronized the air requirements with the European directives [4 – 6].

The general condition of the atmospheric air is determined by means of the indicators in Art. 4 of the Clean Air Act [3]. Atmospheric air quality in the Municipality of Burgas [7] is calculated on the basis of six of the controlled air pollutants: nitrogen dioxide, sulfur dioxide, particulate matter, hydrogen sulfide, ozone and styrene.

The legislation on the environment in Bulgaria, which is fully synchronized with the European legislation and that on the atmospheric air, in particular, determines the norms for the protection of human health for each of these pollu-

tants. For PM10, the daily norm is 50 $\mu g/m^3$ and the annual rate is 40 $\mu g/m^3$.

The harmful effect of dust pollution is more pronounced in the simultaneous presence of sulfur dioxide in the air. Their synergistic effect on the respiratory organs and exposed mucous membranes has been established. Prolonged exposure to sulfur dioxide and dust is manifested by an increase in non-specific lung diseases, mainly respiratory infections of the upper respiratory tract and bronchitis – at significantly lower concentrations than 30 - 150 $\mu g/m^3$, which is particularly pronounced in children. Partivulary vulnerable to the combined effects of dust and sulfur dioxide are the people with chronic conditions, such as bronchial asthma and cardiovascular disease.

Recently, an important problem for the Municipality of Burgas is the relatively high levels of PM10, which is why it is necessary to deal with this important for the city atmospheric pollutant.

EXPERIMENT

The statistical processing of the database for the concentrations of PM10 in the atmospheric air was done with the help of the Excel software product [8]. The Descriptive Statistics module has a user-friendly interface and allows you to get results that describe the distribution without entering any formulas in the worksheet. The

module is entered with the command Tools / Data Analysis. It is only necessary to set the data area in the Input Range, to indicate where to get the results in the Output Range and to include the Summary Statistics field. Information about the location on the measuring scale is given by the measures of the central trend. The most commonly used measures of the central trend are: average, median, fashion. In relation to the scattering of the values of the variable in question, the most commonly used scattering measures are: range, variance and standard deviation.

To calculate the concentration of PM10, regression models of 9th order were developed, respectively:

$$y = b + a_1.x + a_2.x^2 + a_3.x^3 +$$
$$a_4.x^4 + a_5.x^5 + +a_6.x^6 + \quad , \quad (1)$$
$$+ a_7.x^7 + a_8.x^8 + a_9.x^9$$

where y is the average of monthly concentrations of PM10, $\mu g / m^3$; x is month of the year. The coefficients b and a_1, a_2, ... , a_9, involved in equations (1) are determined by regression analysis of the experimental data.

For estimation of the quality of the regression models, the coefficient of determination R^2 was used, which determines the degree of linear dependence between the regresses involved in the model and the initial value. The significance of R^2 was checked using the Fisher criterion [9, 10]

$$F = \frac{R^2}{\left(1 - R^2\right)} \cdot \frac{\left(N_1 - k\right)}{\left(k - 1\right)}, \quad (2)$$

where: k – number of the estimated parameters of the model; N_1 – the size of the sample of experimental data. The higher the calculated value of R^2, the more reliable the regression model is.

RESULTS AND DISCUSSION

For the statistical processing of the concentrations of PM10 by calendar quarters for the AMS in Dolno Ezerovo, Burgas, daily data for each month of 2020 were used. Calculated are: mean, standard error, median, mode, standard deviation, sample variance, range, minimum and maximum value.

Table 1 presents the statistical results obtained in the processing of the data for I - III months quarter, IV - VI months quarter, VII - IX months quarter and X - XII months quarter.

Table 1. Statistical results obtained in the processing of PM10 concentrations for AMS Dolno Ezerovo, Burgas Municipality, 2020

Statistical treatment	I - III quarter	IV - VI quarter	VII - IX quarter	X - XII quarter
Mean	53.46	31.00	31.50	40.47
Standard Error	3.52	1.12	0.73	1.61
Median	45.24	28.60	29.10	36.55
Mode	36.30	23.70	23.00	31.00
Standard Deviation	33.37	10.71	7.02	15.48
Sample Variance	1113.69	114.67	49.29	232.52
Minimum	18.8	17.20	20.30	15.20
Maximum	248.8	86.70	47.90	95.10
Sum	4811.8	2852.4	2897.6	3723.3
Count	90	92	92	92

Table 1 shows that the standard error of the mean is small (0.73 to 3.52). The standard deviation has quite large values for all four quarters, due to the rather wide range of PM10 concentrations. They are larger for the first and fourth quarters, due to the larger differences between the minimum and maximum temperatures (the range as a measure of dissipation is the largest). The same applies to the dispersion.

The higher values of the measured concentrations are for the colder months (heating seasons), when in the Dolno Ezerovo area there is a signif-

icant combustion of solid fuels in the utilities sector.

The frequency intervals of the measured PM10 concentrations for the four quarters were found by the methods of mathematical statistics (Table 2). The histogram of the frequency distribution is given in Fig. 1.

Table 2. Frequency distribution in PM10 concentration processing for AMS Dolno Ezerovo

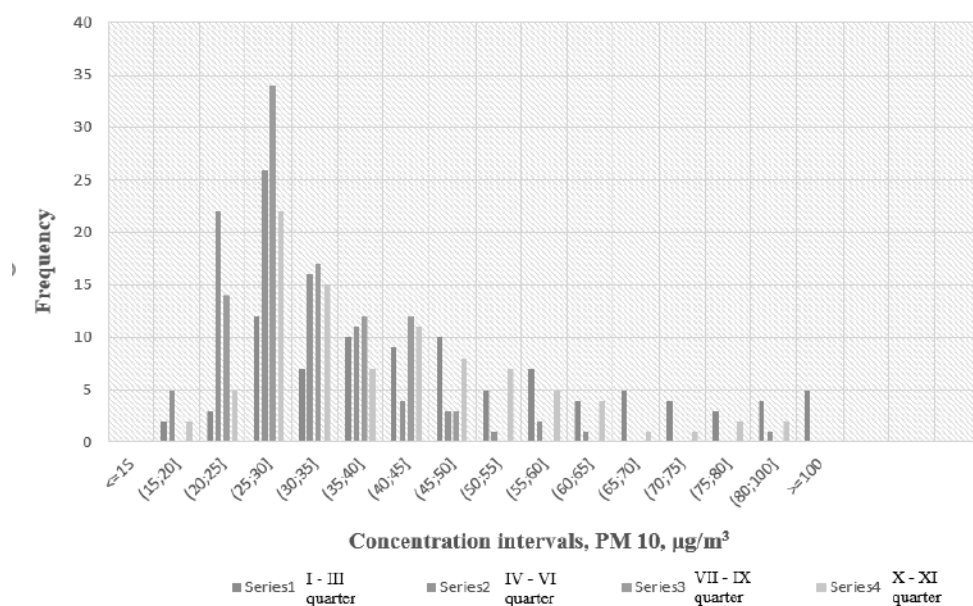| Upper limit of the interval	Interval	I - III quarter	IV - VI quarter	VII - IX quarter	X - XII quarter
15	<=15	0	0	0	0
20	(15;20]	2	5	0	2
25	(20;25]	3	22	14	5
30	**(25;30]**	**12**	**26**	**34**	**22**
35	(30;35]	7	16	17	15
40	(35;40]	10	11	12	7
45	(40;45]	9	4	12	11
50	(45;50]	10	3	3	8
55	(50;55]	5	1		7
60	(55;60]	7	2		5
65	(60;65]	4	1		4
70	(65;70]	5	0		1
75	(70;75]	4	0		1
80	(75;80]	3	0		2
100	(80;100]	4	1		2
	>=100	**5**			

Fig. 1. Histogram of the frequency distribution of PM10 concentrations by quarters for AMS Dolno Ezerovo

15

Table 2 and Fig. 1 show that the highest frequency of hits is for the interval [25; 30]: for I - III months quarter (12 hits), for IV – VI months quarter (26 hits), VII - IX months quarter (34 hits) and for X - XII months quarter (22 hits).

The measured daily concentrations of PM10 are mainly from (30 - 150 μg/m³). For the first quarter, very high values of the daily concentrations of 191.6 μg/m³ and 248.8 μg/m³ were observed, which are considered to be extremely unhealthy and dangerous to human health.

The derived regression model (1) for the arithmetic mean values of PM10 concentrations includes one factor – the month of the year. The coefficients b and a_1, a_2, ..., a_9 are determined using the Regression Statistics module of the Excel software product.

The regression equation is

$$y = 323.4 - 614.9.x + 546.1.x^2 - 259.4.x^3 + 72.9.x^4 - 12.8.x^5 + 1.407.x^6 - 0.0954.x^7 + 0.00364x^8 - (6.E - 05).x^9 \qquad (3)$$

Fig. 2 graphically compares the measured and predicted values of PM10 concentration for AMS Dolno Ezerovo according to model (3).

AMS Dolno Ezerovo, Burgas, 2020

y = 1x + 2E-10
$R^2 = 0.963$
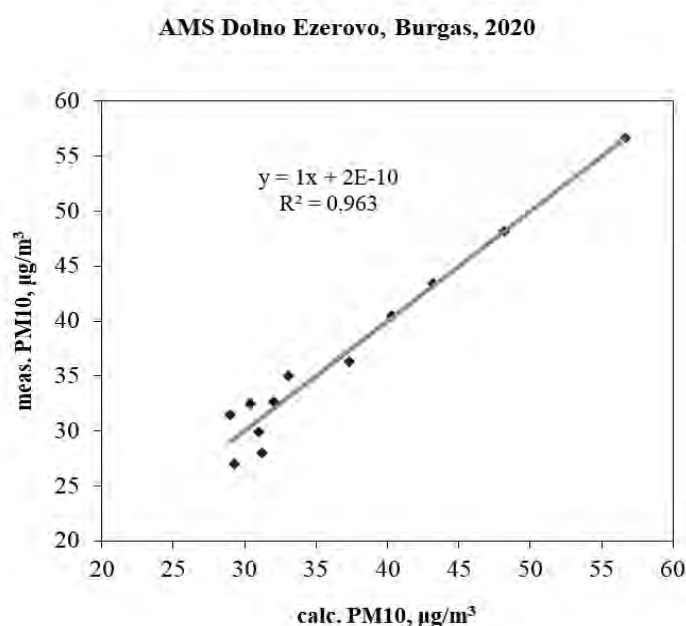
Fig. 2. Measured and predicted by model (3) values of PM10 concentration

Fig. 2 shows that the value of the coefficient of determination is very close to 1 ($R^2 = 0.963$), so it is assumed that the models are characterized by good quality and reliability.

Statistical and regression analysis and research can be applied to other pollutants (sulfur dioxide, ozone, etc.).

CONCLUSIONS

From the above results and discussion, it is concluded that:

Statistical processing of PM10 concentrations by calendar quarters was made for AMS Dolno Ezerovo, Burgas, 2020. The higher values of the measured concentrations are for the colder months (heating seasons), when in the Dolno Ezerovo area there is a significant combustion of solid fuels in municipal and household sectors.

The standard error of the mean is small (0.73 to 3.52); the standard deviation has quite large values for all four quarters, due to the rather wide range of PM10 concentrations. They are larger for the first and fourth quarters, due to the larger differences between the minimum and maximum temperatures (the range as a measure of dissipation is the largest). The same applies to the dispersion.

Using the methods of mathematical statistics, the frequency intervals of hits of the measured concentrations of PM10 for the four quarters were found. The highest frequency of hits is for

16

an interval [25; 30]. The measured daily concentrations of PM10 are mainly from (30 - 150 µg/m^3). For the first quarter very high values of the daily concentrations were observed, which are considered extremely unhealthy and dangerous.

A regression model for the arithmetic mean values of PM10 concentrations was derived. The measured and predicted values of PM10 concentration for AMS Dolno Ezerovo are compared and predicted according to model (3). Using Fisher's criterion, the coefficient of determination was found, which is very close to 1 ($R^2 = 0.963$). This shows that the models are characterized by good quality and reliability.

The method is convenient for estimating the concentration and pollution on a given day of the month, which can also be used for practical purposes (e.g. estimation of pollution in connection with the construction of photovoltaic systems).

REFERENCES

1. Dimov, A. and P. Toromanova. *Introduction to the Chemical and Metallurgical Technology and Ecology, Technics, Sofia, 1998.*
2. Kutsarov. *Air Pollution. Publishers "Prof. Dr. Assen Zlatarov" University, Burgas, (2001).*
3. *Air Act, Ministry of Environment and Water and Ministry of Health, last amended State Gazette, 3 January (2019).*
4. Nikolova, N. *Pollution and Monitoring of the Air. Pensoft, Sofia, (2008).*
5. Ljubojev, N., J. Veselinovic and M. Dukic-Mijatovic. *Protection of the Quality of Air in the Legislation of the Republic of Serbia as a Process of Harmonisation with the EU Legislation. Bulg. Oxid. Commun.*, **36** (4), p. 1217 (2013).
6. Air Quality Index (AQI), *A Guide to Air Quality and Your Health, US EPA, February (2014)*, https://www.airnow.gov/sites/default/files/2018-04/aqi_brochure_02_14_0.pdf.
7. *Air Quality in Burgas, Burgas Municipality*, http://air.burgas.bg.
8. *System for training in statistics and statistical calculations with Microsoft Excel, (2021|*, https://www.btu.bg/statexcel/
9. Kasarova, S., N. Sultanova, R. Kasarov, I. Nikolov. *Properties of polymeric materials for optical systems, Proc. SPIE*, **11047**, p. 110471I-1–110471I-8 (2019).
10. Kasarova, S., N. Sultanova, I. Nikolov, R. Kasarov. *Optical polymers in remote imaging devices*, *SES 2017 Proceedings,* p.354-359 (2017).

ADIABATIC THERMODYNAMIC MODEL FOR THE DESCRIPTION OF THE CURRENT STATE OF THE EXCESS CARBON DIOXIDE IN THE ATMOSPHERE

Mihai Petrov
E-mail: mihpetrov@abv.bg

ABSTRACT

The atmosphere, which is a complex component of the Earth's biosphere, is currently affected by complex changes as a result of intensive human activity and the technical and scientific progress. The widespread use of natural resources and especially carbon-containing fuel is resulting in the accumulation of excess carbon dioxide in the atmosphere and thus leading to the increase of the average temperature due to the greenhouse effect. If the density of the air is known and the molar fictive mass too, then the estimation of molar concentration of the air can be performed. If the molar fictive mass of the air is known respectively, then the calculation of the altitude of the troposphere can be performed and this calculated value is compared with the real one. This research applies empirically an adiabatic model with the respective equation of adiabatic process and then allows for quantitative estimation of the variation of the concentration of carbon dioxide. This variation of carbon dioxide influences the average temperature of the atmosphere and the final result is the increase of the environmental temperature. NASA's research registers both the values of the temperature and concentration of carbon dioxide. The suggested adiabatic model allows to obtain the expression of the variation of the temperature as a function of the variation of the concentration of carbon dioxide. The real values of temperatures registered by NASA are used for the validation of this adiabatic model. The re-calculation value of the adiabatic constant of air allows to confirm the validity of the application of this model. The application of barometric formula to the real values of pressure gives the re-calculation of the effective molar mass of air. The pressure at the null level is also calculated to be of the order of real one. The final aim of this paper is to obtain the empirical equation of the variation of the temperature as a function of the variation of the concentration of carbon dioxide and the results are compared with the real values.

Key words: adiabatic model, adiabatic constant, molar concentration, barometric formula, empirical expression

INTRODUCTION

The modern stage of life is determined by dynamic social changes and technical progress that lead to the changes in the composition of the biosphere and atmosphere as a result of the increased pollutant concentrations and, subsequently, to unpleasant consequences such as the disappearance of many marine and terrestrial species and weather anomalies. One of the pollutants is the accumulation of carbon dioxide in the atmosphere as a result of anthropogenic activity. This excess of carbon dioxide that accumulates in the atmosphere leads to the greenhouse effect with the subsequent increase of the average temperature of the environment and, respectively, to temperature anomalies. The increase of the concentration of carbon dioxide has the property to accumulate the excess of solar thermal energy. The thermodynamic adiabatic processes are used to empirically describe the respective equation that will give an expression of the temperature variation as a function of the variation of the concentration of carbon dioxide in the atmosphere.

EXPERIMENT

The composition of dry air is complex and it contains 78.08 % nitrogen, 20.95% oxygen, 0.93% argon, 0.04% carbon dioxide and small amounts of other gases [1]. The temperature of the troposphere is the highest near the surface of the Earth and decreases with altitude. The average temperature gradient of the troposphere is 6.5°C per 1000 m of altitude. An important pa-

rameter that describes the dependence of the temperature as the function of height is the rate $-\dfrac{dT}{dh}$, (h is the altitude). This rate is called the environmental lapse rate [2],[3],[4]. The ELR assumes that the air is perfectly still, i.e. there is no mixing of the layers of air from vertical convection and no winds that would create turbulences. The dry adiabatic lapse rate accounts for the effect of the expansion of dry air as it rises in the atmosphere and wet adiabatic lapse rates include the effect of the condensation of water steam on the lapse rate. Since the process of compression and expansion of an air parcel can be considered reversible and no energy is transferred into or out of the parcel, such a process is considered isentropic, meaning that there is no change in entropy as the air parcel rises and falls ($dS=0$). Since the heat exchanged ($dQ=0$) is related to the entropy change dS by $dQ=TdS$, then:

$$\frac{dS}{dh} = 0 \qquad (1)$$

where S is the entropy. The above equation states that the entropy does not change with height. The rate at which temperature decreases with height under such conditions is called the adiabatic lapse rate [5]. For dry air the adiabatic equation of the ideal gas is valid [6]:

$$P(h) \cdot \left[T(h)\right]^{-\frac{\gamma}{\gamma-1}} = const \qquad (2)$$

where γ is the adiabatic constant of the air ($\gamma \approx 7/5$). Combined with the equation for the pressure, the expression of dry adiabatic lapse rate is [7]:

$$\frac{dT}{dh} = -\frac{M \cdot g}{R} \cdot \frac{\gamma-1}{\gamma} = -9,8^0 C/km \qquad (3)$$

The pressure of the atmosphere has its maximum at sea level and decreases with altitude [8]. This is because the atmosphere is very nearly in hydrostatic equilibrium so that the pressure is equal to the weight of air above a given point. The change in pressure with altitude can be expressed by the density [9] as:

$$\frac{dP}{dh} = -\rho \cdot g = -\frac{M \cdot P \cdot g}{R \cdot T} \qquad (4)$$

where g is the gravitational acceleration; ρ is the density of air; h is the altitude; P is the pressure; R is the gas constant; T is the thermodynamic temperature; M is the molar mass.

This change in pressure (4) originates from the barometric formula of troposphere [10]:

$$P(h) = P_o \cdot e^{-\frac{M \cdot g \cdot h}{R \cdot T(h)}} \qquad (5)$$

Combining the expressions of adiabatic process (2) with (5), then:

$$P_o \cdot e^{-\frac{M \cdot g \cdot h}{R \cdot T}} \cdot \left[T(h)\right]^{-\frac{\gamma}{\gamma-1}} = const \qquad (6)$$

If the temperature depends on height, it will be better to obtain such an expression of the value of temperature that depends on height by applying (6):

$$\left[T(h)\right]^{-\frac{\gamma}{\gamma-1}} = \frac{const}{P_o} \cdot e^{\frac{Mgh}{RT(h)}} \qquad (7)$$

$$\left[T(h)\right]^{\frac{\gamma}{\gamma-1}} = \frac{P_o}{const \cdot e^{\frac{Mgh}{RT(h)}}} \qquad (8)$$

The procedure of natural logarithm of (8) gives:

$$\frac{\gamma}{\gamma-1} \cdot \ln[T(h)] = \ln P_o - \ln(const) - \frac{Mgh}{RT(h)} \qquad (9)$$

$$T(h) \cdot \ln[T(h)] = \frac{T(h) \cdot (\gamma-1)}{\gamma} \cdot (\ln P_o - \ln(const)) - \frac{Mg \cdot (\gamma-1)h}{R \cdot \gamma} \qquad (10)$$

$$\ln[T(h)] = \frac{(\gamma-1)}{\gamma} \cdot (\ln P_o - \ln(const)) - \frac{Mg \cdot (\gamma-1) \cdot h}{R \cdot \gamma \cdot T(h)} \qquad (11)$$

For the case where $h=0$, then $h/T=0$ and the expression (11) is:

$$\ln[T(0)] = \frac{(\gamma-1)}{\gamma} \cdot (\ln P_o - \ln(const)) \qquad (12)$$
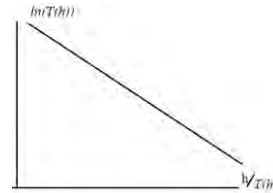
Fig.1 The dependence of $\ln[T(h)] = f\left(\dfrac{h}{T}\right)$

Thus, it would be possible to recalculate the temperature at the null level T(0) and also the molar mass M by the slope of this graphic.

The expression (12) could be applied for small altitudes. Then:

$$\ln T = \frac{(\gamma-1)}{\gamma} \cdot (\ln P - \ln(const)) \qquad (13)$$

In order to describe the increase of the temperature due to of the greenhouse effect, it will be better to differentiate the expression (13):

$$\frac{\Delta T}{T} = \left(\frac{\gamma-1}{\gamma}\right) \cdot \frac{\Delta P}{P} \qquad (14)$$

The respective expression of the equation of the state of ideal gas is:

$$P.V = \nu.R.T; \quad P = C.R.T ;$$

where C is the molar concentration of the mixture of gas of the atmospheric air.

The respective variation of pressure:

$$\Delta P = R \cdot (\Delta T.C + \Delta C.T) \qquad (15)$$

The substitution of (15) into (14) gives:

$$\frac{\Delta T}{T} = \left(\frac{\gamma - 1}{\gamma}\right) \cdot \frac{(C.\Delta T + T.\Delta C)}{C.R.T} =$$

$$= \left(\frac{\gamma - 1}{\gamma}\right)\left(\frac{\Delta T}{R.T} + \frac{\Delta C}{C.R}\right) = \left(\frac{\gamma - 1}{\gamma}\right)\frac{\Delta T}{R.T} + \left(\frac{\gamma - 1}{\gamma}\right) \cdot \frac{\Delta C}{C.R}$$

$$\Delta T = \left(\frac{\gamma - 1}{\gamma(R-1)+1}\right) \cdot \frac{\Delta C \cdot T}{C} \qquad (16)$$

The expression (15) shows quantitatively the increase of the temperature of the atmosphere with the increase of the molar concentration of greenhouse gases by the value ΔC.

The density of air at sea level is about 1.2 kg/m^3. The atmospheric density decreases as the altitude increases [11].

Then the molar concentration of the atmospheric air is calculated as:

$$C = \frac{\rho}{M} = \frac{1,2(kg/m^3)}{0,029(kg/mol)} = 41,37(mol/m^3) =$$

$$= 0,04137(mol/l)$$

The average mass of the atmosphere is about 5 quadrillion (5.13×10^{15}) tones or 1/1,200,000 the mass of Earth [10]. The mass of the atmosphere that is $5.13.10^{18}$ kg allows to calculate the full volume of the atmosphere - $V_{atm.}$:

$$V_{atm} = \frac{m_{atm}}{M \cdot C} = \frac{5,13.10^{18}(kg)}{0,029(kg/mol) \cdot 0,04137(mol/l)} =$$

$$= 4275,96.10^{18}(l) = 4275,96.10^{15}(m^3) = 4,28.10^{18}(m^3)$$

Then, we can easily calculate the height of the troposphere - h:

$$h = \frac{V_{atm}}{S_{Earth}} = \frac{4,28.10^{18}}{4.3,14.(6371.10^3)^2} =$$

$$8,39.10^{-9}.10^{18}.10^{-6} = 8,39.10^3(m) \cong 8,5(km)$$

The calculated value of molar concentration of air will be used to appreciate the change of the temperature as a result of the increase of greenhouse gases by the value ΔC.

In general, the average temperature of the atmospheric air has been increasing almost linearly for the last 50 years [12] (Fig. 2).
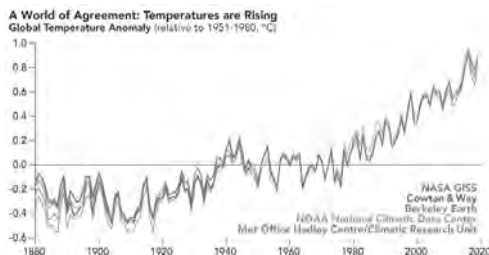

Fig. 2. The history of global change of temperature [13]

The opinions about the reasons for the increase in temperatures are various, but most observation focus on the increase of the concentration of carbon dioxide, which is a major greenhouse gas and has 75% effect of all others greenhouse gases [14]. The registration of the concentrations of carbon dioxide by satellites [14] is represented in Fig. 3.

The changes of temperature and concentration values which are described in the Fig. 2 and 3 can be included in expression (15) and the final result is the representation of the graphic $\Delta T=f(\Delta C)$ which, in general, is a linear dependence (Fig. 4)
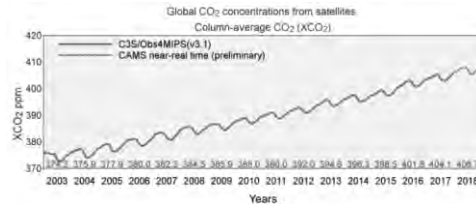
Fig. 3 The dynamics of the change of the concentration of CO_2 [14]
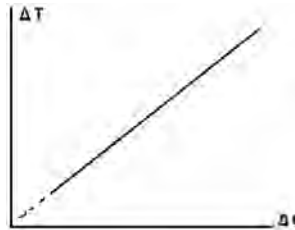
Fig. 4 The form of the dependence of $\Delta T=f(\Delta C)$

Thus, the slope of the dependence of $\Delta T=f(\Delta C)$ allows us to calculate the value of adiabatic constant γ. The numerical value of γ confirms the validity of the suggested quantitative expression of the temperature variation.

RESULTS AND DISCUSSION

The values of temperatures and of the pressure are changeable with the altitude. The following Table 1 shows the results [11] of the measurements of these values.

Table 1. The important parameters of the atmosphere as function of altitude [11]

Geo potential Altitude above Sea Level - h - (m)	Temperature - t - (°C)	Acceleration of Gravity - g - (m/s^2)	Absolute Pressure - p - (10^4 N/m^2)	Density - ρ - (kg/m^3)	Dynamic Viscosity - μ - (10^{-5} N s/m^2)
-1000	21.50	9.810	11.39	1.347	1.821
0	15.00	9.807	10.13	1.225	1.789
1000	8.50	9.804	8.988	1.112	1.758
2000	2.00	9.801	7.950	1.007	1.726
3000	-4.49	9.797	7.012	0.9093	1.694
4000	-10.98	9.794	6.166	0.8194	1.661
5000	-17.47	9.791	5.405	0.7364	1.628
6000	-23.96	9.788	4.722	0.6601	1.595
7000	-30.45	9.785	4.111	0.5900	1.561
8000	-36.94	9.782	3.565	0.5258	1.527
9000	-43.42	9.779	3.080	0.4671	1.493
10000	-49.90	9.776	2.650	0.4135	1.458

20

In order to validate expression (2) with the application of real values of the source [11], the following graphic $\ln[P(h)] = f(\ln[T(h)]$ is represented on Fig. 5. The procedure of natural logarithm of expression (2) is:

$$\ln\left[P(h) \cdot [T(h)]^{\frac{\gamma}{\gamma-1}} \right] = \ln[const];$$

$$\ln[P(h)] = \frac{\gamma}{\gamma-1} \cdot \ln[T(h)] + \ln[const]$$

The slope of this linear dependence allows to find the adiabatic constant γ of air.

Fig.5 The functional dependence
$\ln[P(h)] = f(\ln[T(h)]$

The correlation calculation of the linear dependence shows that

$$\frac{\gamma}{\gamma-1} = 5,2521 \Rightarrow \gamma = \frac{5,2521}{4,2521} \approx 1,23$$

The obtained result of the adiabatic constant of atmospheric air is of the same order as the results in the literature [15],[16]. In order to check the barometric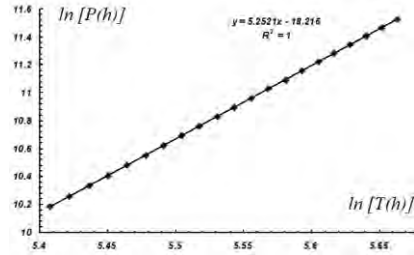 formula (5) for the tropospheric air it, would be better to represent this expression by the logarithm of this expression. The linear dependence will validate the expression of the barometric formula: $\ln[P(h)] = \ln[P_o] - \frac{M.g}{R.T}.h$. The graphic of $\ln[P(h)] = f(h)$ is represented in Fig. 6. The respective slope is: $\frac{M.g}{R.T} = 0,00012$. Then the calculation of the molar mass of tropospheric air is:

$$M = \frac{0,00012 \cdot 8,31 \cdot 288}{9,83} = 0,02921(kg/mole)$$

The calculated value of the molar mass of the tropospheric air is of the same order as in [11].
$\ln P_0 = 11,55 \Rightarrow P_0 = 103777(Pa) \approx 1,04 \cdot 10^5 (Pa)$
The obtained value of the pressure of the tropospheric air at the null level is of the same order as the value in Table 1 [11].

The graphic of $\ln[T(h)] = f(h/T)$ is represented in Fig. 7. The correlational calculations show that $\ln[T(0)] = \frac{(\gamma-1)}{\gamma} \cdot (\ln P_o - \ln(const)) = 5,6581$

$\ln[T(0)] = 5,6581; \quad T(0) = e^{5,6581} = 286,6(K)$;
The respective slope of the graphic is:
$$-\frac{Mg \cdot (\gamma-1)}{R \cdot \gamma} = -0,0057$$
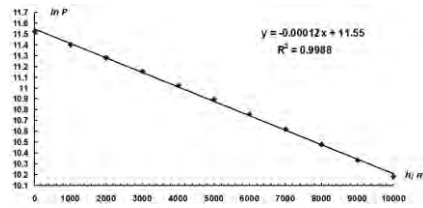
Fig. 6 The graphic of the dependence
$\ln[P(h)] = f(h)$

Then, we can easily recalculate the molar mass of the tropospheric air:

$$M = \frac{0,0057.R.\gamma}{g.(\gamma-1)} = \frac{0,0057 \cdot 8,31 \cdot 1,2}{9,83 \cdot 0,2} = 0,0289(kg/mol)$$

The suggested method of quantitative description of the variation of the atmospheric temperature ΔT with the increase of the concentration of greenhouse gas CO_2 can be checked by the following Table 2 whic is based on the results of the sources [13], [14].
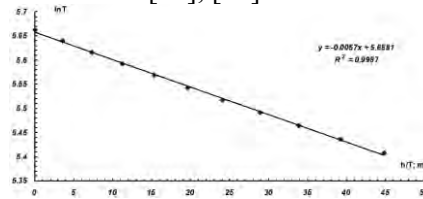
Fig. 7 The graphic of the dependence
$\ln[T(h)] = f(h/T)$

Table 2. The variation of temperature as a function of the increase of the concentration of CO_2

	year	ΔT; °C	C (CO_2); ppm	ΔC (CO_2); ppm	ΔC (CO_2); mg/m³
0	1980	0	338	0	0
1	1981	0.03	340	2	3.61
2	1982	0.05	341	3	5.41
3	1983	0.07	343	5	9.01
4	1984	0.09	345	7	12.63
5	1985	0.11	347	9	16.23
6	1986	0.13	348	10	18.03
7	1987	0.15	349	11	19.84
8	1988	0.18	350	12	21.64
9	1989	0.19	350.5	12.5	22.54
10	1990	0.22	351	13	23.44
11	1991	0.26	352	14	25.25
12	1992	0.32	353	15	27.05

13	1993	0.34	355	17	30.66
14	1994	0.36	357	19	34.26
15	1995	0.37	359	21	37.87
16	1996	0.39	360	22	39.67
17	1997	0.41	361	23	41.48
18	1998	0.42	362	24	43.28
19	1999	0.43	363	25	45.08
20	2000	0.45	365	27	48.69
21	2001	0.46	369	31	55.90
22	2002	0.47	373	35	63.12
23	2003	0.5	375	37	66.72
24	2004	0.54	376	38	68.52
25	2005	0.58	378	40	72.13
26	2006	0.59	379	41	73.93
27	2007	0.6	380	42	75.74
28	2008	0.61	381	43	77.54
29	2009	0.62	382	44	79.34
30	2010	0.63	383	45	81.15
31	2011	0.65	385	47	84.75
32	2012	0.68	393	55	99.18
33	2013	0.7	398	60	108.20
34	2014	0.74	401	63	113.61
35	2015	0.78	402	64	115.41
36	2016	0.8	406	68	122.63
37	2017	0.81	410	72	129.84
38	2018	0.82	412	74	133.44
39	2019	0.83	413	75	135.25
40	2020	0.85	415	77	138.85

The usual concentrations that are represented in Table 2 as *mmp* values can be transformed into mg/m^3 by the application of the method given in [16]. So, the respective variation of *ppm* is:

$$\Delta C_{ppm} = \frac{24,4(l/mole) \cdot \Delta C[mg/m^3]}{M[g/mole]}$$

The variation of the concentrations of carbon dioxide $\Delta C[mg/m^3]$ in the atmosphere is:

$$\Delta C[mg/m^3] = \frac{M[g/mole] \cdot \Delta C_{ppm}}{24,4}$$

The respective dependence of the variation of the temperature *ΔT* as the function of *ΔC* is represented in Fig. 8. The respective slope of the graphic ΔT=f(ΔC) is:

$$\left(\frac{\gamma - 1}{\gamma(R-1)+1} \right) \cdot \frac{T}{C} = 0,006 ;$$

The atmospheric air has the concentration:

$$C = 0,04137(mol/l) = 41,37(mol/m^3)$$
$$\equiv 29(g/mol).41,37(mol/m^3) = 1199,73(g/m^3)$$

The value of adiabatic constant γ is calculated from the expression below:

$$\left(\frac{\gamma - 1}{\gamma(R-1)+1} \right) = \frac{0,006.C}{T} = \frac{0,006.1199,73}{288} = 0,02499 ;$$

$$\gamma = \frac{1+0,02499}{1-0,02499\cdot(8,31-1)} = \frac{1,02499}{1-0,1826} = \frac{1,02499}{0,8174} = 1,25$$

Thus, expression (16) could be written simply by proportional linear coefficient *a* as:

$$\Delta T_e = a.\Delta C + 0,0895 ; \quad \text{(e)-empirical}$$

$$a = \left(\frac{\gamma - 1}{\gamma(R-1)+1} \right) \cdot \frac{T}{C} = \frac{1,25-1}{1,25.7,31+1} \cdot \frac{288}{1199,73} =$$

$$\frac{0,25}{10,1375} \cdot \frac{288}{1199,73} = \frac{72}{12162,2628} = 0,006$$

$$\Delta T_e = 0,006 \cdot \Delta C + 0,0895 ; \quad [\Delta C] = mg/m^3 ;$$
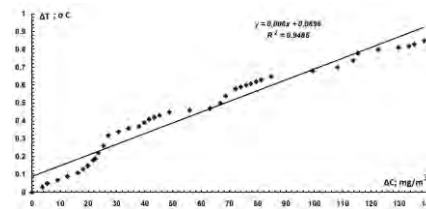
Fig. 8 The graphic of the dependence ΔT=f(ΔC)

The calculated values of ΔT_e can be checked with the real variations of ΔT by the representation in the following graphic (Fig. 9):
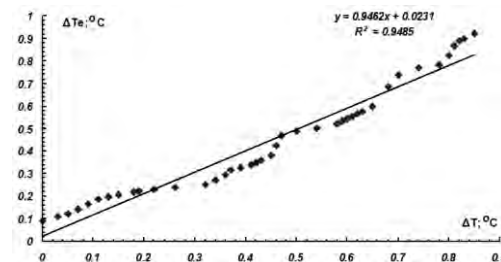
Fig. 9 The validity of empirical calculations of temperature variations

In order to include an important parameter such as the interval of time in the empirical expression, it is necessary to represent the following dependence of the variation of concentration of carbon dioxide as the function of time (Fig. 10). The rate of increase of CO_2 (speed of increasing the concentration each year) is about *3.383((mg/m^3)/year)*

Thus, the empirical formula of the temperature variation can be written as:

$$\begin{cases} \Delta T_e(t) = 0{,}006 \cdot \Delta C(t) + 0{,}0895 \\ \Delta C(t) = 3{,}3833 \cdot t - 8{,}6206; \\ [t] = years; \quad [\Delta C] = mg/m^3 \end{cases};$$

Fig. 10 The variation of the concentration of carbon dioxide as the function of time (starting year is 1980)

If every year the concentration of carbon dioxide has increased by *3.383 mg/m³,* then it would be possible to calculate the excess mass Δm_{CO2} per year.

$$\Delta m_{CO_2} = \Delta C \cdot V_{atm} = 3{,}383((mg/m^3)/year) \cdot 4{,}27596 \cdot 10^{18}(m^3) =$$
$$= 14{,}47 \cdot 10^{18}(mg/year) = 14{,}47 \cdot 10^{12}(kg/year) =$$
$$14{,}47 \cdot 10^9(tons/year) = 14{,}47(Gtons/year)$$

Study [15] gives this result about carbon dioxide: "Between 2009-18, however, the growth rate has been 2.3 ppm per year". When transposing *ppm* into mg/m³, then:

$$\Delta C[mg/m^3] = \frac{M[g/mole] \cdot \Delta C_{ppm}}{24{,}4} =$$
$$= \frac{44 \cdot 2{,}3}{24{,}4} = 4{,}14((mg/m^3)/year)$$

The result in this recent paper is 3.383 (mg/m³)/year. Then, the average value is 3.76 (mg/m³)/year. The respective admissible error is:

$$\varepsilon = \frac{|4{,}14 - 3{,}76|}{3{,}76} \cdot 100\% = \frac{38}{3{,}76} \approx 10\%$$

This ready performed suggested empirical expression is only momentary. It describes the actual global ecological state. The task is indeed the reduction of the rate of CO_2 emissions through the application of other types of energy resources.
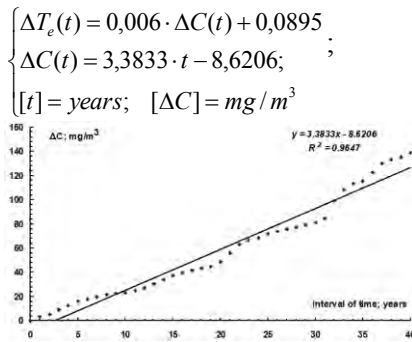
The important task of the world's population nowadays is to maintain at least the same level of carbon dioxide concentration in the atmosphere and just to decrease it, because the consequences in the future will be very unpleasant both for the biosphere, in general, and for human health, in particular. Therefore, in order to know the current state of the atmosphere with the recent concentration of carbon dioxide, it is necessary to know the variation of the concentration over time. This study suggests a model based on the thermodynamical theory of adiabatic processes in the atmosphere and the result is the achievement of an empirical expression of the temperature variation as a function of the concentration.

The validation of the empirical expression is finalized with the calculation of the excess mass of carbon dioxide, which is of the order of the real one as 15 billion tons per year.

REFERENCES

1. Haynes, H. M., ed. (2016–2017), CRC Handbook of Chemistry and Physics (97th ed.), CRC Press, p. 14, ISBN 978-1-4987-5428-6.
2. Jacobson, Mark Zachary (2005), Fundamentals of Atmospheric Modeling (2nd ed.) Cambridge University Press, ISBN 978-0-521-83970-9.
3. Ahrens, C. Donald (2006). Meteorology Today (8th ed.), Publishing. ISBN 978-0-495-01162-0.
4. Danielson, Levin and Abrams (2003). Meteorology. McGraw Hill.
5. Glossary of meteorology https://glossary.ametsoc.org/wiki/Adiabatic_1 pse_rate
6. Landau and Lifshitz (1980). Statistical Physics. Part 1. Pergamon.
7. Kittel and Kroemer (1980). Thermal Physics. Freeman. chapter 6, problem 11.
8. Lydolph, Paul E. (1985). The Climate of the Earth. Rowman and Littlefield Publishers Inc. p.12.
9. Landau and Lifshitz, Fluid Mechanics, Pergamon, 1979
10. Lide, David R. Handbook of Chemistry and Physics, Boca Raton, FL: CRC, 1996: 14–17
11. U.S. Standard Atmosphere (engineeringtoolbox.com), https://www.engineeringtoolbox.com/standard-atmosphere-d_604.html
12. Rebecca Lindsey and LuAnn Dahlman, "Climate Change: Global Temperature", March 15, 2021, Climate Change: Global Temperature | NOAA Climate.gov
13. World of Change: Global Temperatures (nasa.gov)
14. "Last four years have been the warmest on record – and CO_2 continues to rise", 7th January 2019, // Last four years have been the warmest on record – and CO_2 continues to rise | Copernicus
15. Rebecca Lindsey, "Climate Change: Atmospheric Carbon Dioxide", (2020), https://www.climate.gov/news-features/understanding-climate/climate-change-atmospheric-carbon-dioxide
16. Air pollution workbook, Introduction to Air Pollution - Workbook (utoledo.edu)

ASSESSMENT OF INDOOR AIR QUALITY IN SOME CLASSROOMS OF PROF. DR A. ZLATAROV UNIVERSITY, BURGAS

Vladilena Deyanova, Emilya Ivanova, Nikola Todorov

E-mail: steel_nick@yahoo.com

ABSTRACT

Assessing air quality in university classrooms is currently a subject of increasing attention, because it affects not only the comfort but also the health and performance of students and lecturers. In the current study, the air quality was assessed in classrooms 107 and 327, located on the first and third floors of the Inorganic Chemistry Building of Prof. Dr Assen Zlatarov University, Burgas. Measurement of particulate matter with aerodynamic diameter of 2.5 µm ($PM_{2,5}$) and 10µm (PM_{10}) was carried out using Trotec PC 220 fine particulate matter measuring device. The temperature and relative humidity of the air were also determined. The measurements were carried out weekly for a period of one month.

Particulate matter concentrations were measured for 15 min (during breaks when students are out of the classrooms) and for 45 min (during lectures in the presence of students). It was calculated that the average mass concentrations of $PM_{2,5}$ were in the range of 16.2 to 26.8µg/m^3, while these of PM_{10} were in the range of 35.2 to 63.6 µg/m^3. The assessment of the results indicated that the average mass concentrations of $PM_{2,5}$ and PM_{10} were lower than the allowable limits according to the national legislation of the Republic of Bulgaria. Comparing the measured values of the relative humidity and temperatures with the allowable limits, it was found out that they are within the comfort zone.

Keywords: monitoring, fine particulate matter, particle mass concentration

INTRODUCTION

The assessment of air quality in university classrooms is at present an issue to which increasing attention is being paid [Predescu Land D. Dunea 2021, Wongaree et al. 2020, Park and Song 2019], because it affects the whole educational process and students' concentration and productivity, and might as well affect the health of students and lecturers in the long run.

Studies have indicated that the exposition to particulate matter takes place mainly in closed premises. People spend about 80-90% of their time indoors, where the pollution is much higher than outdoors [Rivas et al. 2014]. The reason for this is the smaller degree of dilution, chemical transformation and dispersion, as well as the greater number of persons per unit volume.

There are quite few publications reporting studies of air quality in university classrooms. Concentrations of $PM_{2,5}$ and PM_{10} in the university classrooms of the Democritus University, Technical school, Xanthi, Greece were studied [Gaidajis and Angelakoglou, 2009]. It was found out that the average concentrations of $PM_{2,5}$ and PM_{10} in the rooms were in the ranges of 32–188 µg/m^3 and 25–151 µg/m^3, respectively.

Burdova et al. [2014] carried out measurements of $PM_{2,5}$, PM_{10} and PM_1 in the university classrooms of the Institute of Ecologic Engineering, Faculty of Construction in Kosice, Slovakia. The measurements were taken once per week for one month. It was found out that the values of PM_{10} concentration exceeded the allowable limits according to the Slovak legislation for 100% of the measurements. An investigation was carried out [Branis et al. 2005] involving a 12-hour analysis of the mass concentrations of $PM_{2,5}$, PM_{10} and PM_1 in a lecture hall of Harvard University in the presence and in the absence of students. The results revealed a correlation between the number of present students and PM levels. Similar results were obtained Aniefiok E. et al [Aniefiok E et al. 2017].

No data was found in the available literature about determination of air quality in the premises of Bulgarian universities.

With this background, the aims of the present work are as follows:

♦ measurement of the particle number concentrations of PM_{10} and $PM_{2.5}$ in rooms 107 and 327 of Prof. Dr Assen Zlatarov University;

♦ determination of the particle mass concentrations of PM_{10} and $PM_{2.5}$;

♦ assessment of the indoor air quality with respect to particulate matter and the physical parameters – temperature and relative humidity.

METHODS

2.1. Study area

Studies were carried out in the town of Burgas (population: over 210,000 inhabitants), Bulgaria. The town is located on Black Sea coast and is the most important cultural, economic, transport, governmental, tourist and educational center in South-East Bulgaria.

Among the biggest sources of hazardous emissions in the town are the nearby Lukoil Neftochim AD oil refinery, Kronospan EOOD, as well as the increasing automobile traffic after the construction of the Trakiya highway.

Prof. Dr Assen Zlatarov University is located in the north-western part of the town. Two of the buildings, the Organic Chemistry Building (OB) and the Inorganic Chemistry Building (IB) are situated at a distance less than 30 m from the E871 international road, which is the same as European road E773.

2.2. Apparatuses

Measurements were made using a particle counter (Trotec PC200), designed to measure the size and amount of particles in the air. To detect the data, the particle counter sucks in air with a flow rate of 2.83 l/min and determines the size and amount of particles contained in it using a laser diode (class 3R laser, 780nm, 1.5-3mW). The device automatically converts particle number concentration with aerodynamic diameter of 2.5 and 10 μm into particle mass concentration (μg/m³). The time of sampling, time interval between measurements and measurements count can be adjusted. Measured values are stored in the device memory and are easily transferred to a PC using a USB cable.

For the current study the time for sampling was set to 21sec (0.9912L of air), time interval – 39 sec and the count of measurements – 60.

During the measurements, the Trotec PC220 was placed at a distance of at least 2 m from doors or windows and at a height of 1 m from the floor.

2.3. Determination of monitoring sites

According to the aim of the study, two classrooms were selected for the present work, No. 107 and No. 327.

Some basic characteristics of these rooms were determined (Table 1).

Table 1. Basic characteristics of the classrooms

Characteristic	Room 107	Room 327
Area, m^2	60	40
Volume, m^3	186	124
Openable windows	3	2
Ventilation	Natural	Natural
Orientation	South-West	South-West
Number of occupants	11	11
Cleaning frequency	Thrice a day	Thrice a day

The selected rooms have different areas (40 and 60 m^3) and volumes (124 and 186 m^3). They have the same orientation, south-west, but room 107 is on the first floor, while room 327 is on the third. The height of the measurement is important for the distribution of the particles by size. The two rooms have natural ventilation. When the windows are open, particulate matter from the external environment such as road traffic, industry, domestic pollutants, etc. can get into the room. The number of occupants (students and lecturers) has a certain effect on the resuspension of the particles. The furniture and equipment in the rooms is very similar: desks, chairs, a white board and markers, a computer and a projector. The minimum distance between the students and the white board is 2 m and the maximum distance ensures good visibility from the farthest desks in the room. The internal pollution sources are fragrancies (deodorants, perfumes), smells (from sweating and breathing), particles of cleaning agents, disinfectants, air fresheners, secondary resuspension result from physical impact.

All the studies for the present work were carried out during the COVID-19 pandemic under strict compliance with the anti-epidemic measures and cleaning three times a day.

RESULTS AND DISCUSSION

Using Trotec PC220, the particle number concentrations (PNC) with aerodynamic diameter 2.5μm ($PM_{2,5}$) and 10μm (PM_{10}) were measured.

For monitoring the changes with time, the data obtained were plotted in a coordinate system. The change of PNC with time for $PM_{2,5}$ and PM_{10} are presented in Figs. 1 and 2.
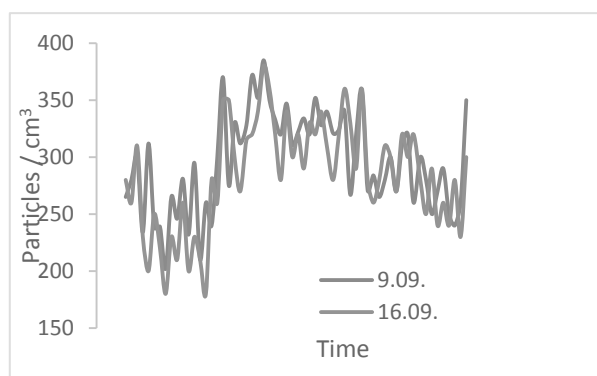

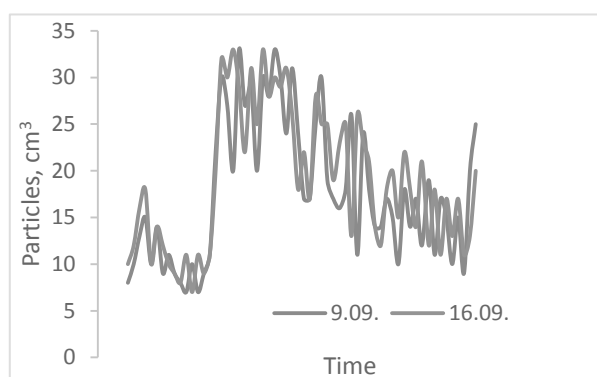**Fig. 1.** Course of particulate number concentration of $PM_{2,5}$

Fig. 2. Course of particulate number concentration of PM_{10}

Analyzing the change of PNC with time, the following important characteristics were observed. During the break, an air current is caused by the open door and windows and the concentrations of $PM_{2,5}$ and PM_{10} decreased, which indicates that the air outside was cleaner than that within the room. When students entered the room and the door and windows were closed, the concentration of particulate matter increased. This might be due to the introduction of internal pollutants, secondary resuspension from the physical impact. No big changes were observed during the academic hour, which can be explained with the stationary state of the students and the use of only markers and a computer during the lecture.

The general course shows a slight decrease of particulate matter concentration by the end of the lecture. For PM_{10}, this can be explained with the deposition of the particles on the surfaces while for $PM_{2,5}$ with inhaling them by the students and the lecturer.

The data about the particle mass concentrations were processed statistically to find the average concentrations during the 15 min breaks and the standard deviations (SD) with open windows and doors in the absence of students (Table 2) and the average for 45 min lecture time concentrations with closed windows and doors and the SD in the presence of students (Table 3).

Table 2. Average 15 min concentrations of PM_{10} and $PM_{2,5}$ in rooms 107 and 327 in absence

	Date	$PM_{10,}$ μg/m³		$PM_{2,5}$, μg/m³	
		Average 15min conc.	CO	Average 15min conc.	CO
107	09.09	36.2	2.6	17.2	3.0
	16.09	36.0	2.7	16.2	2.5
	23.09	35.3	2.9	20.8	2.9
	30.09	37.3	3.1	21.4	3.1
327	09.09	35.8	3.1	18.8	2.1
	16.09	36.3	2.6	19.3	2.3
	23.09	35.2	3.1	20.1	2.9
	30.09	36.6	4.2	20.1	2.8

of students

Table 3. Average 45 min concentrations of PM_{10} and $PM_{2,5}$ in rooms 107 and 327 in presence of students

Room	Date	$PM_{10,}$ μg/m³		$PM_{2,5}$, μg/m³	
		Average 45min conc.	CO	Average 45min conc.	CO
107	09.09	44.3	4.3	24.5	2.5
	16.09	46.6	4.5	25.4	3.0
	23.09	48.3	4.8	25.2	3.1
	30.09	42.7	3.9	23.9	2.8
327	09.09	49.8	4.4	25.4	3.5
	16.09	63.6	6.1	26.1	4.1
	23.09	46.6	4.5	26.8	3.3
	30.09	45.3	3.2	25.2	2.9

The results obtained for the average mass concentration of PM_{10} and $PM_{2,5}$ in rooms 107 and 327 in the presence and absence of students are graphically plotted in Figs. 3 and 4, respectively.
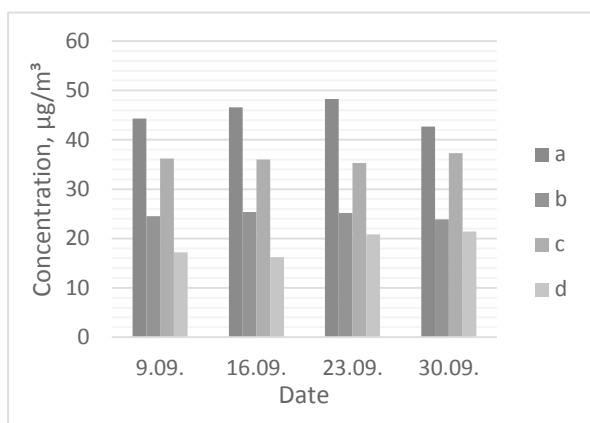
Fig.3. Average mass concentrations of PM_{10} and $PM_{2.5}$ in room 107 IE in presence and absence of students
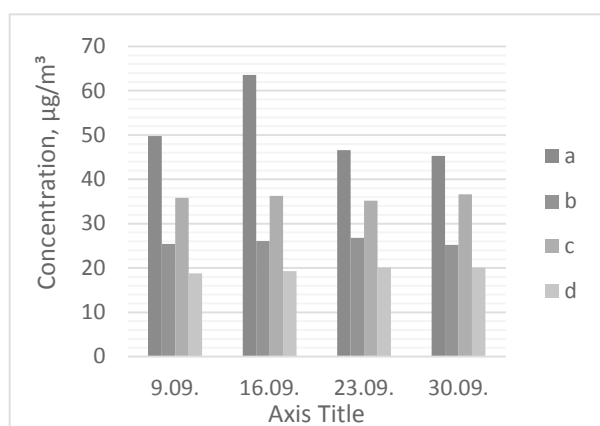

Fig.4. Average mass concentrations of PM_{10} and $PM_{2.5}$ in room 327 IE in presence and absence of students

The results (Tables 2 and 3 and Figs. 3 and 4) showed that the average mass concentrations of PM_{10} in the presence of students during lectures ranged from 42.7 to 63.6 μg/m³ while in the absence of students they were from 35.2 to 37.3 μg/m³. The values of $PM_{2.5}$ in the presence of students were in the range from 24.5 to 26.8 μg/m³ and in absence of students from 16,.2 to 21.4 μg/m³. The results for $PM_{2.5}$ obtained in room 107 were slightly lower than those in room 327, which can be explained by the difference in room volumes and the same number of students inside. However, this difference was not observed for PM_{10} which could result from the presence of a higher amount of PM_{10} on the first floor compared to that on the 3rd floor.

There are currently no standards for $PM_{2.5}$ and PM_{10} especially for the air within educational institutions. Usually, the general air quality standards are used as standards for the air quality in university rooms. To estimate the quality of the air in rooms 107 and 327, the results obtained were compared to the requirements existing in the European (Directive 2008/50/EU) and Bulgarian (Ordinance No.12/15.06.2010) legislation and to the directives of the World Health Organization (WHO) (Table 4).

Table 4. Standards and directives of WHO for $PM_{2.5}$ and PM_{10}

	Averaging time	Directive 2008/ 50/EU	Ordinance No.12/15.06 .2010	Directives of WHO
PM_{10}, (μg/m³)	1 year	40	40	20
	24 h	50	50	50
$PM_{2.5}$, (μg/m³)	1 year	20	25	10
	24 h	-	-	25

Comparing the results obtained from the present study to the standards shown in Table 4, it can be seen that the PM_{10} and $PM_{2.5}$ concentrations in rooms 107 and 327 are lower than the values required by the EU Directive and the national legislation (except for the value of PM_{10} on 16.09), although most of the average values were higher than the WHO recommended values.

Throughout the measurements of PM_{10} and $PM_{2.5}$, the Trotec PC220 device measured the temperature and the relative humidity of the air. From these data, the minimal, maximal and average values of the temperature and relative humidity were calculated (Table 5).

It can be seen that the temperature was in the range from 19.8 to 27.1°C and the relative humidity from 42.2 to 53.9%. These values were compared to the allowable limits defined with Ordinance No. RD-07-3 from 18.07.2014 and Ordinance No. RD-02-20-3 from December 21, 2015, which are in force at present in the Republic of Bulgaria. The Ordinances define the optimal allowable levels of the temperature during the warm period of the year, which is 24.5 ± 2.5, while the allowable levels of the relative humidity of the air are from 30 to 60 % at air temperature in the room 26°C < t ≤ 28°C; from 30 to 65 % at air temperature in the room 25°C < t ≤ 26°C; from 30 to 70 % at temperature 24°C < t ≤ 25°C and from 30 to 75 % at air temperature in the room t ≤ 24°C. The comparison of the values measured with the allowable levels showed that the relative humidity and the temperature in classrooms 107 and 327 are within the comfort zone.

Table 5. Minimal, maximal and average values of the temperature and the relative humidity measured in rooms 107 and 327 for the four days of the study

Room 107						
Date	Temperature, °C			Relative humidity, %		
	Min	Max	Mean	Min	Max	Mean
09.09	24.7	26.9	25.8	42.2	47.1	44.6
16.09	24.4	26.1	25.2	44.5	48.1	46.3
23.09	20.1	23.8	21.9	47.5	52.2	49.8
30.09	19.8	22.2	21.0	48.7	53.9	51.3
Room 327						
Date	Temperature, °C			Relative humidity, %		
	Min	Max	Mean	Min	Max	Mean
09.09	25.8	27.1	26.4	41.7	46.5	44.1
16.09	24.6	26.6	25.6	43.8	47.3	45.6
23.09	20.3	24.5	22.4	46.0	50.9	48.4
30.09	20.1	24.0	22.0	46.2	51.2	48.7

CONCLUSION

The air quality in rooms 107 and 237 in IB was assessed under the COVID-19 pandemic with strict compliance with the anti-pandemic rules. The rooms are on different floors and have different areas and volume. The $PM_{2.5}$ and PM_{10} concentrations were measured in the presence of students (during lectures) and in the absence of students (during breaks). The analysis of the data obtained showed a slight decrease of the concentrations by the end of the academic hour. For the PM_{10}, this could result from the deposition of the particles onto the surfaces in the room while for $PM_{2.5}$ from inhaling them by the students and the lecturer.

The particle mass concentrations were determined and for all the days studied. It was found out that the average mass concentrations of $PM_{2.5}$ were slightly lower in room 107 compared to room 327, which can be explained with the different volumes of the two rooms and the same number of students.

The results obtained from the present work will be used to improve the ecological knowledge and ecological education of the students to create habits of reducing pollution sources and a sense of responsibility for the maintenance of favourable air quality in the classrooms.

REFERENCES

1. Aniefiok E. et al. 2017, Particulate Matter and Staff Exposure in an Air-Conditioned Office in Akwa Ibom State University – Nigeria. *Journal of Atmospheric Pollution*. 5(1):24-32. doi: 10.12691/jap-5-1-4.)

2. Branis M., P. Rezacova and M. Domasova (2005). The effect of outdoor air and indoor human activity on mass concentrations of PM_{10}, $PM_{2.5}$, and PM_1 in a classroom, *Environ. Res. 99: 143-149*

3. Burdova E. et al., 2016, Investigation of Particulate Matters of the University Classroom in Slovakia, *Energy Procedia 96:620-627.*

4. Gaidajis G., K. Angelakoglou, Indoor air quality in university classrooms and relative environment in terms of mass concentrations of particulate matter, *Journal of Environmental Science and Health Part A–Toxic/Hazardous Substances & Environmental Engineering*, 44 (2009), 1227-1232.

5. Park S. W. and D. S. Song, 2019, The effect of student activity and outdoor conditions on particulate matter concentration in university classroom, *IOP Conf. Ser.: Mater. Sci. Eng. 609 042064.*

6. Predescu L. and D. Dunea, Performance Evaluation of Particulate Matter and Indoor Microclimate Monitors in University Classrooms under COVID-19 Restrictions, *Int J Environ Res Public Health 2021 Jul*; 18(14): 7363.Published online 2021 Jul 9. doi: 10.3390/ijerph18147363

7. Rivas I. et al. ,2014, Querol.Corrigendum to 'Child exposure to indoor and outdoor air pollutants in schools in Barcelona, *Spain Environment International* 69C, 200–212.

8. Wongaree M. et al. 2020, Indoor Air Quality of PM2.5 in Classrooms of Science Building, Udon Thani Rajabhat University, Thailand, *Thai Environmental Engineering Journal* 34 (3): 23-32.

CALCULATION OF CERTAIN PARAMETERS OF INSTALATION FOR ADSORPTION PURIFICATION OF VENTILATION AIR FROM VOLATILE ORGANIC COMPOUNDS

Elena Mollova, Anelia Darakova, Blagovesta Midyurova, Aleksandar Dimitrov, Dimitar Gogov
E-mail: al_dim_2000@abv.bg

ABSTRACT

In the production of commodities, the release of toxic substances (volatile organic solvents) into the atmosphere is constantly increasing. From an economic point of view, one of the most effective ways to deal with this is recovery, which involves capturing the vapors of organic solvents from industrial ventilation discharges and returning them to the main production for reuse. Depending on the concentration and physicochemical properties of the solvent, the volume of purified ventilation air and its condition (dust, humidity, temperature, etc.), different methods of recovery are used: condensation, absorption, adsorption and combined. In the present article, some calculations related to the adsorption of a volatile organic solvent in a fixed bed of the solid phase are done.

Key words: *adsorption, purification, ventilation air, volatile organic compounds*

INTRODUCTION

It is known that the adsorption process can take place on the surface of any solid. Solids with a large specific surface area are considered to be active adsorbents. These include porous substances, which may have different chemical nature and different origins. If not subjected to activation, the porous structure of natural mineral adsorbents depends on their composition and structure formed under natural conditions. The nature of the porosity of the adsorbents is of great importance both for the penetration in the pores of the adsorbent molecules and for the kinetics of the adsorption process [1-6].

Depending on the concentration and physicochemical properties of the solvent, the volume of purified ventilation air and its condition (dust, humidity, temperature, etc.), different methods of recovery are used (condensation, adsorption, absorption and combined) [7,8].

Adsorption methods and systems with continuous and intermittent action are mainly used for the purification of air with low vapor content of volatile solvents. For recuperative purposes, carbon adsorbents are primarily proposed [9-11].

There are no complete data and methodology in the literature for calculation of adsorption plants for recovery of volatile solvents, and there are no data on the adsorption and recovery of ethyl alcohol from air gas streams.

In this regard, it is necessary to make: the choice of adsorbent and the method of conducting adsorption and determine the hydraulic resistence of the layer and the apparatus, the dimensions of the adsorber, and the height of the adsorbent.

EXPERIMENT, RESULTS AND DISCUSSION

Calculations related to the adsorption of organic solvent in the fixed bed of the solid phase were performed in accordance with the set initial data: consumption of vapor-air mixture (8000 m^3/h); initial concentration of ethyl alcohol in the air (y_n = 2 g/m^3); concentration of ethanol in the purified air (y_k = 0.4 g/m^3); operating temperature (25°C) and pressure (735 mmHg).

Activated carbon of a certain brand with the following characteristics was chosen as an adsorbent (Table 1).

The adsorbent is selected in accordance with its porous structure, properties and the purpose of recovery. It has a low retention capacity, ie. It is easily regenerated.

Due to the low consumption of steam-air mixture, we assume that the adsorption devices have a periodic action. In this regard, it is necessary to set one of the two interrelated values – the height of the layer (L_{laver}) or the duration of the phases in the adsorption process.

Table 1. Adsorbent characteristics

Adsorbent	Bulk density (ρ_H) kg/m³	Fractional composition (fraction)		Area of application	Toughness kg/cm²	Structural constant B.10⁶, g.rad²
		mm	%			
activated carbon (AB-G)	580	5.0	1.0	To capture solvent vapor	70	74
		5.0 ÷ 2.8	83.0			
		2.8 ÷ 1.0	15.0			
		1.0 ÷ 0.0	1.0			

For a complex and efficient annular adsorber, the thickness of the adsorbent layer is determined by the dimensions of the concentric gratings between which the adsorbent is poured. We assume dimensions of the concentric lattices D_{out} = 1.2 m, D_{in} = 0.6 m, H = 2.5 m, L_{layer} = 0.3 m.

This height significantly exceeds the height of the working layer, ie. the mass transfer zone [12-15]. This excludes the possibility of leakage of the adsorbent. The height of the layer is determined only by the hydraulic resistance of the layer and the duration of adsorption.

Adsorption isotherm

Since the characteristic adsorption curves do not depend on temperature, but are sensitive to the chemical nature of the absorbed substance, we can construct the absorption isotherms of different substances, since we know the affinity coefficient β [11].

Using the equilibrium values x_1 and y_1 for adsorption of benzene (standard) on activated carbon AB-G, the corresponding values x_1' and y_1' for ethyl alcohol can be calculated according to the following dependences:

$$x_1' = x_1 \frac{1}{\beta} \qquad lg\, y_1' = \lg y_{H_2} - \beta \frac{T_1}{T_2} . \lg \frac{y_{H_1}}{y_1},$$

where: y_{H1} and y_{H2} are the concentration of the adsorbed substance in the gas phase, kg/m³; T_1 and T_2 – temperature, K.

At 25°C, the saturated vapor pressure of benzene is P_{H1} = 75 mmHg, and for ethyl alcohol P_{H2} = 44 mmHg.

From the gas state equation y = P/(R.T) we determine the volume concentrations:
$$y_{H_1} = 0.0041 \text{kg/m}^3; \quad y_{H_2} = 0.0024 \text{ kg/m}^3;$$
$$x_1' = x_1 \frac{1}{\beta},$$

where: x_1 and x_1' - concentrations of benzene and ethanol in the solid phase, kg/m³; β = 0.61 – affinity ratio (for ethyl alcohol).

The results of the calculations for the equilibrium values for the system: vapor (ethyl alcohol) – activated carbon are presented in Table 2.

From the calculated values the isotherm of adsorption of ethyl alcohol on AB-G is constructed (Fig. 1).
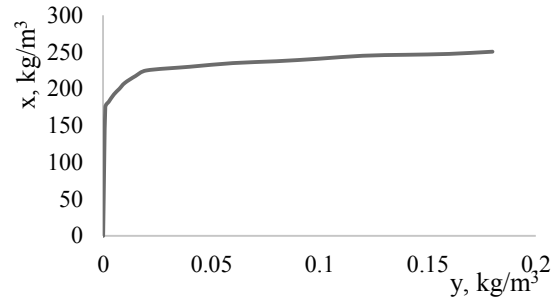
Fig. 1. Ethanol adsorption isotherm at 25°C

Conditionally, the adsorption isotherm can be divided into three regions for each of which the equations for determining the duration of adsorption are different [12-15].

The equilibrium initial concentration of ethyl alcohol in the solid phase (X_H = 182 kg/m³) is reported from the isotherm (Fig. 1).

From the adsorption isotherm it is determined in which area the value Y_H is (initial concentration of ethyl alcohol in a gas mixture Y_H = 0.002 kg/m³).

In our case Y_H is in the first region of the isotherm and the adsorption duration is calculated according to the following equation:

$$\sqrt{\tau} = \sqrt{\frac{G}{\omega}} . \sqrt{L_{layer}} - b . \sqrt{\frac{G}{\beta}}$$

where: τ – duration of adsorption, hour; G – Henry's coefficient, a dimensionless quantity; L_{layer} - height of the adsorbent layer, m; ω - average fictitious velocity of the vapor-air mixture, m/s; β - affinity coefficient; b - coefficient.

Determination of the duration of adsorption and desorption
➤ *Mass transfer coefficient*
$$\beta = 1.6 \frac{\omega_{CP}^{0,54}}{v^{0,54} . d^{1,46}} \text{ m}^2/\text{s},$$

where v – kinematic viscosity of the gas flow, m²/s; μ – viscosity, Pa.s; d – adsorbent particle diameter, m; D – diffusion coefficient, m²/s; P – density of the vapor-air mixture, kg/m³.

30

Table 2. Content of components – benzene and ethanol in the gas and solid phase.

x_1' benzene, кg/m³ solid phase	109.0	134.2	139.8	143.0	147.3	151.2
y_1' benzene, kg/m³ gas phase	0.00854	0.02560	0.05125	0.09390	0.17060	0.25610
x_1' benzene, кg/m³ solid phase	178.0	220.0	229.0	234.5	241.47	247.9
y_1' benzene, kg/m³ gas phase	0.0053	0.0156	0.0318	0.0595	0.1116	0.1731

According to the conditions in the adsorber (temperature 25°C and pressure 735 mmHg) for the vapor-air mixture we determine ρ = 1.21 kg/m³ and μ = 0.018.10⁻³ Pa.s, then we calculate the kinematic viscosity ν = 0.16.10⁻⁴ m²/s.

The diffusion coefficient for ethyl alcohol at 25°C is D = 0.135.10⁻⁴ m/s.

The gas flow rate is a variable. Therefore, in the equations, the arithmetic mean value of the gas flow rate at the inlet, in the adsorbent layer and at its outlet must be determined.

In this regard, it is necessary to calculate the area of the grid s_{CP} = 7.07 m²:

$$s_{CP} = \frac{\pi . H_P}{2} . (D_1 + D_2),$$

where: H_P – lattice height, = 2.5 m; D_1 – outer diameter of the grid, = 1.2 m; D_2 – inner diameter of the grid, = 0.6 m.

The average fictitious velocity of the vapor-air mixture is 0.32 m/s.

$$\omega_{CP} = \frac{V}{60.s_{CP}},$$

where V – consumption of steam-air mixture, m³/h.

It follows that the mass transfer coefficient at 25°C is β = 17.42 s⁻¹.

From the benzene adsorption isotherm, the points are calculated and the ethyl alcohol adsorption isotherm is constructed. This allows us to read the concentration of ethyl alcohol in the activated carbon at the set initial concentration and pressure determined by it.

➤ *Determination of the adsorbate concentration in the solid phase.*

$$P_0 = Y_H . R . T$$

At Y_H = 0.002 kg/m³, we determine P_0 = 0.8 mmHg. From the adsorption isotherm at P_0 = 0.8 mmHg we read the initial concentration in the adsorbent X_H = 55 kg/m³ (Fig. 2).

➤ *Calculation of adsorption time*

To determine the duration of adsorption, it is necessary to calculate the height (length) of the adsorbent layer and the constant b, which is proportional to the reciprocal of the Crump function (Φ^{-1}) and the ratio between the content of the target component in the gas stream and its initial content in the vapor-air mixture.
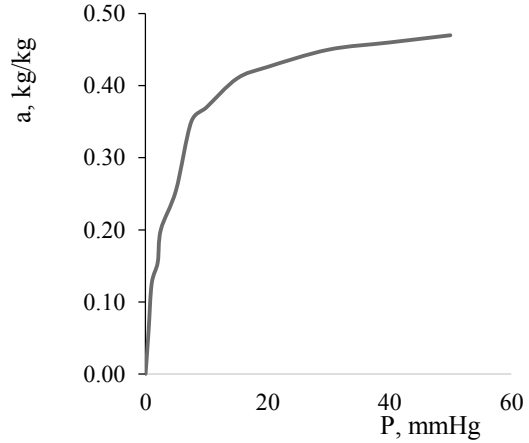

Fig. 2. Isotherm of adsorption of ethyl alcohol on activated carbon at 25°C

$$\sqrt{\tau} = \sqrt{\frac{G}{\omega_{CP}}} . \sqrt{L_{CN}} - b . \sqrt{\frac{G}{\beta}}; \qquad G = \frac{X_H}{Y_H};$$

$$L_{CN} = \frac{D_1 - D_2}{2}; \quad b = \Phi^{-1}\left(1 - \frac{Y_K}{0,54 . Y_H}\right)$$

Crump's function is defined by the expression:

$$\Phi_{(Z)} = \frac{2}{\sqrt{\pi}} \int_0^Z e^{-z^2} . dZ$$

Depending on the values of Z, the Crump function, resp. and the constant b can be determined tabularly from the ratio:

$$\frac{Y_K}{Y_H} = \frac{0.0004}{0.002} = 0.2$$

For $\frac{Y_K}{Y_H}$ we report a value for b = 0.63 $\sqrt{\tau}$ = 5 h

➤ *Determination of the fictitious length of the adsorbent layer, according to the profile of the change in concentration*

The concentration of ethanol in the initial mixture is:

$$C_H = \frac{Y_H . P . M}{R.T} = 0.079 \text{ kg/m}^3,$$

where Y_H – the ethyl alcohol content of the starting mixture, mol; M – molecular weight of ethanol.

From the adsorption isotherm we find the concentration of ethanol in the sorbent, which is in equilibrium with the initial composition of the gas:

$$X^*_{(CH)} = \frac{0.375\,C_H}{1+8.C_H} = \frac{0.375 \cdot 0.079}{1+8 \cdot 0.079}$$
$$= 0.018 \frac{kg\ alcohol}{kg\ activated\ carbon}$$

The content of ethyl alcohol in the fictitious length of the adsorbent layer is:

$$z = \frac{\omega \cdot \tau \cdot C_n}{\varepsilon \cdot C_H + \rho_{HAC} \cdot x^K_{HC}} = 45\ m$$

The fictitious length of the adsorbent layer at an adsorption time of 5 hours and a velocity of the vapor-air mixture of 0.32 m/s is equal to 45 m.

Determination of the minimum time for practically complete desorption of ethyl alcohol from a layer with a length of 45 meters, which initially contains 0.018 kg of alcohol/kg of activated carbon. At z = H = 45 m the desorption will end after time:

$$\tau_{gec} = \frac{H\left|\varepsilon + \rho_{HAC}\left(\frac{dX^*}{dC}\right)_{C=0}\right|}{\omega} = 8\ h$$

We assume that at the initial moment the concentration of ethyl alcohol is equal to zero. Then $\left(\frac{dX^*}{dC}\right)_{C=0} = 0.375$.

Not more than 8 hours are required for complete desorption of the bed, at a gas velocity of 0.32 m/s.

Determination of the minimum gas velocity at which practically complete desorption of the bed can be achieved in 3 hours.

$$\omega_g = \frac{H\left|\varepsilon + \rho_{HAC}\left(\frac{dX^*}{dC}\right)_{C=0}\right|}{\tau_{gec}} = 0.86\ m/s$$

CONCLUSIONS

An annular adsorber and a hydrophobic adsorbent - activated carbon of recuperative type (AB-G) were selected, and the isotherm of adsorption on ethyl alcohol was calculated by the method of affinity characteristic curves.

The adsorption and desorption times, the height (length) of the adsorbent layer were calculated according to the set initial (2 g) and final (0.4 g) concentrations of ethyl alcohol in the gas mixture.

REFERENCES

1. Astrakova, T. *Catalysis in industry*, 2012, 1, pp. 64-68. (in Russian)
2. Dubinin, M. Porous structure and adsorption properties of activated carbon, Moscow, 1965. (in Russian)
3. Lashkov, V. and S. Kondrasheva. *Bulletin of the Kazan Technological University*, 2010, 10, p. 360. (in Russian)
4. Gogov, D. and L. Ljubtchev. *Colloids and Surfaces*, 1992, 66(3), p. 223.
5. Gregg, S. and W. Sing. Adsorption, Surface Area and Porosity. Academic Press, London, 1982.
6. Rouquerol, J., F. Rouquerol, P. Llewellyn, G. Maurin and K. Sing. Adsorption by Powders and Porous Solids: Principles, Methodology and Applications. 2nd ed. Elsevier Ltd, 2014.
7. Lukin, V. and I. Antsypovich, Recuperation of volatile solvents in the chemical industry, Leningrad, Chemistry, 1981.
8. Robinson, C. The recovery of volatile sovents in chemical engineering, Merchant Books, 2006.
9. Kinle, X. and Z. Bader. Activated carbons and their industrial application, Leningrad, Chemistry, 1984. (in Russian)
10. Marsh, H. and F.R. Reinoso. Activated Carbon, Elsevier, 2006.
11. Komarov, V. and A. Ratko. Adsorbents: production, structure, properties. Science, Minsk, Belarus, 2009. (in Russian)
12. Keltsev N. Fundamentals of adsorption tecniques. 2 edit., Chemistry, Moscow, 1984. (in Russian)
13. Bandosz, T. (Editor). Activated Carbon Surfaces in Environmental Remediation, 7, Sciencedirect, 2006.
14. Ghaedi M. (Editor). Adsorption: Fundamental Processes and Applications, 33, Sciencedirect, 2021.
15. Douglas LeVan M. (Editor). Fundamentals of adsorption. Proceedings of the fifth international conference on fundamentals of adsorption. Springer, 1996

EVALUATION OF GASOIL PURIFICATION BY THERMODYNAMIC AND KINETIC PARAMETERS

Milena Dimitrova, Yordanka Tasheva
E-mail: jtasheva_2006@abv.bg

ABSTRACT

The adsorption processes of gasoil purification from sulphur compounds were investigated by thermodynamic and kinetic parameters. The adsorption of the used raw materials took place at ambient conditions and different adsorbents. The thermodynamic and kinetic parameters were calculated using well-known equations. It was concluded that adsorbent alumina is a better adsorbent for purification of the investigated gas oils.

Key words: sulphur compounds, adsorption, energy of Gibbs, reaction constant

INTRODUCTION

Adsorptive desulphurization at ambient conditions can supplement the hydrodesulphurization process and offers an alternative solution to the high cost of producing ultra clean fuels. The process employs a solid adsorbent material to selectively adsorb sulphur compounds from targeted streams. The process can be divided into two types: reactive and non-reactive. In the reactive adsorption process, a sulphur atom from the compound is stripped off and the remaining hydrocarbon is recovered. This type of adsorption usually occurs at high temperature. In non-reactive adsorption, the sulphur compounds are mostly physically adsorbed on the surface. In this case, the operating conditions are mild (<100°C) and the material adsorbs the organosulphur compounds as a whole. The adsorption process can also be employed with or without the use of auxiliary gases such as hydrogen. Regeneration of the adsorbent is necessary when a continuous process is called for.

In recent years, desulphurization by direct adsorption of organosulphur species (non-reactive adsorption) at ambient conditions has gained much attention [1, 2-4].

Selective adsorption of sulphur species is one of the most promising solutions for producing ultra clean hydrocarbon fuels. The process primarily requires an adsorber with or without the need of supplementary streams (e.g. hydrogen) or other external auxiliary units (e.g. separators, compressors for hydrogen). Energy efficient and environmentally benign, the process does not require operations at extreme temperatures or pressures. Some adsorption processes can even be operated at room temperature and atmospheric pressure. Based on the adsorbent materials, adsorptive desulphurization addresses a major problem generally faced by the HDS process: the selectivity toward polyaromatic sulphur heterocycles (PASH). Heavy thiophenic derivatives, such as methylated benzthiophenes and dibensthiophenes, have very low reactivity with hydrogen in the presence of HDS catalysts as compared to their aliphatic counterparts, thus resisting the HDS process and remaining in the product streams. Selective adsorption provides novel mechanisms of capturing sulphur from hydrocarbon streams, such as π-complexation and the use of surface acidity. As a result, some of the adsorbent materials demonstrate a great selectivity toward PASH molecules. This is also complemented by the absence of any extraneous reactions, such as olefin hydrogenation or octane/cetane number reduction. Adsorptive desulphurization possesses a great applicability toward fuel cell applications due to its ability to deeply desulphurise hydrocarbon fuels. With the variation of the adsorbent bed volume, the targeted sulphur concentration can be varied from a few ppmw to ppbw ranges. Adsorption has a significant edge over other processes in the case of application in portable desulphurization systems. As seen from the discussion above, there are marked differences between the sulphur removal operation in the refineries and portable desulphurization paradigm. The onboard units

should be compact, simple in design and should require fewer or no supplementary streams. The conventional HDS process requires high temperatures and pressure along with auxiliary units, hence it is not suitable for on-board systems. The absence of major auxiliary units is a major advantage for adsorptive desulphurization. For this reason, the adsorption process can be scalable to any sizes and can be used in various applications. The low temperature adsorbent in the fuel processing units allows for the "cold-starts" of hydrogen vehicles. Operation at atmospheric or mild pressures reduces the process safety challenges to a great extent. The absence of hydrogen requirements would greatly alleviate the complexity of the process. For all the features mentioned above, adsorptive desulphurization would be better suited for mobile fuel cell stacks than other commercial or prospective sulphur abatement processes. It would be an ideal process that could supplement the HDS process as a polishing step. In spite of the many advantages, adsorptive desulphurization is not free from limitations. The process is primarily limited by the adsorbent capacity. Most of the adsorbent materials have very low capacities for sulphur adsorption as compared to the catalytic HDS process. The lower capacity may be attributed to the facts that adsorption takes place instead of catalytic reaction and also there are mass transfer and diffusion limitations. Liquid phase adsorption proceeds much slower than gas phase; as a result, the production rate would be low. It also depends upon the adsorption equilibrium, thereby performing poorly for low sulphur feed. Due to its low capacity, the adsorber volume has to be significantly large considering the target production. Therefore, the economies involved regarding the cost of the adsorbent materials should be considered. Regeneration of the adsorbent bed should also be necessary if the objective is continuous operation. In the case of regeneration by flowing gaseous streams, pressure drop becomes an issue. The choice of medium for regeneration would also be important, and easily available gases (air, steam, exhaust gases) should be appropriate for application in the regeneration process [5-7].

In this study, the evaluation of adsorption laboratory processes by thermodynamic parameters was investigated.

EXPERIMENT

All technological experiments were conducted under laboratory conditions. Silica gel and alumina were used as adsorbents. The middle distillate fractions were purified. The physicochemical properties of raw materials and adsorbents are given in Ref. 8.

The investigated adsorption processes were provided at follow conditions: temperature from 293.15 to 323.15 K, contact time from 1.5 h to 6.0 hours and ratio raw material: adsorbent = 1:20.

The evaluation of adsorption processes was done by calculating thermodynamic parameters: free energy of Gibbs, enthalpy and entropy as well as by calculating kinetic parameters such as activation energy, reaction constant and Arrhenius constant of each raw material: adsorbent system. The thermodynamic and kinetic parameters were calculated using well-known physicochemical equations, which are presented in Ref. 9, 10.

The obtained experimental results are presented in the next section.

RESULTS AND DISCUSSION

The following tables show the calculated thermodynamic parameters of each raw material: selected adsorbent system:

Table 1. Results of thermodynamic parameters of adsorption processes OG1: silica gel

T, K	τ, h	ΔH, kJ/mol	ΔS, kJ/mol.K	ΔG, kJ/mol
293.15	1.0	-860	-1.47	-430
293.15	1.5	-2015	-3.44	-1008
293.15	2.0	-4346	-7.41	-2173
293.15	3.0	-6660	-11.36	-3330
293.15	4.5	-7996	-13.64	-3998
293.15	6.0	-9064	-15.46	-4532
303.15	1.0	-1473	-2.43	-736
303.15	1.5	-2431	-4.01	-1215
303.15	2.0	-4967	-8.19	-2483
303.15	3.0	-6434	-10.61	-3217
303.15	4.5	-8651	-14.27	-4325
303.15	6.0	-10744	-17.72	-5372
313.15	1.0	-2135	-3.41	-1068
313.15	1.5	-4705	-7.51	-2353
313.15	2.0	-5941	-9.49	-2971
313.15	3.0	-8478	-13.54	-4239
313.15	4.5	-9107	-14.54	-4554
313.15	6.0	-10312	-16.46	-5156
323.15	1.0	-3427	-5.30	-1714
323.15	1.5	-6131	-9.49	-3065

323.15	2.0	-6911	-10.69	-3456
323.15	3.0	-8981	-13.90	-4491
323.15	4.5	-10432	-16.14	-5216
323.15	6.0	-11453	-17.72	-5727

Table 2. Results of thermodynamic parameters of adsorption processes OG1:alumina

T, K	τ, h	ΔH, kJ/mol	ΔS, kJ/mol	ΔG, kJ/mol
293.15	1.0	-2436	12.53	-6107.40
293.15	1.5	-2436	10.08	-5391.05
293.15	2.0	-2436	7.01	-4490.04
293.15	3.0	-2436	5.57	-4070.07
293.15	4.5	-2436	4.87	-3864.08
293.15	6.0	-2436	3.86	-3569.15
303.15	1.0	-2519	8.72	-5261.04
303.15	1.5	-2519	7.09	-4668.14
303.15	2.0	-2519	4.87	-3996.04
303.15	3.0	-2519	3.98	-3726.38
303.15	4.5	-2519	1.93	-3104.09
303.15	6.0	-2519	1.48	-2968.98
313.15	1.0	-2602	6.90	-4762.45
313.15	1.5	-2602	5.18	-4225.24
313.15	2.0	-2602	3.28	-3628.28
313.15	3.0	-2602	2.33	-3333.70
313.15	4.5	-2602	0.83	-2862.21
313.15	6.0	-2602.54	-0.70	-2384.04
323.15	1.0	-2685.71	5.80	-4558.93
323.15	1.5	-2685.71	3.95	-3963.08
323.15	2.0	-2685.71	2.61	-3529.74
323.15	3.0	-2685.71	1.93	-3309.14
323.15	4.5	-2685.71	0.01	-2689.97
323.15	6.0	-2685.71	-1.18	-2305.44

Table 3. Kinetic parameters of adsorption process of OG1:silica gel

T, K	Reaction constant k, s^{-1}	Activation energy, kJ/mol	Arrhenius constant
293.15	223	0.9299	568682
303.15	353	0.8992	568682
313.15	459	0.8705	568682
323.15	449	0.8435	568682

Table 4. Kinetic parameters of adsorption process of OG1:alumina

T, K	Reaction constant k, s^{-1}	Activation energy, kJ/mol	Arrhenius constant
293.15	388	0.6804	104674
303.15	388	0.6580	104674
313.15	533	0.6370	104674
323.15	629	0.6173	104674

Table 5. Kinetic parameters of adsorption process of OG2:silica gel

T, K	Reaction constant k, s^{-1}	Activation energy, kJ/mol	Arrhenius constant
293.15	231	1.0604	1734174
303.15	385	1.0254	1734174
313.15	470	0.9927	1734174
323.15	534	0.9620	1734174

Table 6. Kinetic parameters of adsorption process of OG2:alumina

T, K	Reaction constant k, s^{-1}	Activation energy, kJ/mol	Arrhenius constant
293.15	423	0.6125	66578
303.15	446	0.5922	66578
313.15	573	0.5733	66578
323.15	659	0.5556	66578

As shown by the calculated data obtained at all temperatures, the duration of contact and the ratio of raw material: adsorbent purification process is thermodynamically possible. It should be noted that with increasing the temperature and contact time we got better results for Gibbs energy and entropy. The best results were obtained using adsorbent alumina and raw material OG1, average results were obtained with adsorbent alumina and silica gel in raw materials OG1 and OG2. The worst are the thermodynamic and kinetic characteristics of the OG1: silica gel systems.

The negative values obtained for the free energy of Gibbs confirm the experimental data on the process of adsorption of the raw materials studied by us, while at the same time they show that this process is thermodynamically possible for all the systems studied.

From the obtained data on the entropy of distribution of the individual systems, it can be seen that in the process of adsorption of the middle distillate fractions studied by us the most probable interaction of the type of specific solvation is performed, without noticeable thermal effect.

REFERENCES

1. Wang L., S. Baode, Fr. Yang et all. *Chemical Engineering Science,* **73**, (2012), p. 208.
2. Wang F., Zh. Zhang, J. Yang et all. *Fuel,* **107,** (2013), p. 394.
3. De Luna M., M. Samaniego, D. Ong et all. *Journal of Cleaner Production,* **178,** (2018), p. 468.

4. Fallah R., S. Azizian, G. Reggers et all. *Fuel Processing Technology,* **119,** (2014), p. 278.

5. Gao Sh., G. Yu, R. Abro et all. *Fuel*, **173** (2016).

6. Shahrani F., T. Xiao, M. Green et all. *Catalyst. Appl. Catal. B-Environ.*, **73** (2007).

7. Ma X., A. Zhou, Ch. Song. *Catal. Today*, 123 (2007).

8. Guttierez J., G. Fuentez, M. Hernandez-Teran et all.*Appl Catal A-Gen*., **305** (2006).

9. Tasheva Y. *Annual of Assen Zlatarov University*, **XLVIII** ((2019).

10. Tasheva Y., Al. Dimitrov, M. Dimitrova, *Annual of Assen Zlatarov University*, **XLVIX** (2020).

GARNET CERAMIC PIGMENTS DOPED WITH SEVERAL D-CHROMOPHORE ELEMENTS

Fila Yovkova, Irena Markovska
E-mail: fila_03@abv.bg

ABSTRACT

Garnet ceramic pigments were synthesized by solid state synthesis of pure oxides: CaO, $SiO_2.nH_2O$. The dyers added were V, Fe, Cr, which were introduced with the following oxides: NH_4VO_3, Fe_2O_3 and $K_2Gr_2O_7$. The pigments were synthesized at final sintering temperature of 1100°C. The color characteristics of the garnet ceramic pigments were determined using the CIELab color measuring system.
Key words: garnet pigments, solid-state sintering, CIELab color measurement

INTRODUCTION

In nature, garnets have been formed at high temperatures and pressures. They are artificially synthesized at temperatures up to 1200°C and in the presence of mineralizers. By substituting the two-valence ions with Ba^{2+} or Ni^{2+} uniquely colored garnets which are not found in nature are obtained.

One of the best-known natural garnets with beautiful green color is uvarovite $Ca_3Cr_2(SiO_4)_3$ or $3CaO.2Cr_2O_3.3SiO_2$. It is produced artificially and is known as "Victoria green". On the basis of the garnet grossular $Ca_3Al_2(SiO_4)_3$, series of garnet pigments were prepared by full or partial substitution of CaO with MgO, MnO and FeO, and Al_2O_3 with Cr_2O_3 and Fe_2O_3. Pigments doped with Co, Ni, Cu, Ba, Zn were synthesized by partial substitution of SiO_2 with ZrO_2, TiO_2 and SnO_2. In the search of new and stale pigments, the acidic radical $[SiO_4]^{4-}$ has been replaced also by $[PO_4]^{4-}$.

In nature, phosphorus containing garnets are quite rare, mainly as spessartine which contains manganese and has pink-red to yellow-brown color. It is possible to obtain pigments based on solid solutions of garnets and phosphates. Pigments were also obtained by mixing garnets and spinels – highly stable mixtures of various colors are formed while preserving the structure of the main crystals [1].

The aim of the present work is to synthesize garnet ceramic pigments from pure raw materials and study the possibilities for their application in the silicate industry.

EXPERIMENT

Methods

Color measurement. The color of pigments is determined by tintometer (Lovibont Tintometer RT 100 Colour) and presented in the CIELab color space as defined by the International Commission on Illumination (CIE).

X-ray analyses. Phase composition of the synthesized ceramic pigments was determined using X-ray diffraction (XRD) with a Bruker D8 diffractometer operating at 40 kV and 40 mA with CuKα radiation.

Materials

Garnet ceramic pigments were synthesized by the method of solid state sintering of pure oxides: CaO, $SiO_2.nH_2O$. The dyers added were V, Fe, Cr, introduced with the following oxides: NH_4VO_3, Fe_2O_3 and $K_2Cr_2O_7$.

The blends compositions are presented in Table 1.

Table 1. Initial materials

No of the sample	Composition	Synthesis temperature
1	**3CaO.Fe$_2$O$_3$ .3SiO$_2$** CaCO$_3$ Fe$_2$O$_3$ SiO$_2$	1100°C
3	**CaO.V$_2$O$_3$.3SiO$_2$** CaCO$_3$ NH$_4$VO$_3$ SiO$_2$	1100°C

9	**3CaO.Cr$_2$O$_3$.3SiO$_2$**		
	CaCO$_3$	1100°C	
	K$_2$Cr$_2$O$_7$		
	SiO$_2$		

Blends compositions

The blends were prepared by weighing the corresponding quantities of the initial components, mixing and homogenizing them. The grinding and homogenization were carried out simultaneous in a Pulverisette 6 planetary mill (Fritsch, Germany). The materials were ground for 1 h at 150 rpm, so that the particles of each material had sizes by the order of micrometers. The samples were placed in a furnace at room temperature and the final sintering temperature was 1100°C with isothermal period of 2 h.

Photographs of the initial blends and the pigments synthesized are shown in Fig. 1.

Fig. 1. Initial blends and sintered pigments – synthesized at 1100°C

RESULTS AND DISCUSSION

Color measurement

The main characteristic of the chromophores (components and structural specificities of the pigments which cause their dying properties) is their ability to intensely absorb and transform the light energy (electromagnetic radiation) in the visible part of the spectrum. It means that color is imparted by the selective absorption of light with certain wave lengths. [1]

The color space of CIELAB is defined by the Commission Internationale de l'Éclairage (CIE) and is used to describe all the colors visible to the human eye in a 3D model determined by L *, a * and b * values as Cartesian coordinates and C

* and h ° as polar coordinates in a three-axes system for color calculation [2, 3].

Pigments colors were determined with a Lovibond Tintometer RT 100 Colour using a spectral method. In the CIELab system the color coordinates were as follows:

- L* - brightness, L*= 0 – black color, L*= 100 – white color

- a* - green color (-) / red color (+)

- b* - blue color (-) / yellow color (+)
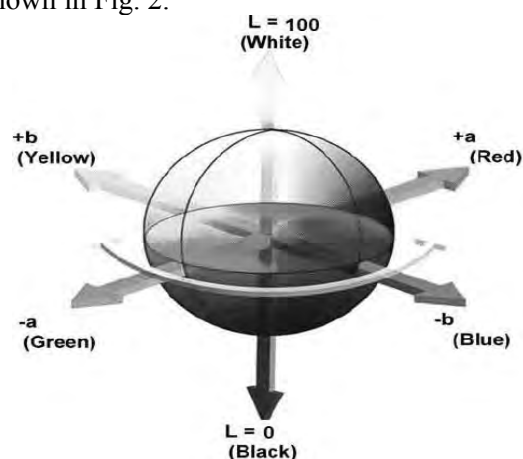
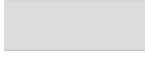The color space of the CIELab system is shown in Fig. 2.

Fig. 2. Colour space of CIELab system [4]

The results obtained from the measuring of the colors of the pigments synthesized are given in Table 2.

Table 2. Results obtained from the measurement of the color coordinates of garnet ceramic pigments in the CIELab system

Sample	Colour	L	a *	b *
1 / 1100°C		57.67	6.50	9.97
3 / 1100°C		89.42	-6.61	20.67
9 / 1100°C		64.51	-3.90	46.59

X-ray analyses

The main phases present in the pigments synthesized were determined by XRD. The results obtained from the analysis of the sample with composition 9 are shown in Fig.3.

38

Fig. 3. Diffractogram of sample 9 synthesized at 1100°C

It can be seen from the diffractogram in Fig. 3 that the predominant phases were as follows: uvarovite 82.7% ($Ca_3Cr_2(SiO_4)_3$) and pseudowollastonite ($Ca_3Si_3O_9$) 13.4%.

CONCLUSIONS

Garnet pigments were synthesized from pure oxides by the method of solid state sintering.

The color characteristics of the garnet pigments synthesized were determined using the CIELab color measuring system.

XRD analysis of the pigments synthesized was carried out. The main phases were identified. The predominant phase was found to be uvarovite 82.7% ($Ca_3Cr_2(SiO_4)_3$).

It was established that the garnet pigments synthesized can be used in glazes for faience tiles.

REFERENCES

1. Gerasimov, E., A. Gerasimov, A. Atanasov, V. Toshev, D. Petkov, D. Ivanov, L. Georgieva, L. Pavlova, N. Drenska, Vinarov P., Petrov P., Bachvarov S., Panova C., S. Bagarov, S. Serbezov, S. Stefanov, S. Dzhambazov, T. Stojkova, T. Datskova, H. Berlinov. *Technology of Ceramic Products and Materials, Ed. S. Bachvarov, Saraswati IC, Sofia, 2003.*
2. Lillotte, T. D., M. Joester, B. Frindt, A. Berghaus, R. F. Lammens, K. G.Wagner, UV–VIS spectra as potential process analytical technology (PAT) for measuring the density of compressed materials: Evaluation of the CIELAB color space, *Int. J. Pharm.*, **603** (2021), p. 120668.
3. Berns, R.S., *Numerical Color Specification: Colorimetry, in: Billmeyer and Saltzman's Principles of Color Technology. John Wiley & Sons, Ltd, Hoboken, NJ, (2019), p. 51–84.*
4. Singh, B., D.V. Parwate, S.K. Shukla, Radiosterilization of Fluoroquinolones and Cephalosporins: Assessment of Radiation Damage on Antibiotics by Changes in Optical Property and Colorimetric Parameters. *AAPS Pharm.Sci.Tech.*, **10,** (2009), p.34–43.
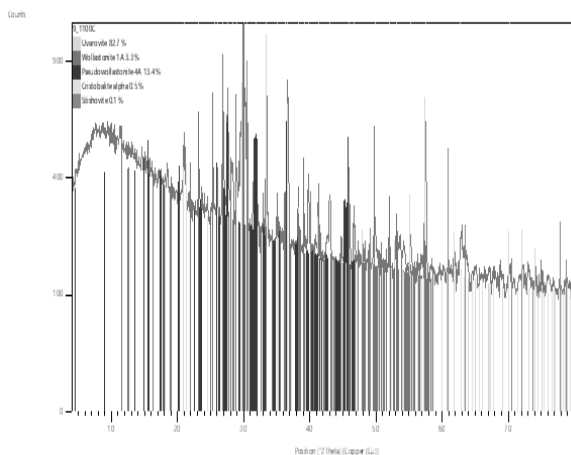
HEALTH BENEFITS OF EATING NATURAL HONEY. PHYSICOCHEMICAL ANALYSIS OF HONEY

Galina Grigorova
E-mail: galinakirova@abv.bg

ABSTRACT

The aim of this study was to review the role of the consumption of honey by the Bulgarian population and to define the health norms related to it. The general recommendations for consumption of honey can be traced back to ancient times. Our study includes physicochemical analysis of honey performed in the period from June to August. We analysed some basic physicochemical parameters (sucrose, hydroxymethylfurfural, diastase activity and water content), which give information about the quality of honey. We also conducted a survey on the consumption of honey by Bulgarians.

Key words: *honey, healthy eating, physicochemical analysis*

INTRODUCTION

Food is a major factor for human health. The microbiological and physicochemical safety of food is very important for our health. Scientific research in the food industry helps consumers make informed decisions toward a more balanced diet. In medicine, well-balanced eating is defined as the healthy and optimal eating which is adequate for the needs of the human body for energy and nutrients of specific quantity and quality, satisfying the plastic needs and growth, maintaining optimal body weight and high productivity, and boosting the body's natural resistance to diseases and unfavourable environmental conditions, maintaining the optimal level of all vital processes under various conditions of life and work, promoting good physical and mental health, as well as reproductive health and having healthy and fit offspring [3]. The introduction of minimally processed foods in the diet of the Bulgarian people is a good alternative, which also contributes to the ecological balance. Honey is one such type of food. 'Honey' is the common name of the sweet food substance produced by the honey bees Apis mellifera from plant nectar or from secretions of the living parts of plants [1]. Honey consists of more than 400 components. Since ancient times honey has been known as a product with exceptionally high energy density and biological activity. Honey is one of the first medicines known to man. In the past, people regarded honey as the only substance that could guarantee a long and healthy life. The advancements in sciences such as chemistry, biochemistry, and microbiology have helped define the composition of honey and most of the mechanisms of its pharmacological effects on the human body. Currently, the antibacterial activity of honey is subject to strenuous research and is already used successfully in medicine for the treatment of some wounds, and some gastrointestinal, hepatic and other disorders. Specific antimicrobial ingredients have been found in some types of honey, including our honeydew honey (oak forest honey) [2]. Scientific research shows that even to this day the interest in the different types of honey has not stopped growing [2]. The article reviews the role of the consumption of honey in our country. We have analysed some of its physicochemical parameters (sucrose, hydroxymethylfurfural, diastase activity and water content).

EXPERIMENT

The first physicochemical analyses conducted after the collection of the samples were:

Determination of sucrose in compliance with BS (Bulgarian Standard) 3050, Section 2.3; 2.4

Description of the method:

Before conducting the tests, the sample must be properly homogenised – if it is crystallised, it needs to be placed in a hot water bath of up to 50°C.

Equipment: Volumetric flasks of 100 cm³, beakers of 100 cm³, pipettes of 10, 20, 25, 50 cm, Class A.

Determination of water content – Regulation No. 48, State Gazette, Issue 103/2003, Annex to Section 9, point 3

Description of the method:

This method is based on the correlation between the refraction coefficient and the water content of honey. The correlation table is made by determining the refraction coefficient. The water content is determined by refraction only.

Equipment: Refractometer ABBE – Prizma Model, Calibration Certificate 115K/28.11.2017, Interlab Laboratory Complex Sofia.

Determination of hydroxymethylfurfural levels; Winkler method – Regulation No. 48, State Gazette, Issue 103/2003, Annex to Section 9, point 8.1

Description of the method:

This method is based on the determination of the optical density at 550 nm of the coloured solutions resulting from the interaction between the hydroxymethylfurfural, para-toluidine and barbituric acid contained in honey.

Equipment: Spectrophotometer – Jenway, measuring optical density at 550 nm, beakers, test tubes of 10 ml, pipettes of 1, 2, 5 and 10 ml, volumetric flasks of 50 and 100 ml.

Determination of diastase activity - Regulation No. 48, State Gazette, Issue 103/2003, Annex to Section 9, point 7

Description of the method:

This method is based on the determination of the quantity of the decomposed starch under specific conditions of the diastase in honey. The intensity of the blue solutions of undiluted starch and iodine in the incubation solution is determined at specific intervals. A graph is generated displaying the interdependence of time and the decreasing extinction (optical density) of the blue solutions. The graph is used to determine the time t, x necessary to reach extinction of 0.235. The diastase number is calculated by division by 300 c t.

Equipment: Hot water bath - WNB14, Memmert, Spectrophotometer - Jenway, Digital timer, Calibration Certificate No. 0534 of 15 April 2019. Measuring Equipment Calibration Laboratory Unisyst; pH meter, HI 2020-02, HANNA instruments, Calibration Certificate No. 50 E/10 May 2018. Laboratory Complex InterLab, Sofia; Dryer INB 200, C2071869, Memmert.

RESULTS AND DISCUSSION

The honey samples were analysed in relation to the following physicochemical parameters: sucrose, water content, HMF, and diastase activity. The results are presented in Table 1. The tests were performed in the period from June to August. Each sample was analysed twice. The analysis and visualization of the data were made in MS Excel. They give us information about the quality of the honey. The analysis of the results shows that the sucrose content is within the range of 1.7% to 3.59%. The higher content of sucrose in the samples tested in June is probably due to the supplementary feeding of the bee colonies. According to the Bulgarian regulations, the content of sucrose must not exceed 5%. Hydroxymethylfurfural – 2.00 mg/kg – 2.25 mg/kg, which shows an excellent quality of the honey. The regulations of ПCM196 provide for no more than 80 mg/kg of hydroxymethylfurfural. The diastase activity of the tested samples is from 25.00 to 41.00 Schade units. The regulations of ПCM196 provide for diastase activity of not less than 8 Schade units. The water content of the tested honey samples is from 17.00% - 18.80%. The regulations of ПCM196 provide for no more than 20% of water content.

Table 1. Physicochemical parameters of honey

No.	Parameter	Period	Measuring units	Results
1	Sucrose	June	%	3.59
2	Hydroxymethylfurfural		mg/kg	2.00
3	Diastase activity		Schade units	25.00
4	Water content		%	18.80
1	Sucrose	July	%	2.48
2	Hydroxymethylfurfural		mg/kg	2.12
3	Diastase activity		Schade units	38.00
4	Water content		%	18.00
1	Sucrose	August	%	1.70
2	Hydroxymethylfurfural		mg/kg	2.25
3	Diastase activity		Schade units	41.00
4	Water content		%	17.00

The classification of the health benefits of honey is based on its healing properties which are used in our traditional medicine and on the healing properties included in various scientific publications. Honey is a natural product comprising more than 400 biologically active substances, which is widely used in contemporary human diets. During the development of ancient civilizations honey was used not only as a food source, but also as a healing, cosmetic, and conserving substance [4]. The honey production regions in Bulgaria are determined by the availability of the vegetation required for beekeeping. There are more than 1,500 plant species in Bulgaria that produce nectar and pollen. Out of these, 250 are relevant to beekeeping. Nectariferous plants belong to forest, grass and shrub species. The forests are the best preserved and most common form of natural vegetation. From the perspective of beekeeping in the Strandzha Mountain, the forests of interest are the oak forests where honeydew honey (oak forest honey) is produced.

A survey was conducted over the period of the study to analyse the consumer interest in the consumption of honey. The data collected from the survey have been processed with the help of the MS Excel application and the results have been statistically analysed.

Figure 1 shows that the consumers who eat honey **on a regular basis**, i.e. those who answered 'yes' are 52.5%, while those who answered 'no' are 47.05%. In conclusion, we can say that those whose answer contained 'yes' are 5.45% more than those whose answer contained 'no'.
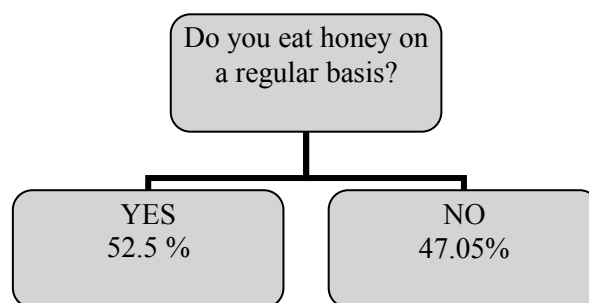

Fig. 1 Survey on honey consumer attitudes

CONCLUSION

This study aims to raise the awareness of the general population on how to select healthier food products. The survey conducted among the Bulgarian consumers over the cited period shows that Bulgarians make smarter choices of food products when they improve their consumer awareness, are better informed and wish to improve their quality of life. The honey produced in Bulgaria has outstanding properties and is fully consistent with the requirements of the national legislation.

REFERENCES

1. Regulation on the requirements for honey produced for human consumption adopted with Order No. 196 / 28 August 2021 effective as of 1 August 2003; 2. Dinkov, D., *Veterinary Sanitary Inspection of Honey*, 2013, p.56-79
3. Garchev, R., *Practical Seminars in Physiology, ARSO* Medical Literature Publishers, Sofia 2015 p.199-217
4. Baykova, D. – *Lose Weight without Hunger*, 2013.

COMPARISON OF GROWTH OF ASPERGILLUS ORYZAE AND SACCHAROMYCES CEREVISIAE ON COFFEE GROUND

Galina Yordanova
E-mail: burdelova@abv.bg

ABSTRACT

Coffee grounds are a large amount of waste and a serious environmental problem. The possibilities to grow and develop two types of microorganisms, Aspergillus oryzae and Saccharomyces cerevisiae, on coffee grounds for the purpose of waste utilization were studied. It was found out that both types of microorganisms, mold and yeast, are able to grow only on the sediment, without the addition of other carbon sources. As the concentration of the precipitate increases, so does the growth of the cells. This gives us prospects for further research and production of organic products.
Key words: Aspergillus oryzae, Saccharomyces cerevisiae, coffee ground

INTRODUCTION

Coffee is the second largest traded commodity in the world after oil, and therefore the coffee industry is responsible for generating large amounts of residues. The popularity of coffee as a main beverage has also brought unwanted side effects, as the production, processing and consumption of coffee are accompanied by impressive amounts of coffee-related waste that can pose a threat to the environment. Significant amounts of waste are generated from coffee production, the most abundant being from spent coffee grounds during roasting of the beans and in the preparation of instant coffee. The waste coffee grounds are solid residues obtained during the treatment of raw coffee powder with hot water or steam for the preparation of instant coffee. Most of these residues, however, remain unused, disposed of in the environment or incinerated for non-environmental disposal. They cause severe environmental pollution due to their toxic nature, and combustion leads to the production of carbon dioxide. These residues are toxic and after direct discharge into nearby reservoirs can cause serious environmental and health problems.

Coffee residues are generated in large quantities from the processing and consumption of coffee. These residues are usually considered waste and are disposed of due to improper management practices [1]. In solid fermentation, fungal strains, Aspergillus awamori and Aspergillus oryzae, have been used to support microbial growth on coffee grounds. Tracking of chemical changes that occur during fermentation shows that coffee residues contain chemical compounds that can be used by microorganisms in bioprocesses to produce value-added products. Growth of fungal hyphae, an increase in free amine nitrogen and total reducing sugars are observed on coffee residues. The reuse of sludge as a feedstock for ethanol production is of great interest for biofuel production as well as for adding value to this agro-industrial waste [2].

Studies on various fungal strains of the genera Aspergillus, Mucor, Penicillium and Neurospora have found growth and release of phenolic compounds on coffee residues. All strains manage to develop on coffee grounds. Solid fermentation is a valuable alternative for the reuse of agricultural and agro-industrial residues, as it can be used for the production and extraction of compounds such as enzymes, flavors, pigments, organic acids and so on. Phenolic compounds are widely used in the food and pharmaceutical industries and thus the extraction of these compounds can be a valuable alternative for the exploitation of coffee grounds [3]. And the filamentous fungi Aspergilus oryzae are also widely used for the production of hydrolytic enzymes for industrial purposes [4].

Other authors have studied the yeasts used in the coffee industry and found out that they play a major role in the treatment of coffee grounds for coffee waste extraction, especially spent coffee grounds in the form of organic biomass, biofuels and others [5]. The use of sludge for bioethanol

production is due to the content of carbohydrates in the sludge, which can be fermented by Saccharomyces cerevisiae [6]. In the production of ethanol based on the fermentation of coffee husks from Saccharomyces cerevisiae, it was found out that the fermentation yield decreases with the increase of yeast concentration. Such results show that coffee husks present an excellent potential for ethanol production based on these residues [7].

Another study evaluated sugar metabolism and ethanol production from three different yeast strains (Saccharomyces cerevisiae, Pichia stipitis and Kluyveromyces fragilis) when cultured in sugar-rich hydrolysates obtained by hydrolysis of coffee bean acid. Saccharomyces cerevisiae provides the best ethanol production from coffee grounds. The reuse of the main waste from the coffee industry is essential from an environmental and economic point of view. Therefore, to use coffee processing waste to produce bioethanol, which provides an alternative source of energy from waste biomass and solves the ecological waste disposal, as well as the human health problem is important [8]. A study was made on the joint use of the two types of microorganisms in coffee pulp. Coffee pulp, which is an agricultural waste obtained from the processing of coffee beans, is used for the production of bioethanol. The experiment was performed by separate hydrolysis and fermentation process using Aspergillus niger and Saccharomyces cerevisiae. The study shows that the joint culture of Aspergillus niger and Saccharomyces cerevisiae gives an effective result. The use of coffee cellulose for the production of biofuel or bioethanol has the advantage for regions with intensive coffee production. Coffee pulp has a high concentration of carbohydrates and is a likely raw material for bioethanol production [9].

The most commonly used and effective microorganisms for alcoholic fermentation are yeasts of the species Saccharomyces cerevisiae, as well as molds of the species Aspergillus oryzae. Which are more suitable as growth and for utilization of coffee grounds is the subject of study in this paper.

MATERIALS AND METHODS

1. Materials
Coffee grounds are collected from a coffee vending machine and air-dried.
Microorganisms:
Aspergillus oryzae and Saccharomyces cerevisiae were provided by the Department of Biotechnology, Faculty of Technical Sciences, Burgas University "Prof. Dr. Assen Zlatarov", Bulgaria. Cultures of the investigated strains were maintained on Beer agar at 29-30°C in order to obtain dense sporulation and stored at 4°C in a refrigerator.
Culture conditions:
In 500 cm^3 flasks a poor nutrient medium Chapek-Dox is put and a certain amount of coffee grounds is added. After sterilization and cooling of the medium, a wash of the microorganism is added. The closed flasks are placed in a thermostat at 29-30°C for 24-hour fermentation.

2. Methods
Microscopic preparations are used to monitor the development of the two microorganisms on the coffee grounds. Cell counting is performed with Tom's camera.

RESULTS AND DISCUSSION

The condition of the culture at the beginning and at the end of the process was monitored, namely after 24 hours of fermentation. The initial measurement of the number of microorganisms before sowing was: Aspergillus oryzae 10.107 cells ml-1 and Saccharomyces cerevisiae 1.9.107 cells ml-1.
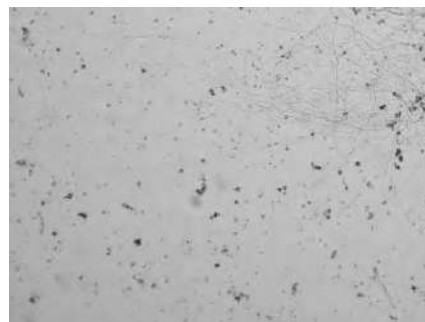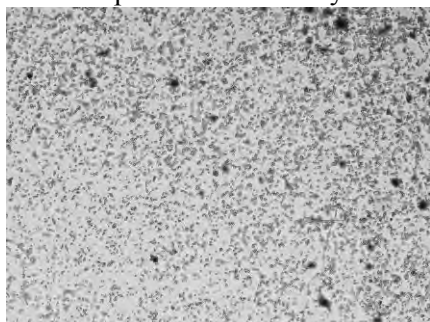

Fig. 1 Sample of *Aspergillus oryzae* without coffee grounds at 0 h and at 24 h
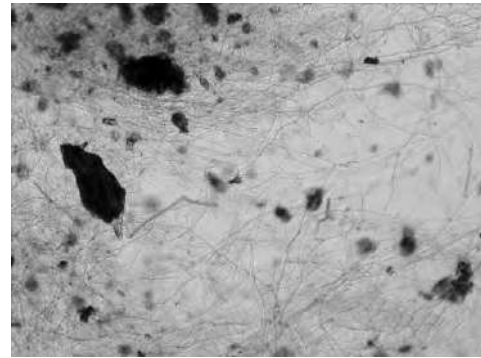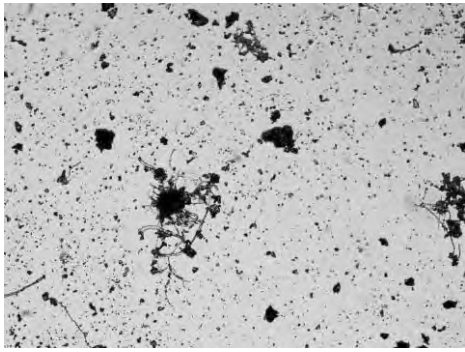
Fig.2 Sample after 24 hours *Aspergillus oryzae* with 10 g.l^{-1} coffee grounds and 20 g.l^{-1} coffee grounds
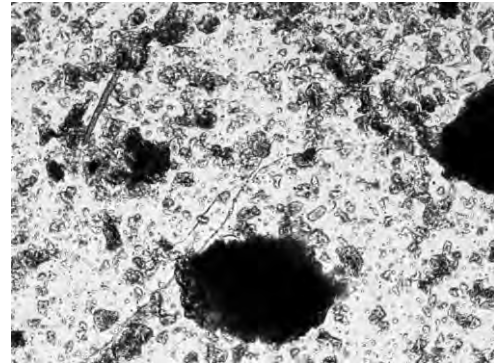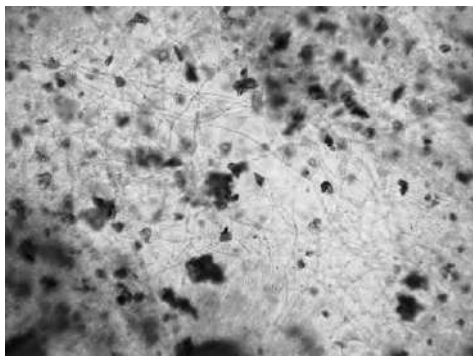

Fig.3 Sample after 24 hours *Aspergillus oryzae* with 30 g.l^{-1} coffee grounds and 50 g.l^{-1} coffee grounds

In subsequent samples, as the amount of sludge increases, so does the number of hyphae. Fig. 3 shows a rapid development of mold fungi, and at 50 g.l-1 coffee grounds a layering of the picture from the sediment begins.

Subsequent measurements were performed with yeast of the species Saccharomyces cerevisiae.
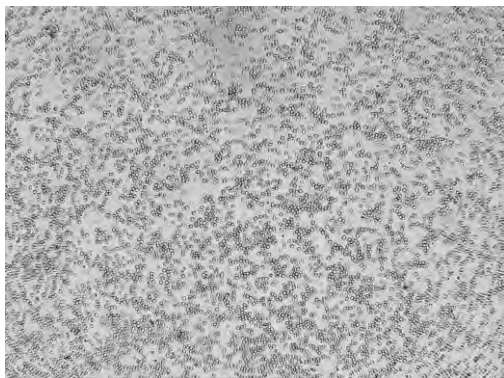
Fig. 4 Sample *Saccharomyces cerevisiae* without coffee grounds at 0 h and after 24 h.

As with molds, at the beginning and end of the process (after 24 hours) there is a slow increase in the number of cells. In the following samples with 10 g.l-1 coffee grounds and with 20 g.l-1 coffee grounds similarly, as the amount of precipitate increases, so does the number of yeast cells (Fig. 4).
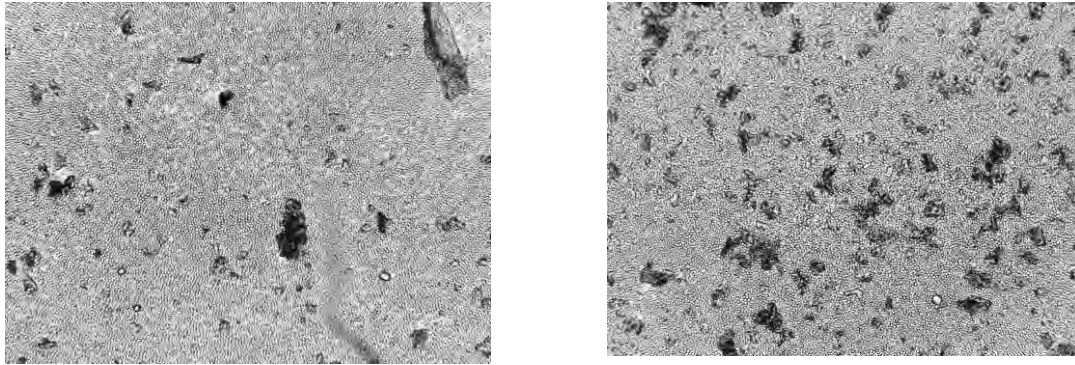
Fig. 5 Sample after 24 hours *Saccharomyces cerevisiae* with 30 g.l^{-1} coffee grounds and 50 g.l^{-1} coffee grounds

From the photographs in Fig. 5, a rapid development of yeast cells can be observed, both with 30 g.l-1 coffee grounds and with 50 g.l-1 coffee grounds, the cells are literally adjacent. The accumulation of cells from the coffee grounds begins to increase with the amount of coffee. The examinations and microscopic photos show that the yeast cells develop a little better and relatively faster than the molds on the coffee grounds. This directs us to search for the right combination of the two types of microorganisms for the recovery of coffee waste.

CONCLUSION

The recovery of waste such as coffee grounds is a prospect for the future of mankind. Through microorganisms, the absorption of waste is associated with minimal costs and preservation of the environment. The study found out that the molds Aspergillus oryzae and the yeast Saccharomyces cerevisiae are able to use coffee grounds for their growth and development without adding additional sources. Microscopic photographs show that yeast grows relatively faster than mold fungi. But it is also related to the type of microorganism and the time required for development, which shows that molds need a longer period of time.

REFERENCES

1. Solange I., A Mussatto, M.S. Erchlia, A. Machado, M. Lhvia Carneiro, A. Josu. *Sugars metabolism and ethanol production by different yeast strains from coffee industry wastes hydrolysates*. Teixeira a Applied Energy 92 (2012) 763–768.

2. Obayuwana I. and O. C. Eigbike. *Bioprocessing: A Solid State Fermentation of Coffee Residues Procedure*. International Journal of Agriculture and Earth Science Vol. 2 No.4 (2016) ISSN 2489-0081.

3. Erchlia M.S. Machado, Rosa M. Rodri-guez-Jasso, Josu A. Teixeira, Solange I. Mussatto. *Growth of fungal strains on coffee industry residues with removal of polyphenolic compounds*. Biochemical Engineering Journal Volume 60, (2012), Pages 87-90, ISSN1369.

4. Shruti P., M. Arora, Loveleen Sarao. *Production and optimization of amylase and glucoamylase using Aspergillus oryzae under solid state fermentation*. International Journal of Research in Pure and Applied Microbiology. (2013); 3(3): 83-88.

5. QianLi Yu-YouLi, W. Q. Xiaochang, W. K. Takayanagi. *Sulfate addition as an effective method to improve methane fermentation per-formance and propionate degradation in ther-mophilic anaerobic co-digestion of coffee grounds, milk and waste activated sludge with AnMBR*. Bioresource Technology, Volume 185, June (2015), Pages 308-315.

6. Valderez M., L. Ponte Rocha , J. Brandão, L. Matos, L. Pinto deLima, P. Marciano da Silva Figueiredo, I. Larissa, L. Fabiano, A. N. Fernandes, L. Rocha, B. Gonçalves. *Ultrasound-assisted production of bio-diesel and ethanol from spent coffee grounds*. Bioresource Technology, Volume 167, September (2014), Pages 343-348.

7. Godoy P., Á. Mourenza, S. Hernández-Romero, Je. González-López and Ma. Manzanera. *Microbial Production of Ethanol From Sludge Derived From an Urban Wastewater Treatment Plant*. Department of Microbiology, Front Microbiol. (2018); 9: 2634.

8. Carolina A., V. Montoya, R. Cristina da S. Mazareli, T. P. Delforno, V. B. Centurion, I. K. Sakamoto, V. Maia de Oliveira, E. LuizSilva, M. Bernadete, A. Varesche. *Hydrogen, alcohols and volatile fatty acids from the co-digestion of coffee waste (coffee pulp, husk, and processing wastewater) by applying autochthonous microorganisms*. International Journal of Hydrogen Energy, Volume 44, Issue 39, 13 August (2019), Pages 21434-21450.

9. Kousar H. and K.R. Navitha. Bioethanol Production Using Aspergillus Niger And *Saccharomyces Cerevisiae From Coffee Pulp By Separate Hydrolysis And Fermentation Process*. October (2020). International Journal of Scientific & Technology Research 09(01):2853-2855.

ACTIVITY OF LACTASE PRODUCED FROM *ESCHERICHIA COLI* AND *ASPERGILLUS ORYZAE*

Dimitrina Krasteva, Reni Syarova, Zlatina Chengolova
E-mail: zlatinabe4eva@abv.bg

ABSTRACT

Lactose is disaccharide present in milk but a large number of the world population suffer from lactose intolerance. Therefore, many dairy factories produce lactose-free milk using microbial enzymes. The enzyme that cleaves the glycoside bond in the disaccharide is called lactase. In this study, bacterial and micro-fungus lactase were compared. The activity and thermal stability of the enzymes were determined. The lactase from E. coli had faster reaction, but the lactase from Asp. oryzae could react with larger amounts of the substrate.

***Key words:** lactose, lactase, ONPG, activity, milk*

INTRODUCTION

Lactase is an enzyme in the small intestine. The role of the enzyme is to hydrolyze the disaccharide lactose [1]. According to enzyme classification and nomenclature, lactase is in the class of hydrolases [2] and the EC number of the lactase from the intestinal mucosa is EC 3.2.1.108 (http://www.enzyme-database.org). The reaction determined by the enzyme starts with lactose and water and ends with D-galactose and D-glucose. The systematic name of the enzyme is lactose galactohydrolase.

A similar reaction is caused by the enzyme β-galactosidase (EC 3.2.1.23), which is often called lactase. The enzyme catalyzes the hydrolysis of terminal non-reducing β-D-galactose residues in β-D-galactosides. The systematic name of the enzyme is β-D-galactoside galactohydrolase (http://www.enzyme-database.org). The enzyme is often used in laboratory investigations and in lactose-free milk production.

Both of the described enzymes catalyze hydrolysis of the lactose. Lactose is the main carbohydrate found in milk. It is a disaccharide consisting of glucose and galactose which are linked by a β-1,4 glycosidic bond [3]. The lactose represents approximately 98% of the sugars in milk and it is not found in any other food. The main function of the lactose is to provide galactose to new-born mammals to form the nerve structures (myelin sheaths) [4], and lactose is also the main source of energy for the heart, liver and kidneys [5].

Lactose gives the slightly sweet taste of the milk. It appears as a D-isomer that has two anomeric forms (α- and β-, ratio 2:3) [4]. Furthermore, lactose has lower sweetness than sucrose. On a 100-piont scale, sucrose has 100, and α-lactose has 20, β-lactose has 50. Also, it has a lower glycemic index (46) than that of sucrose (68) [5].

Digestion and absorption of the lactose happen in the small intestine. Lactase has α-glucosidase activity and cleaves disaccharide to monosaccharides glucose and galactose. The monosaccharides are actively transported to enterocytes and the glucose moves to surrounding capillaries by facilitated diffusion [6]. Around 70% of the world's adult population has lactase limited expression. Lactose malabsorption may cause numerous painful symptoms. They can be gastrointestinal symptoms such as abdominal pain, bloating, borborygmi, nausea, diarrhea, constipation, or extraintestinal symptoms such as headache, muscle pain, eczema, etc. [7]. Consequently, consumers with those symptoms prefer lactose-free milks which are produced by using lactase.

In this study, two lactase enzymes were compared. One was produced from micro-fungus – *Aspergillus oryzae* and the other was produced from bacteria – *Escherichia coli*. The thermal stability of the enzymes was tested, and the ac-

tivity to various concentrations of specific substrate was analyzed.

EXPERIMENT

The analyses were performed with two enzymes: lactase produced from *Escherichia coli* (120 units/mg), and lactase produced from *Aspergillus oryzae* (4 500 FCC/mL). The lactase (from *Asp. oryzae*) was purchased from the local pharmacy. The trade name of the reagent is Colactase. All +the other reagents (including lactase from *E. coli*) were purchased from Sigma-Aldrich (Germany). The colour reactions were performed by using 2-nitrophenyl β-D-galactopyranoside (ONPG). The spectrophotometric analyses were made with a Jenway UV/Vis 7205 spectrophotometer.

Two buffers were used in the assay. The first was 0.1 M PBS pH 6.8, and the other was 0.1 M PBS pH 6.8 containing 10 mM $MgCl_2$. The first one was used to prepare the enzyme solution, and the other for the substrate solutions. A solution with 1 M Na_2CO_3 was used as a stop solution. Both tested enzymes were prepared at concentration 1 mg/mL. The substrate solutions with ONPG were prepared just before the analysis at the desired concentrations.

Enzyme-substrate mixture was prepared by loading 10 μL of the enzyme solution (lactase produced in *E. coli*) and 100 μL of 10 μM ONPG in a vial and the mixture was loaded to 1 mL with 0.1 M PBS pH 6.8. The reaction mixture was allowed to react for 5 min and absorbance measurements were performed (at 2.5 min, and at 5 min). The absorbance of the samples was read at wavelength from 200 nm to 800 nm. After that, 200 μL stop solution was added and the absorbance was measured again.

The activities of the lactases produced from *Asp. oryzae* and from *E. coli* were analyzed. Enzyme (from *Asp. oryzae* or *E. coli*) 10 μL was loaded in a cuvette with 100 μL of 10 μM ONPG and 890 μL 0.1 M PBS pH 6.8. Single measurements of the absorbance at 395 nm were performed every 20 sec. The data were collected and the slope of the obtained graphical expression was calculated.

Lactase from *E. coli* (10 μL) was tested with two different concentrations of ONPG substrate (100 μL): 1 μM and 10 μM. The mixtures were diluted with 0.1 M PBS pH 6.8 to 1 mL. The reaction was observed with the spectrophotometer at wavelength 395 nm.

The thermal stability and activity of the enzymes (from *Asp. oryzae* and from *E. coli*) were tested by loading each of the enzymes in boiling water for 25 min. After that the enzyme substrate reaction was tested (10 μL enzyme + 100 μL substrate + 890 μL 0.1 M PBS pH 6.8). The substrate was prepared at different concentrations from 100 μM to 1.56 μM at 2-fold dilutions. The mixtures reacted for 4 min and stop solution (20 μL) was added. The absorbance was read at 417 nm, and from 200 nm to 600 nm.

RESULTS AND DISCUSSION

The substrate ONPG contained D-galactose coupled with *o*-nitrophenol. The enzyme reaction was traced by observing the colour of the obtained reaction mixture – enzyme lactase with ONPG. Ortho-nitrophenol coloured the mixture yellow (Fig. 1). All analyses were performed with the spectrophotometer to evaluate the amount of the resulting product.

Fig. 1 ONPG enzyme hydrolysis by lactase (control – left, reaction – right).

The first step before rating the enzyme-substrate reaction was to determine the optimal wavelength for single measurements. The obtained maximum before adding the stop solution was at 395 nm and after that at 417 nm (Fig. 2). There was a slight shift of the maximum due to the increased pH value after the stop solution addition.
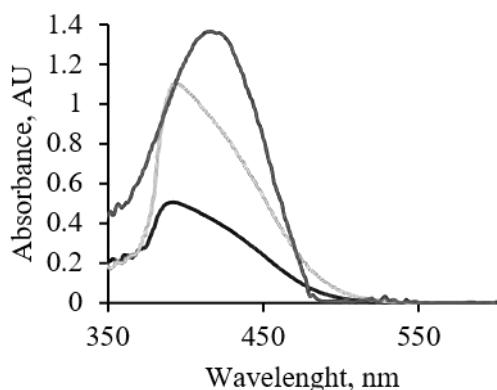
Fig. 2 Absorption maximums of the product of the enzyme reaction (lactase + ONPG) at 2.5 min (blue), at 5 min (yellow) and after adding stop solution (red).

Two enzymes were compared: lactase produced from *Asp. oryzae* and lactase produced from *E. coli*. Both enzymes were mixed with equal volumes of substrate and the reaction process was observed (Fig. 3). Slopes of the obtained linear ranges were: 0.0042 from lactase from *E. coli*, and 0.0017 lactase from *Asp. oryzae*. This showed the more intense reaction of the enzyme from the bacteria compared to the lactase from the micro-fungus. Consequently, bacterial lactase could "consume" the substrate amount in the sample faster.
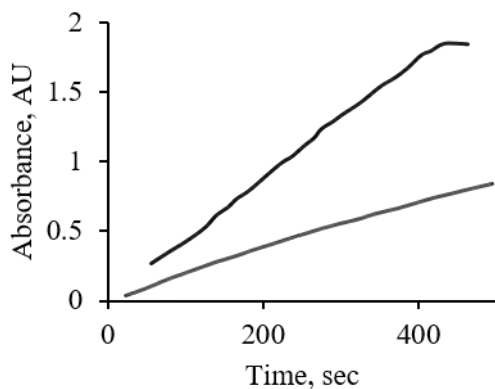
Fig. 3 Time-dependence graphic of lactase (from *E. coli* – blue, from *Asp. oryzae* – red) reacting with ONPG.

The bacterial enzyme was tested with two ONPG concentrations (Fig. 4). Substrate concentration 10 μM was better for observing the reaction. The lower ONPG concentration was not enough and the enzyme reacted with the whole amount of the substrate for around 1 min. The

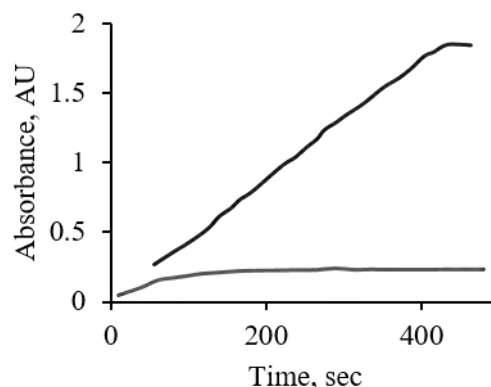other analyses were performed with the higher (10 μM) ONPG concentration.

Fig. 4 Lactase from *E. coli* time-depending reaction with 1 μM (red) and 10 μM (blue) ONPG.

Both of the tested enzymes were inactivated at 25 min in boiling water. Consequently, they were not able to hydrolyze the lactose in milk if the enzymes were loaded in raw milk before its boiling. The spectral analyses of the enzyme-substrate samples (heated and native enzyme) were made (Fig. 5). Both heated enzymes had similar results and the substrate ONPG was not hydrolyzed. The samples with native enzyme contained the rection products (galactose and *o*-nitrophenol), so the absorbance measurements showed maximums at: 290 nm and 417 nm. The mixture of heated inactive enzyme and ONPG substrate showed a large peak with a maximum at 310 nm.
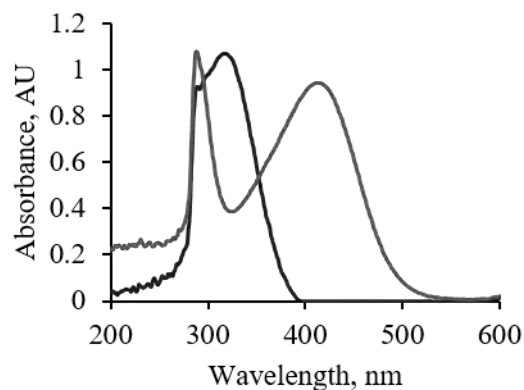

Fig. 5 Spectral analyses of heated inactive (blue) and native active (red) lactase from E. coli with ONPG substrate.

The activity of native enzymes from both producers was analyzed with different concentrations of the substrate (Fig. 6). The bacterial enzyme showed a capacity to 12.5 μM ONPG, and

the micro-fungus enzyme – 25 µM ONPG. Consequently, the lactase from *Asp. oryzae* can react with s higher concentration of the substrate, but the slope of the curve is lower, so the hydrolysis reaction is slower. The lactase from *E. coli* reacts with ONPG wildly, which is obvious from the slope of the curve, and it can spare time for sample processing.
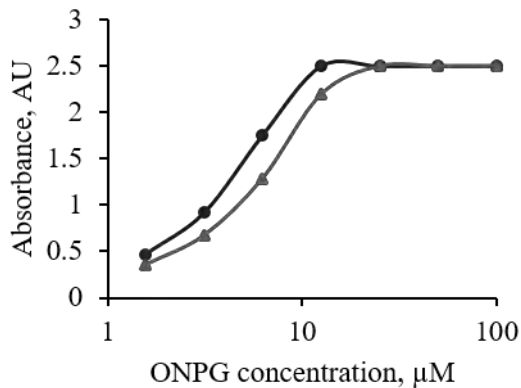

Fig. 6 Comparison of the lactase from *Asp. oryzae* (▲) and lactase from *E. coli* (●) hydrolyzing different ONPG concentrations.

Both tested enzymes showed satisfactory results with ONPG used as a substrate. Similar reactions were observed with various concentrations of the substrate. Also, it was discovered that the bacterial and micro-fungus enzymes are highly thermo labile. Therefore, it is not recommended to add them to raw milk before it is boiled when producing lactose-free milk.

REFERENCES

1. Colaizy, T. T., Demauro, S. B., Mcnelis, K. M., & Poindexter, B. B. (2018). *Enteral Nutrition for the High-Risk Neonate*. In Avery's Diseases of the Newborn (pp. 1009-1022). Elsevier.
2. McDonald, Andrew G; Boyce, Sinead; and Tipton, Keith F (April 2015) *Enzyme Classification and Nomenclature*. In: eLS. John Wiley & Sons, Ltd: Chichester. DOI: 10.1002/9780470015902.a0000710.pub3
3. Churakova, E., Peri, K., Vis, J. S., Smith, D. W., Beam, J. M., Vijverberg, M. P., ... & Winter, R. T. (2019). *Accurate analysis of residual lactose in low-lactose milk: comparing a variety of analytical techniques*. International dairy journal, 96, 126-131.
4. Gambelli, L. (2017). *Milk and its sugar-lactose: A picture of evaluation methodologies*. Beverages, 3(3), 35.
5. Strzałkowska, N., Jasińska, A. J., & Jóźwik, A. (2018). *Physico-chemical properties of lactose, reasons for and effects of its intolerance in humans – a review*. Animal Science Papers and Reports, 36(1), 21-31.
6. Misselwitz, B., Butter, M., Verbeke, K., & Fox, M. R. (2019*). Update on lactose malabsorption and intolerance: pathogenesis, diagnosis and clinical management*. Gut, 68(11), 2080-2091.
7. Facioni, M. S., Raspini, B., Pivari, F., Doglitti, E., & Cena, H. (2020). *Nutritional management of lactose intolerance: The importance of diet and food labelling*. Journal of Translational Medicine, 18(1), 1-9.

SMALL BROAD-BAND IMMERSION TRANSDUCERS FOR INVESTIGATION OF PELTIER MODULE

Radostin Kasarov
E-mail: diagnostika.kasarov@abv.bg

ABSTRACT

Six different notches on a single penetrameter have been examined using the ultrasonic immersion technique. Six types of middle and small size transducers with frequencies of 4MHz and 10 MHz have been used. A comparison of the acoustic signals reflected from the investigated penetrameter is presented. Measurements of the ultrasound path and wave attenuation have been accomplished. On the basis of ultrasonic investigations, proper transducers for characterizing the thermoelectrical properties of Peltier modules are selected.

Key words: *immersion ultrasonic method, ultrasonic attenuation, sensitivity, screen resolution, Peltier module*

INTRODUCTION

Ultrasonic testing is a non-destructive technique for examination of solid (typically metallic or ceramic) components and materials. It can be used for detection of cracks and flaws as well as for material characterization [1, 2, 3]. The ultrasonic test method operates on the principle of injecting a very short pulse of ultrasound from a transducer into a component, and then receiving and analyzing any reflected sound pulses. The frequency of ultrasound pulses must be carefully selected to provide a proper balance between image detail and depth of penetration. In general, high frequency pulses produce higher quality images but cannot penetrate very far into the test material.

The major element within the transducer is a crystal designed to vibrate with the desired frequency. A transducer is often designed to vibrate with only one frequency, whch is its resonant frequency. Therefore, the only way to change ultrasound frequency is to change transducers. This is a factor that must be considered when selecting a transducer for a specific experimental procedure. Certain frequencies are more appropriate for certain types of examinations than others. The ability to conduct and interpret the results of an ultrasound examination depends on a thorough understanding and practical experimentation of these ultrasound interactions.

Typically, a researcher scans a transducer on the surface of the component in such a way as to check the entire area needed to be tested by scanning motion. One of the ways to couple the sound from a transducer to a tested object is to apply a liquid, usually water, which conducts the sound between the probe and test material. This technique is known as immersion testing. In immersion testing, the transducer is placed in the water, above the tested object, and a beam of sound is projected.

EQUIPMENT

Typical experimental equipment consists of two immersion transducers, a USIP 11 Krautkramer-Branson ultrasonic analogue analyzer and a special specimen – a penetrameter, controlled by UV-radiation [4]. The transducers are selected to transmit compression waves of 4 and 10 MHz into the material at a chosen focal distance shown in Table 1.

The penetrameter is made of titanium with a thickness of 3.94 mm as a Peltier Module [5]. Its length is 50 mm and its width is 15 mm and it has six notches (steps) with sizes shown in Table 2.

Table 1. Transducer characteristics, Focal Distance and Frequency Range

Transducer	Element Size [mm]	Focal* distance [mm]	Ultrasonic wave shape	Frequency range [MHz]
Z4KL20	Ø 10	20	detachable collar line focus	0.8 - 8
Z4KP20	Ø 10	20	detachable collar point focus	0.8 - 8
Z10ML15	Ø 5	15	line focus	2 - 20
Z10MP15	Ø 5	15	point focus	2 - 20
L 5 M**	Ø 5	20	line focus	2 - 8
L 10 M**	Ø 5	20	line focus	10 - 15

*Near field length – Freshnel zone, ** Broad-band transducer

Table 2. Notches (Steps) characteristics

Size	Step No.1	Step No.2	Step No.3	Step No.4	Step No.5	Step No.6
Length [mm]	15	15	15	15	15	15
Depth [mm]	2.55	2.08	1.45	1.09	0.85	0.69
Width [mm]	2.7	2.05	1.48	1.08	0.76	0.41

EXPERIMENT

The test penetrameter is positioned in a small water-filled tank. An ultrasound probe is then moved on a horizontal axis at a constant distance to the penetrameter (Fig. 1). The sound travels through the water and into the penetrameter. Following the sound's interaction with the exterior and interior microstructure, any flaws that may exist, or with the inner surface of the component, the echoed sound wave returns to the probe.

RESULTS

The image of soundwave peaks, using the immersion method, is slightly different from the contact technique. In this case there is an additional peak between the initial pulse and the back wall peaks caused by the sound wave going from the water to the test material. The arrival time of the echo and its amplitude enable interpretation of where and what it is originating from in the material. Some energy is lost when the waves hit
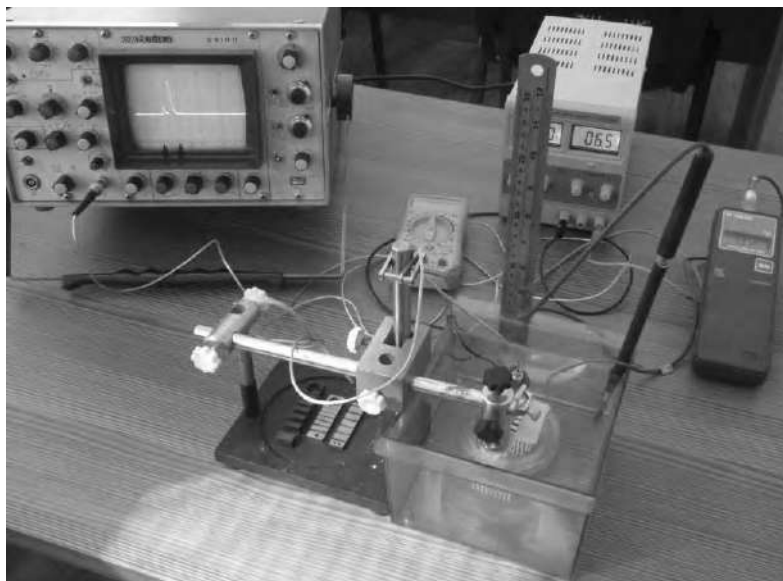
Fig. 1. Experimental set-up

the test material, so the front wall peak is slightly lower than the peak of the initial pulse. The rate at which an ultrasound pulse is absorbed generally depends on two factors: the material through which it passes and the frequency of the ultrasound. The attenuation rate is specified in terms of an attenuation coefficient. Its value for water is 0.002 dB/cm.

The USIP 11 ultrasonic analogue analyzer has been adjusted to ignore the initial pulse peak, so the first peak it will show is from the front wall of the penetrameter (from the notches side). The data obtained by the used transducers for all penetrameter steps show different signal amplitude (Table 3). The results for attenuation of the ultrasound are presented in Fig. 3. A good resolution was obtained in the Z4KL20, L5M and L10M probes. The experimental results show that the highest signal amplitudes are observed for the Z4K type probes with a mean frequency of 4 MHz, and the lowest values were obtained when Z10M (10 MHz) type transducers were applied.

Table 3. Adjusting the sensitivity in dB for different types of transducers in respect to the registered back pulse echoes from penetrameter steps

Transducer	Step No.1	Step No.2	Step No.3	Step No.4	Step No.5	Step No.6
Z4KL20	32.5 dB	32 dB	31 dB	29.5 dB	29 dB	28.5 dB
Z4KP20	33 dB	32.5 dB	32.5 dB	31 dB	31 dB	31 dB
Z10ML15	47 dB	46 dB	45 dB	45.5 dB	45 dB	45 dB
Z10MP15	46 dB	45 dB	45 dB	45 dB	44 dB	44 dB
L5M	44 dB	43 dB	43 dB	42,5 dB	42 dB	40 dB
L10M	45,5 dB	45 dB	44 dB	44 dB	43,5 dB	42,5 dB

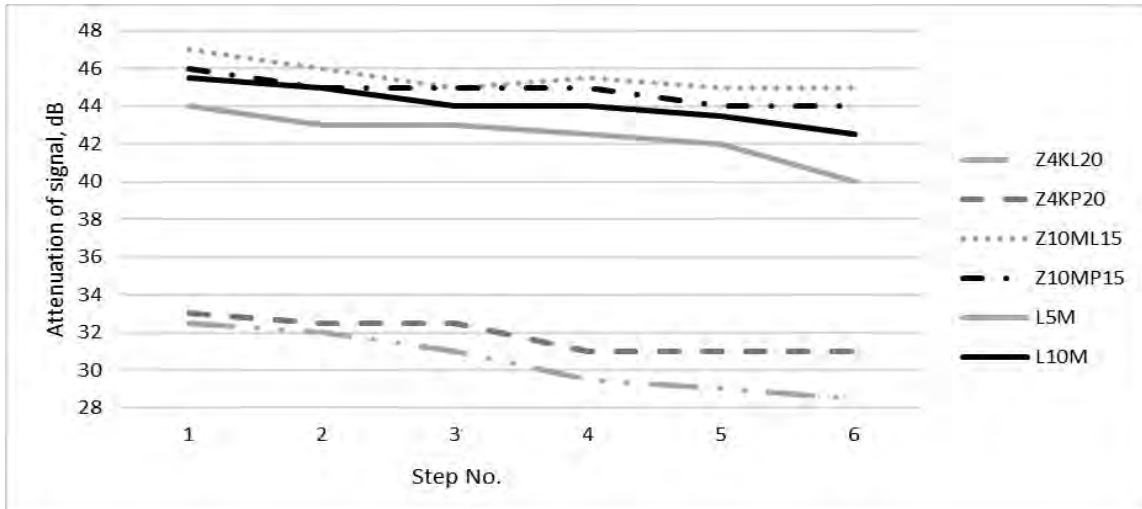**Fig. 2**. Position of probe

Fig. 3. Signal attenuation for selected transducers

Measurements of the distance between the applied transducers and each of the penetrameter steps have been carried out. A comparison of the values obtained with a micrometer shows some differences, which are presented in Fig. 4. As it can be seen, less deviation is observed in the Z4KL20 probe for the first four steps of the penetrameter. For the last two steps, a good coincidence of the results is noticed for the L5M and L10M transducers because of their high resolution. A maximal difference of 1.67 is obtained when the Z10MP15 probe is applied.
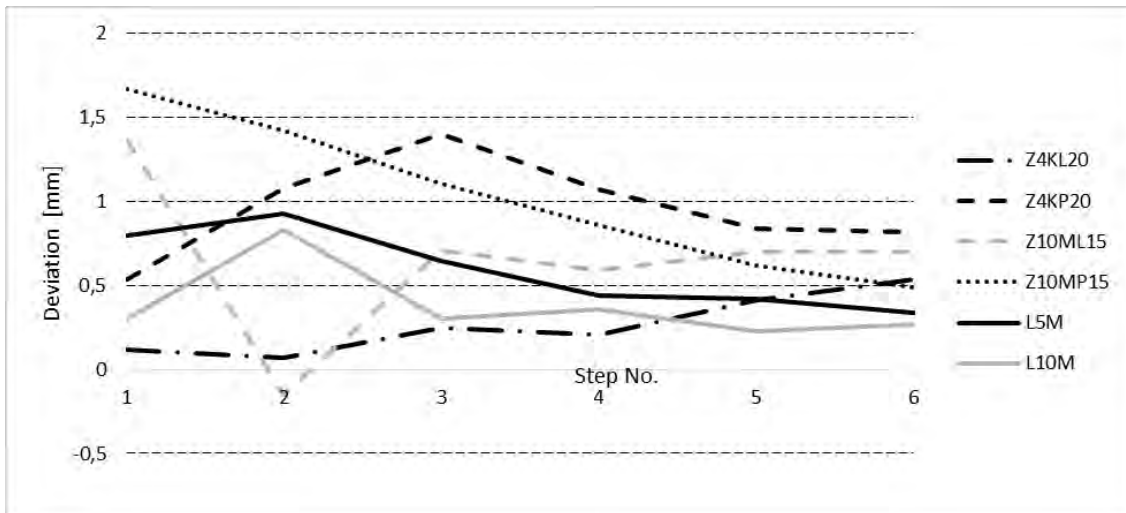
Fig. 4. Differences between micrometric and ultrasonic measurements

CONCLUSIONS

The conducted experiments show that the applied non-destructive testing method can serve as a comparison between the different materials in terms of structure and homogeneity, as well as for quality control without disturbing their integrity.

The results of the research conducted with the immersion method showed that we can confidently distinguish the steps with a different depth and width.

In ultrasound imaging the significance of wavelength is that short wavelengths are required to produce short pulses for good detail (in the depth direction) and this requires higher frequencies. The data obtained for all steps unambiguously shows a good signal resolution and amplitude in respect to the screen position of the Z4KL20, L5M and L10M.

The results are obtained with the optimal adjustment mode: sensitivity of 29-45 dB in the frequency range of 4-10MHz. With the same parameters for transducers Z4KL20 and Z4KP20 with detachable collar line and point focus we

get a higher amplitude, but lower resolution than that of the broad-band transducers L5M (5MHz) and L10M (10MHz).

Observations during the experiment show minimal but sufficiently distinct and well reproducible differences in a sample of the same thickness as Peltier Modules, which may be a criterion for characterizing the electrical and thermal properties of the Peltier Modules. The co-application of this method with electrical measurements ensures a better study and correct selection of Peltier Modules in respect to their applications in various electronic devices.

REFERENCES

1. Hübschen, G. *Ultrasonic techniques for materials characterization, In book: Materials Characterization Using Nondestructive Evaluation (NDE) Methods*, pp. 177-224.

2. Ramzi, R., M. F. Mahmod and E. Bakar. *Immersion ultrasonic inspection system for small scaled composite specimen, Journal of* Engineering and Applied Sciences 10 (22), 2015, 17146-17150.

3. Kasarov, R. *Investigation of Polymeric Materials by Means of Electro Acoustic Methods,* Assen Zlatarov University Annual, Vol. XLVII, Book 1, 2018, p.97.

4. Nikolaeva, Z. and T. Mihalev, *Modeling ultraviolet radiation for Burgas Municipality,* International Scientific on-line Journal Science & Technologies, Stara Zagora, Bulgaria, IV (3), 2014, pp. 15-19.

5. Belovski I., A. Aleksandrov, K. Teodosios. *Study of operation of Peltier modules in cascade,* International Scientific Conference UNITECH 2017 - Gabrovo, Proceedings, vol. 1, 2017, 207 – 211.

CALIBRATION OF 15MHz IMMERSION TRANSDUCER FOR INVESTIGATION OF PELTIER MODULE

Radostin Kasarov
E-mail: diagnostika.kasarov@abv.bg

ABSTRACT

Ultrasonic immersion technique has been applied to investigate a calibrated penetrameter with two flat bottom holes and six different notches. Transducers with frequencies 5MHz, 10MHz and 15MHz have been used. A comparison of the reflected acoustic signals has been carried out. Measurements of the ultrasound path and wave attenuation have been accomplished. On the basis of ultrasonic investigations, proper transducers for characterizing the thermoelectrical properties of Peltier modules are selected.

Key words: *immersion ultrasonic method, high-frequency transducer, ultrasonic attenuation, Peltier module*

INTRODUCTION

Ultrasonic technique is one of the basic non-destructive methods for detection of internal defects in parts, evaluation of structures, thickness gauging, and characterization of mechanical properties of materials, such as density and elastic moduli [1, 2, 3]. Typically, time of flight, attenuation, scattering and the change in the frequency spectrum of a wave in a test object have been measured to obtain information about the sample geometry and material properties.

The selection of a proper transducer depends on the testing conditions, geometry and material of the component under consideration. Very important factors are sound frequency, beam spread, near and far-field effects, reflection and refraction on boundaries of the test object. Vibration frequency of the transducer's active element determines the ultrasound wavelength within the studied item and thus affects the probability of reflection from a small internal discontinuity.

Most often transducers are chosen either to enhance the sensitivity or resolution of the system. Usually, high-frequency transducers (between 15 MHz and 25 MHz) have a great sensitivity to small discontinuities, but they provide lower energy and penetration depth in comparison to low-frequency transducers.

In the contact ultrasonic method, a transducer is placed directly on the sample under consideration. Usually, the aid of a coupling fluid and careful positioning of the probe are needed to obtain good results. The main source of errors in this method is the poor contact between the transducer and the samples with uneven, rough surfaces. This problem could be overcome by applying a fluid-assisted method. It is normally realized by setting the sample in a water tank that includes submerged transducers. In general, immersion testing offers excellent control over test variables and provides results of the highest quality.

In this paper, the possible application of a high-frequency immersion transducer for the study of a Peltier element is considered.

EQUIPMENT

Ultrasonic experiments have been carried out by means of a Krautkramer-Branson Flaw Detector, model USM 35XS, and two immersion transducers with central frequencies of 5, 10 and 15 MHz. In Table 1, the main characteristics of the selected probes are presented. Calibration block – a penetrameter with a size of 50 mm in length, 15 mm in width and 3.94 mm in thickness has been applied as a model of Peltier module. The penetrameter is made of titanium and is controlled by the UV-radiation [4]. The test block has six notches (steps) with sizes given in Table 2, and two flat bottom holes (Ø12 mm, h=3 mm and Ø1.5 mm, h = 0.94 mm), shown in Fig. 1.

Table 1. Transducers characteristics, Focal Distance and Frequency Range

Transducer	Element Size [mm]	Focal distance* [mm]	Ultrasonic wave shape	Frequency range [MHz]
L 5 M	Ø 5	20	line focus	0,8 - 8
L 10 M	Ø 5	20	line focus	2 - 20
L 15 M	Ø 5	20	line focus	2 - 20

*Near field length – Freshnel zone

Table 2. Notches (Steps) characteristics

Size	Step No.1	Step No.2	Step No.3	Step No.4	Step No.5	Step No.6
Length - L[mm]	15	15	15	15	15	15
Depth – h [mm]	2.55	2.08	1.45	1.09	0.85	0.69
Width - W[mm]	2.7	2.05	1.48	1.08	0.76	0.41

EXPERIMENT

The test penetrameter is positioned in a small water-filled tank. An ultrasound probe is then moved on a horizontal axis at a constant distance to the penetrameter (Fig. 2). The sound travels though the water and into the penetrameter. Following the sound's interaction with the exterior and interior microstructure, any flaws that may exist, or with the inner surface of the component, the echoed sound wave returns to the probe.
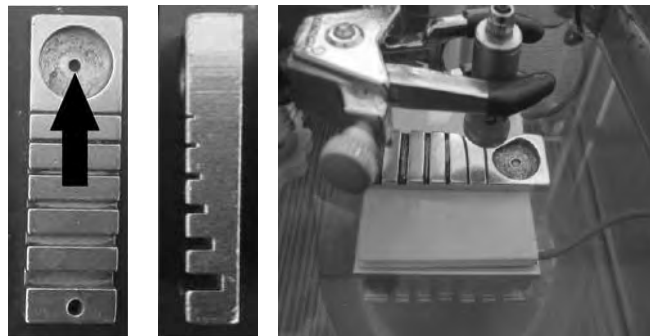
Fig. 1. Front and side view of penetramer, flat bottom holes and transducer
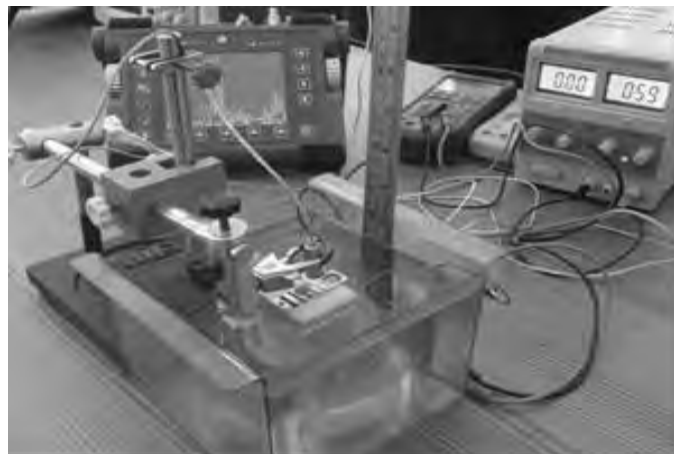

Fig. 2. Experimental set-up position

RESULTS

The image of soundwave peaks, using the immersion method, is slightly different from the contact technique. In this case there is an additional peak between the initial pulse and the back wall peaks caused by the sound wave going from the water to the test material. The arrival time of the echo and its amplitude enable interpretation of where and what it is originating from in the material. Some energy is lost when the waves hit the test material, so the front wall peak is slightly lower than the peak of the initial pulse. The rate at which an ultrasound pulse is absorbed generally depends on two factors: the material through which it passes and the frequency of the ultrasound. The attenuation rate is specified in terms of an attenuation coefficient. Its value for water is 0.002 dB/cm.

The USM 35XS ultrasonic flaw detector has been adjusted to ignore the initial pulse peak, so the first peak it will show is from the front wall of the penetrameter (from the notches side). The data obtained by the used transducers for all penetrameter steps show different signal amplitudes (Table 3). The results for attenuation of the ultrasound are presented in Fig. 3. Good sensitivity was obtained in the L5M and L15M probes. The experimental results show that the highest signal amplitudes are observed for the L15M type probe with a high frequency of 15 MHz and the lowest values are obtained when L10M (10 MHz) type transducers are applied.

Table 3. Adjusting the sensitivity in dB for different types of transducers in respect to the registered back pulse echoes from penetrameter steps

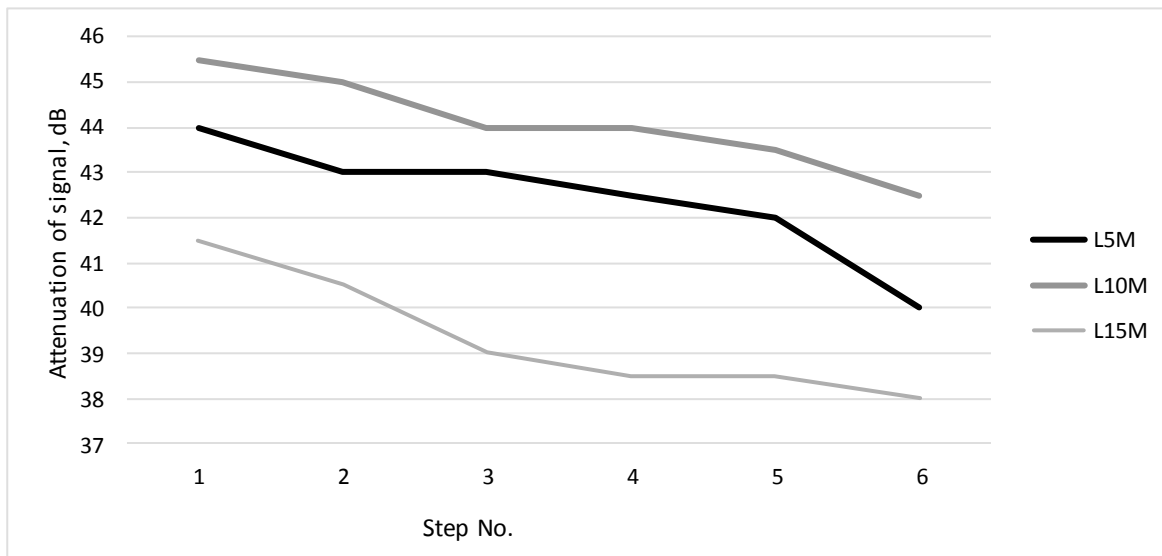| Transducer	Step No.1	Step No.2	Step No.3	Step No.4	Step No.5	Step No.6
L5M	44	43	43	42,5	42	40
L10M	45,5	45	44	44	43,5	42,5
L15M	41,5	40,5	39	38,5	38,5	38

Fig. 3. Signal attenuation for selected transducers

Measurements of the distance between applied transducers and each of the penetrameter steps have been carried out. A comparison to values obtained by a micrometer shows some differences, which are presented in Fig. 4. For the last two steps, good coincidence of the results is noticed for the L5M and L10M transducers because of their high resolution. A maximal difference of 0.93 mm is obtained when the L5M probe is applied. As it can be seen, less deviation (max 0.1mm and min -0.01mm) is observed in the L15M probe for all six steps of the penetrameter. Measurements of the distance between the applied transducers and border of the two bottom holes have been carried out.

The comparison to values obtained by a micrometer (distance-22.92 mm) shows differences which are presented in Fig. 5. As it can be seen, less deviation – 0.02 (distance – 22.94 mm) is observed in the L15M probe for the borders of flat bottom holes, because of its high resolution and sensitivity.
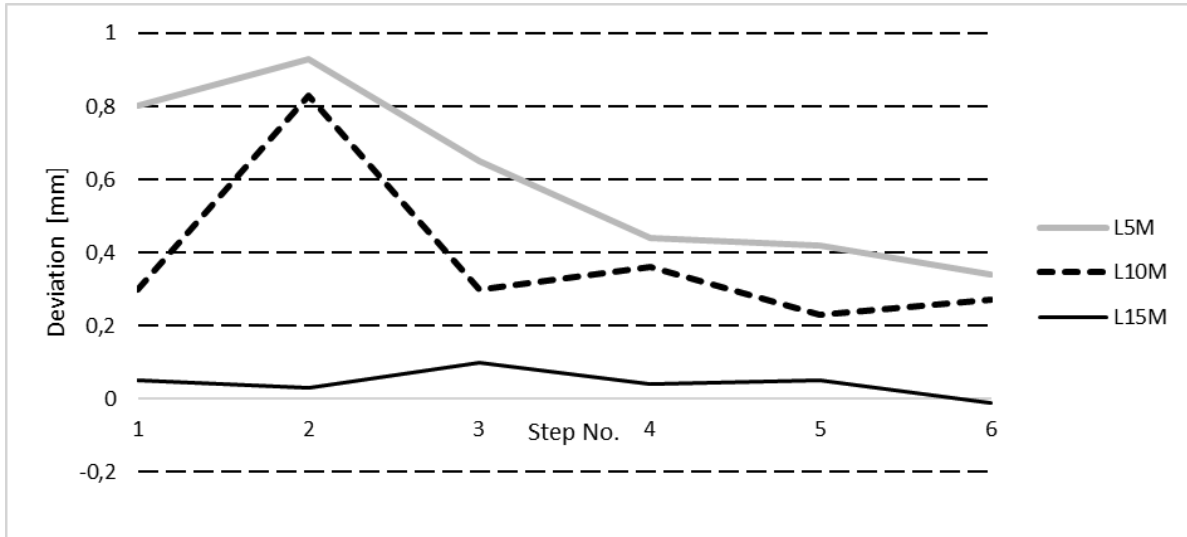

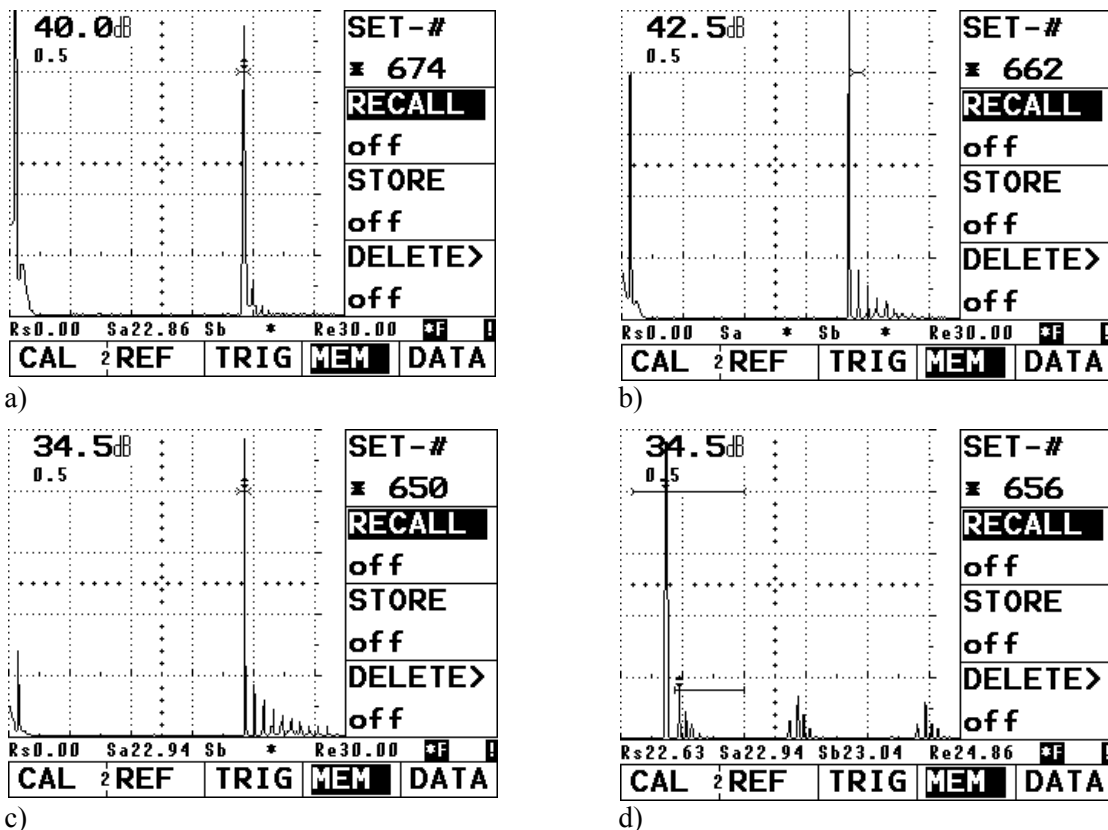**Fig. 4.** Differences between micrometric and ultrasonic measurements

Fig. 5. Echo-signal position and amplitude for transducers: a) L5M, b) L10M, c) and d) L15M

CONCLUSIONS

The results of the ultrasonic immersion investigation show that we can confidently distinguish the steps and flat-bottom holes of the calibration block in terms of their depth and width. Optimal signal is obtained at a sensitivity of 39 - 41 dB and a frequency range from 2 to 20 MHz. When using the line-focus beam transducer L5M we get a higher amplitude but a lower resolution in comparison to the broad-band transducer L15M with the same settings. The obtained data for all steps and flat bottom holes at a frequency of 15MHz unambiguously show a very good signal resolution at sufficient amplitude.

Observations during the experiment show clear enough and well-reproducible differences in the sample with the same thickness as Peltier modules, which can be a criterion for characterizing its electrical properties. The application of the high frequency ultrasonic immersion method provides a good resolution and correct selection of Peltier modules in terms of their structure and homogeneity, and can be used for quality control without compromising their integrity.

REFERENCES

1. Hübschen, G. *Ultrasonic techniques for materials characterization, In: Materials Characterization Using Nondestructive Evaluation (NDE) Methods*, pp. 177-224.
2. Ramzi, R., M. F. Mahmod and E. Bakar. *Immersion ultrasonic inspection system for small scaled composite specimen, Journal of* Engineering and Applied Sciences 10 (22), 2015, 17146-17150.
3. Kasarov, R. *Investigation of Polymeric Materials by Means of Electro Acoustic Methods,* Assen Zlatarov University Annual, Vol. XLVII, Book 1, 2018, p.97.
4. Nikolaeva, Z. and T. Mihalev, *Modeling ultraviolet radiation for Burgas Municipality,* International Scientific on-line Journal Science & Technologies, Stara Zagora, Bulgaria, IV (3), 2014, pp. 15-19.

COMPARATIVE ANALYSES OF DATA ON RADIOLOGICAL MONITORING OF VROMOS BAY AREA

Sabina Nedkova, Plamena Atanasova
E-mail: sabina_nedkova@abv.bg

ABSTRACT

The ionizing radiation environment inhabited by living organisms and created by ionizing radiation is known as radiation background. Depending on the sources of radiation, the radiation background can be natural, artificial and technologically changed. Its systematic monitoring is extremely important for the life and health of living organisms which do not have the senses to detect when it increases. In Bulgaria, monitoring of the ionizing radiation environment is carried out according to an approved scheme for conducting radiological monitoring, including points, monitored indicators and periodicity, according to directives of the Ministry of Environment and Water. For places where high values of radiation background are reported, such as Vromos Bay, radiological monitoring is constant and includes determination of the content of natural and man-made radionuclides in soil, sediment and water samples and measuring the gamma background of the environment.

Key words: ionizing radiation environment, radiological monitoring

INTRODUCTION

Vromos Bay is a small bay at the southern end of the Gulf of Burgas, located between two rocky capes: Atia to the west and Akin to the east. The area of 203,944 sq. m stretching between them is occupied by the nearly 3 km long sandy beach of Vromos. Bay of Vromos was used as a landfill for the tailings from the copper flotation plant of the nearby Rosen mine. The mine and the flotation plant were exploited for 50 years between 1945 and 1995 with a total yield of 7,563 t of ore with 1.02% copper concentration or 77,912 t of copper metal (Ivanov, 2006) In 1998, after the closure of the mine, the Vromos beach underwent recultivation financed by the EU Phare Ecology Program. The layer of sand contaminated with heavy sulfidic ore minerals as well as minerals containing radionuclides were removed and replaced with a non-contaminated layer of sand. The recultivation was targeted only at the surface area of the beach, which left the sediments in the deeper parts of the bay contaminated with heavy mineral ores containing the typical elements of the mineral paragenesis of the hydrothermal deposits of the Rosen mine, such as arsenic, copper, barium, iron etc., and, potentially, radionuclides of uranium, radium and lead [1].

EXPERIMENT

Radiometric measurements on the territory of Vromos Bay near the closed Rosen Mine are carried out by the Regional Laboratory for Radiation Measurements at the Executive Environment Agency (EEA) in Burgas. The obtained data are collected, processed and stored in a national database. The radiometric measurements are carried out four times a year and include rock samples from Vromos Bay. Along with this, the same laboratory does radiological monitoring which aims to determine the content of natural and man-made radionuclides and includes taking samples from two points: Vromos Bay beach point and Vromos Bay surf point, and sea water in the bay for determination of Cs-137 radionuclide.

This article aims to compare the results obtained from the Regional Laboratory of EEA, Burgas with those obtained from measurements made by a team of experts in the framework of a university project. The following were measured:

- gamma radiation background (gamma radiation dose rate);
- specific activity of natural and man-made radionuclides in sand samples from two control points on Vromos Bay beach, "fresh" sediment from the surf on

Vromos beach and soil from the area of waste water runoff from a tailings pond.

RESULTS AND DISCUSSION

The compared samples were taken by the team of experts at six points in the area of Vromos Bay and Rosen Mine tailings pond. Two points are located on the territory of the tailings pond of the Rosen Mine and are soils (Sample 1). Two of the points are located at the end of the sedimentary channel, which ends in the sandy strip and is covered with sediment (Sample 2) and two of the points are on the wet part of the shore (Sample 3). The samples were taken manually with a shovel, according to the following scheme: soil samples from uncultivated soil - for each point, single samples were taken from two depths (0-10 cm) and (10-40 cm) from a circle with a radius of 5 m, on a grid basis (at every 1 m), which are then mixed, homogenized and averaged. The sand samples were taken as single samples on a grid basis, manually with a spatula within a radius of 2 m (about 50 cm), then mixed well and averaged.

The specific activity of certain radionuclides in the averaged soil and sand samples was measured using gamma spectrometric analysis with an ORTEC computer multi-channel analyzer with HPGe detector GEM-15190-P type. The study was performed in the Monitoring of Population Exposure laboratory of the National Center for Radiobiology and Radiation Protection. In the areas where the sampling points fall, the power of the absorbed gamma radiation dose in the air was determined, as 5 readings of the exposure power at a height of 1 m from the earth's surface are made for each of the points, after which the values were averaged. For gamma radiation background of the environment, three different dosimetry devices, FAG, Bella and Graetz, were used [2].

The samples of soils, sand and sediment were collected by the team from the area of Vromos Bay in June 2020. It was established that:

For test sample 1 - tailings soil, the following specific activity was measured: uranium-238 (42.7 Bq / kg), radium-226 (105 Bq / kg) and Lead-210 (119 Bq / kg). The gamma background at the test point is in the range: 0.06-0.21 µSv / h.

For test sample 2 from the end of the sedimentary channel, which ends in the sandy strip and is covered with sediment, the following data of the specific activity was found out: uranium-238 (131.6 Bq / kg), radium-226 (368 Bq / kg) and lead- 210 (169 Bq / kg). The gamma background at the test point is in the range: 0.18-0.46 µSv / h.

For test sample 3 from the wet part of the coast in Vromos Bay the following data of the specific activity was found out: uranium-238 (150.3 Bq / kg), radium-226 (495 Bq / kg) and lead-210 (222 Bq / kg). The gamma background at the test point is in the range: 0.14-0.50 µSv / h.

The Regional Laboratory of EEA studied 3 samples of rock material (the Black Sea near Chernomorets and the Black Sea near Vromos) for the period April-June 2021. The analysis of the rock material sample (sand from the beach of Chernomorets), there was no excess found compared to the values typical for the region, which are: U-238 (23Bq/kg), Ra-226 (22Bq/kg), Th-232 (15Bq/kg), Pb-210 (19Bq/kg), K-40 (1534Bq/kg). The content of the deposited technogenic radionuclide cesium-137 is 2.64 Bq / kg. The measured gamma background is 0.13 µSv / h.

From the monitoring of the radiation situation in Vromos Bay it is established that the tested sample "sand" on the beach has the following specific activity: uranium-238 (423Bq / kg), radium-226 (405 Bq / kg) and lead-210 (276 Bq / kg). The gamma background at the test point is in the range: 0.25-0.27 µSv / h. The specific activity of the sample "fresh" sediment from the surf are respectively: uranium-238 (226 Bq / kg), radium-226 (223 Bq / kg) and lead-210 (194Bq / kg). The measured values of the specific activity in the samples from the two points do not differ from the previous measurements on the beach of the bay, polluted in the period 1954-1977 by deposited flotation waste with increased content of natural radionuclides from the Rosen flotation plant of Burgas copper mine and exceeding the background values of the clean beaches in the area [3].

In the second quarter of 2021, two samples of sea water from the territory of Burgas region were analyzed, namely from the Black Sea near Chernomorets and Vromos Bay. No deviations from the typical values of the analyzed indicators were found. The content of Cs-137 in the analyzed seawater samples from the Black Sea near Chernomorets and Vromos Bay is below the minimum detectable activity of the method (MDA - 0.029 Bq / l for Chernomorets), (MDA - 0,023 Bq/l for Vromos bay [4].

Comparison of the obtained results

The values obtained by the team from the study of soils, sediments and sand, taken from the area of Vromos Bay were compared with those obtained by the Burgas Regional Laboratory of the Executive Environmental Agency. The results are presented in the following figures:

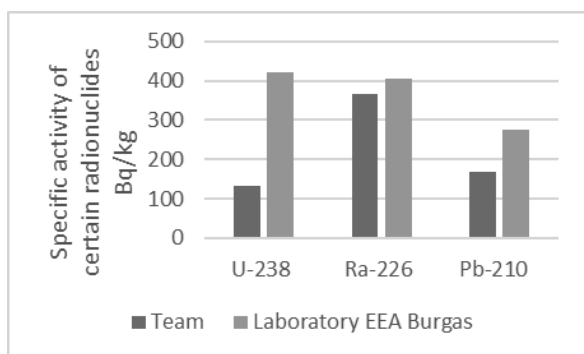**Comparison of values for a sample of sand on the beach (Fig. 1)**

Fig. 1 Sand from the beach sample

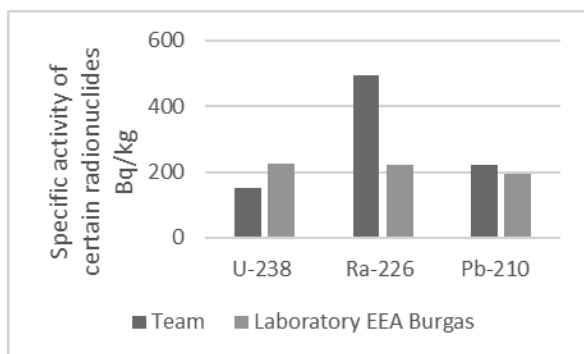**Comparison of values for sample "fresh" sediment from the surf (fig.2)**

Fig. 2 Fresh sediment from the surf on the coast-line

The obtained results show similar values for two of the three studied nuclides - for the beach sand sample, the measured values of the specific activity of uranium 238 are higher in the measurements of EEA laboratory in Burgas, and for the values of the specific activity measured in the sample of fresh sediment from the surf, the values are higher for Radium-226, as reported by the team.

These differences can be explained by the differences in the places from which the samples were taken, as well as by the different devices with which the measurement of the analyzed data was performed.

The measured gamma background at the sampling points by the Laboratory of EEA does not exceed the safe limits of 0.06-0.40 µSv / h, and in the measurement done by the team slightly exceeds these limits, in data obtained by only one of the three used of 0.50 µSv / h.

CONCLUSION

The measured values of the specific activity in the samples from both points are close to the measurements of the regional laboratory of EEA for this and previous years, for the beach of the bay, whose radiological indicators are affected by the deposited flotation waste from the Rosen flotation plant of Burgas copper mine and exceed the background values of the "clean" beaches in the area.

AKNOWLEDMENT

REFERENCES

1. Ivanov Y., Kisyov A., Tzankov Ch., Radiometric Survey of Vromos Bay, Black Sea, VIII National Conference on Geophysics, 25th November 2016
2. Atanasova P., Nedkova S., Kasarov R, Totzeva R., Totzev A, "Radiological monitoring of sand and soil from Vromos Bay" from 22nd RSEP International Economics, Finance & Business Conference, 25-26 August 2021, Istanbul, Turkey p 222-228
3. web site of the Executive environment agency, visited on 16th of October 2021 http://eea.government.bg/bg/dokladi/threemonth/threemonth.02_2021/radiatn/radsoil
4. web site of the Executive environment agency, visited on 16th of October 2021 http://eea.government.bg/bg/dokladi/threemonth threemonth.02_2021/radiatn/radwat

TESTING OF DIGITAL RELAY PROTECTION MODEL SCU OF ABB COMPANY

Mladen Proykov
E-mail: m_proykov@abv.bg

ABSTRACT

The paper presents a brief overview of digital relay protections, device, principle of operation, characteristics and basic parameters. A model for testing digital relay protection model SCU of ABB company has been prepared. For each of the relay protections realized with SCU, laboratory tests were performed with a professional loading device produced by Metrawatt. The tripping currents of the protections and the tripping times are recorded and the relative errors are calculated. A comparison of the performance of the SCU with that of the conventional protections is made.

Key words: *relay protection; ground protection; current relay; overcurrent protection*

INTRODUCTION

Digital relay protection (DRP) based on transistors, operational amplifiers and integrated circuits has better qualities than electromechanical ones, despite the slower pace of development and correspondingly lower mass use in the first years.

The characteristic features of digital protections, which are widely imposed in recent years and which surpass conventional relay protections, are the following: [5,7,14]

1. Analog variables are converted to digital and calculated by a processor.

• The protections have programs for each of their functions.

• Several protection functions can be combined and performed by a single unit: relay protection, control, emergency automation, regulation, event logging and measuring the distance to the fault location, etc.

2. Each block of DRP has built-in permanent programs for self-monitoring and diagnostics of hardware and software.

3. The protection can be controlled by the PC via programs with menus in different languages.

4. The digital inputs have connections to external signals via optical cables.

5. Event records are analysed over time based on the accumulated data.

• Basic hardware can be created, different functions can be set and relay protections with different properties can be realized;

• Adjustment and verification under operating conditions can be performed with computerized test equipment. The effect that is obtained is multifaceted: improving accuracy; test automation; tests can be performed in transient mode, in the presence of higher harmonics (h.h.) and subharmonics, when giving signals from actually registered currents and voltages of short circuits.

6. Digital relay protections put less strain on electromechanical measuring transformers and enable the use of linear converters (current transformers, Rogowski belts and voltage dividers).

7. They have lower consumption of the operating circuits and minimum requirements for the quality of the operational power supply (DC or AC voltage).

8. The relays are equipped with LED indicators. They can store relay status, even in the event of a DC operating voltage failure.

Even with the creation of the first electronic protections, special attention is paid to the impact of the environment in which the relays must operate. External interference is eliminated by separating the circuits with inductive and optical connections, as well as by appropriate filtering and coding of the signals. All microprocessor-based relays must meet IEC requirements for insulation tests, electromagnetic compatibility test for protection against interference, electromagnetic compatibility for interference emissions, mechanical stress tests and climate load test. [10]

Microprocessor-based relays can be programmed to continuously monitor several of their hardware and software subsystems, thus detecting possible faults. With the self-test property, relay failures can be detected quickly and

repaired before they are able to interfere with operation. This process minimizes repair time and the need to monitor protections during operation.

DRP have a system interface for connection to a computer, through which to communicate using special software. They have a coordinated speed for data exchange and formats for recording in the central information system of the respective substation [1,13,15].

THEORETICAL RESEARCH

Relay protections are used to turn off the circuit breaker instantly, with a set time delay (in case of overload or in case of earth fault current). They are characterized by low consumption of active power and high return coefficient with high accuracy of time measurement and high stability of hp. They are especially suitable for protection of generators, transformers and power lines.

The system with an intelligent communication module offers the combination of functional control, signalling, measurement, control and monitoring. This module is an intelligent remote switch with continuous self-monitoring and the ability to connect to the control systems (PYRAMID, SCADA, etc.) of the substations [8].

SCU is a multifunctional microprocessor device. The four microprocessors of the SCU communicate with each other and self-control. They provide: automation, flexibility, protection, diagnostics, control and communication. The concept of the intelligent switching module is for continuous monitoring of the measured values.
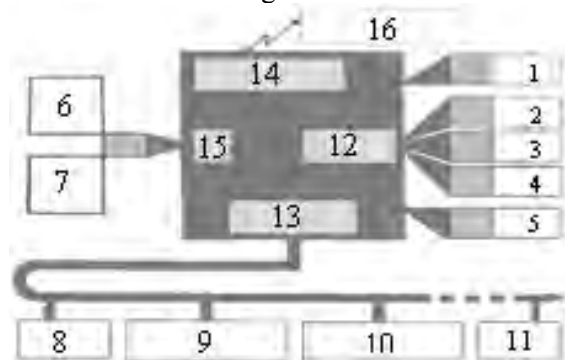

Fig. 1 Block scheme of SCU relay protection
1-auxiliari supply; 2-binary outputs; 3-power outputs; 4- signalling outputs; 5-watch-dog; 6-rogowski coil; 7-ct and tv interface; 8-termal sensor; 9-binary inputs/outputs; 10,11-various sensors; 12-controller; 13,14-processors; 15-DSP; 16-scada system.

SCU remote control and protection is based on a microprocessor system capable of real-time operation. The main microprocessor responsible for control and signalling is assisted by a digital signal microprocessor /DSP/, which performs all protection functions and calculations of R.M.S. (current and voltage measurements).

SCU has the following interfaces:
- optically separated binary inputs;
- output auxiliary relays for actuation of switching devices;
- alarm output relays;
- analog inputs - current and voltage sensors;
- LON - bus for receiving data from external sensors /temperature sensors/;
- communication bus /connected to the control system of the substation/.

With specialized software, SCU can be oriented exactly to the needs of remote switching. The SCU can be connected to a computer via a standard RS232 serial port. SCU provides a wide range of features that protect all types of working equipment. These functions can be combined. The combinations are limited only by the calculation time from the DSP. Each of the following functions can be turned off or left to signal only.

Depending on the SCU configuration, the following values can be measured and visualized, as shown in Table 1 [4].

Table 1. Parameters of the SCU relay protection

$-$zero sequence current: I_0	$-$active power: P
$-$phase voltage: U_1, U_2, U_3	$-$reactive power: Q
$-$frequency: f	$-$reactive energy: W_R
$-$power factor: $\cos\varphi$	$-$active energy: W_A
$-$linear voltage: U_{12}, U_{23}, U_{31}	$-$phase currents $-$ I_1, I_2, I_3

The nominal parameters of the digital relay protection are presented in the table 2. [4]

Table 2. Parameters of the SCU relay protection

Operating voltage	$(48 \div 265)$VDC
Rated current	1,2 mA
Electrical insulation	2kV
Power consumption	< 20W
Setting the time delay	$(0 \div 6)$ s
Insulation resistance	$1.10^9 \ \square$
Maximum pulse duration for commutation	4,23ms
Maximum switched current of the relays during commutation	2A
Maximum allowable current of the switching relays	20A
Working temperature	$(-10 ... +55)$ºC

The SCU is not only a control device for complete switching devices, but also provides many protection functions. Each protection function requires a certain processing time. Based on the time required to calculate the protection algorithm, a weight value for the protection function is determined. The sum of all weight values of the protection functions is processed in the SCU and must not exceed 100% of the load on the DSP processor. The following list (Table 3) shows the security functions that can be performed in the SCU [4]:

Table 3. SCU protection functions

- Overcurrent protection (3 stage)	- Directional current section (2 stage)
- Maximum voltage protection (3 stage)	- Minimum voltage protection (3 stage)
- Non-directional ground protection (2 stage)	- Directional ground protection (2 stage)
- Temperature overload	- Temperature control
- Low load	- Frequency control
- Asymmetric load	Synchronization
- Motor protection	- Blocking at starting currents
- IDMT – Overcurrent protection (time dependent) with normal delay	
- IDMT – Overcurrent protection with a large, very large or prolonged delay	

The operation of the protection functions performed in the SCU is based on the comparison of two limit values (measured and calculated against the pre-established limit value). The duration of the period for which the measured and calculated limit values exceed the programmed limit value with a pre-set time is also monitored. As soon as the measured or calculated value exceeds the programmed limit value, the corresponding protection in the SCU is activated and the timer starts at the same time. If, after the programmed time has elapsed, the value is still above the programmed limit, the protection function switches off the corresponding circuit breaker and thus prevents conductions in the power system. The SCU works mainly with the effective value of the measured current and voltage signals.

Software activated security functions in the tested SCU are:

- current section (CS) - detects single-phase and three-phase short circuits. Maximum current value: $I >>> / I_{NOM} = (0.1 \div 40)$ and time for maximum current: $t = (0.02 \div 30)$s (standard 0.5s). A three-stage current section with two established parameters is provided (SET 1: $3.I_{NOM}$ / 0.02s) and SET 2: $8.I_{NOM}$ / 0.002s);

- overcurrent protection (OCP) - for single-phase, two-phase and three-phase short circuits. Both stages can be programmed with set parameters: SET 1 and SET 2. Establishing a high value: Maximum current: $I >> / In = (0.05 \div 40)$ (standard 0.2) and time for maximum current $t = (0.02 \div 300)$s (standard 0.3s). Establishing a low value: Maximum current: $I > / In = (0.05 \div 25)$ (standard 0.05) and time for maximum current $t = (0.02 \div 300)$s (standard 1s). The current SCU is provided at a high value SET 1 ($1.I_{NOM}$ / 0.45s) and SET 2 ($1.I_{NOM}$ / 0.45s) and at a high low: SET 1 ($1.I_{NOM}$ / 0.4s) and SET 2 ($1.I_{NOM}$ / 0.4s);

- ground protection (GP) – it is possible for earth short circuits in earthed and ungrounded networks. The non-directional GP function has two stages with the establishment of two parameters for each stage (SET 1 and SET 2). Establishing a high value: Current value at earth short circuit: $I_{NOM} = (0.05 \div 40)$A (standard 0.1A) and time for shutdown: $t = (0.05 \div 100)$s (standard 0.3s). Establishing a low value: Established parameters: SET 1 and SET 2. Current value at earth short circuit: $I_{NOM} = (0.05 \div 40)$A (standard 0.1) and time for shutdown: $t = (0.05 \div 100)$s (standard 0.3s); The parameters entered in the current SCU for non-directional GP are: Establishing a high value: SET 1 ($0.4.I_{NOM}$ / 0.1s) and SET 2 ($0.4.I_{NOM}$ / 0.1s). Establishing a low value: SET 1 ($0.4.I_{NOM}$ / 0.03s) and SET 2 ($0.4.I_{NOM}$ / 0.05s);

- overcurrent protection with a hyperbolic characteristic (IMDT) - function with different time dependent protections, with hyperbolic $I = f(t)$ characteristics. The established parameters (SET 1 and SET 2), can be in the following ranges: Maximum current value: $I > / I_{NOM} = (0.05 \div 40)$ (standard 0.05) and time factor: $\kappa = (0.05 \div 1)$ (standard 0.05).

SCU has 7 analog inputs for receiving current and voltage signals. They are divided into 3 groups of 2 triple and 1 single input. Each group can measure current or voltage. This means 6 phases for voltage measurements that are possible, such as 3 phases for current measurements with 4 voltage inputs (for synchronization and maximum current function on a sectional panel). The most common combinations are 1 + 3 current, 3 voltage and one grounding input. Using this combination, the SCU shows the following values on its display:

- direct measurements: currents (three phases); earth short circuit current; phase voltage (three phases) and frequency;
- calculates: linear voltage (three phases), medium / maximum current (three phases), active and reactive power (energy) and cosφ;

PRACTICAL RESEARCH

On the basis of the prepared experimental setup, practical studies have been carried out to establish the actual tripping currents of the SCU protection depending on the set tripping currents, as well as to determine the actual tripping times of the protection depending on the set ones. Fig. 2 shows the block diagram of the model when testing the protection functions: overcurrent protection (OCP), current section (CS) and ground protection (GP) [2,6,9].
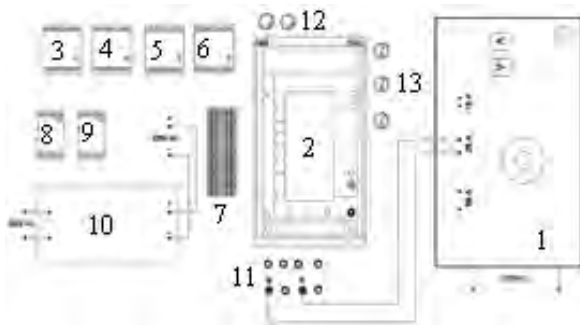
Fig. 2 Block scheme of the model 1-loading device; 2-DSP; 3÷6-auxiliary relays; 7-terminal block 8,9-auxiliary relays; 10-DSP power supply;11-current/voltage terminals; 12,13-light alarms.

Fig. 3 shows a general view of the model.

Fig. 3 General view of the model

The measurements are made with a professional digital, loading device GOSSEN METRAWATT in a licensed measuring laboratory. The measurements are presented in tabular form (Tables 4, 5, 6). Relative error ε is calculated:

$$\varepsilon = \frac{I_{ON} - I_{NOM}}{I_{NOM}} , \ \% \tag{1}$$

Table 4. Overcurrent protection

SCU – function OCP (phase R)	t_{NOM}	t_{ON}	I_{ON}	ε
	s	s	A	%
$I_{NOM} = 1.I = 5A$	0.4	0.41	4.85	3.09
$I_{NOM} = 2.I = 10A$	0.4	0.42	9.9	1.01
$I_{NOM} = 3.I = 15A$	0.4	0.43	14.95	0.33
$I_{NOM} = 4.I = 20A$	0.4	0.44	20.05	0.25

Table 5. Current section

SCU – function CS (phase R)	t_{NOM}	t_{ON}	I_{ON}	ε
	A	A	-	%
$I_{NOM} = 1.I = 5A$	0.02	0.024	4.75	5.26
$I_{NOM} = 2.I = 10A$	0.02	0.023	9.77	2.35
$I_{NOM} = 3.I = 15A$	0.02	0.022	14.79	1.42
$I_{NOM} = 4.I = 20A$	0.02	0.021	19.81	0.96

Table 6. Ground protection

SCU – function GP (phase R)	t_{NOM}	t_{ON}	I_{ON}	ε
	s	s	A	%
$I_{NOM} = 0.2.I = 1A$	0.08	0.085	0.95	5.26
$I_{NOM} = 0.4.I = 2A$	0.08	0.084	1.96	2.04
$I_{NOM} = 0.6.I = 3A$	0.08	0.083	2.97	1.35
$I_{NOM} = 0.8.I = 4A$	0.08	0.082	3.98	0.51
$I_{NOM} = 1.I = 5A$	0.08	0.081	5.02	0.39

Based on the obtained results, the following graphical dependences are constructed: $\varepsilon = f (I_{ON})$; $I_{ON} = f (I_{NOM})$; $t_{ON} = f (I_{ON})$.
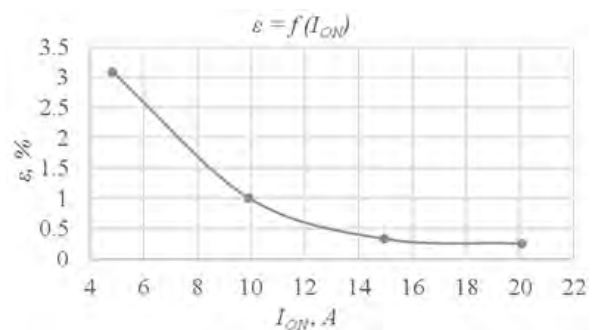
Function: Overcurrent Protection
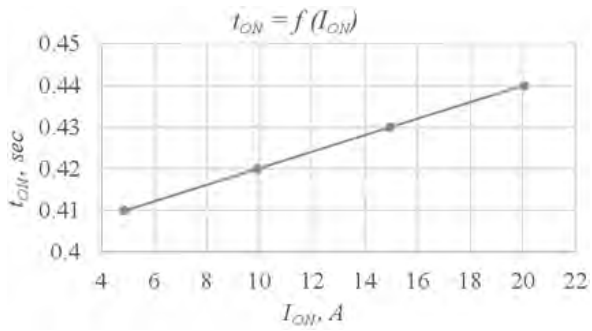

Fig. 4 Dependence between $\varepsilon = f (I_{ON})$
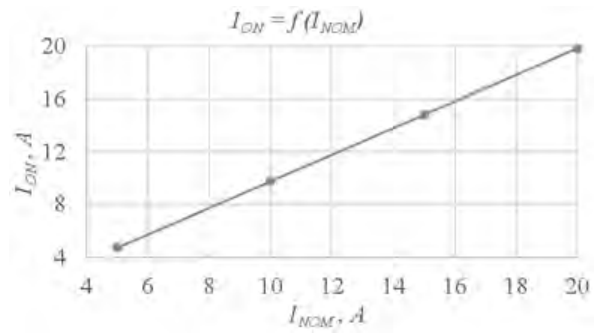
Fig. 5 Dependence between $t_{ON} = f(I_{ON})$
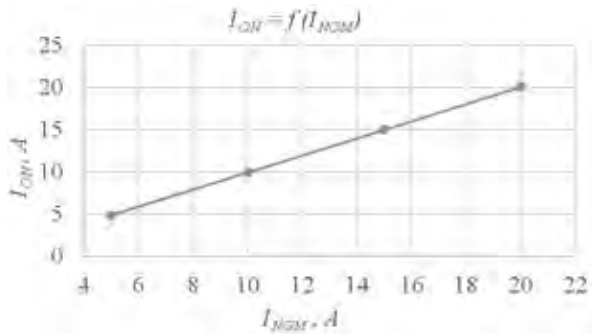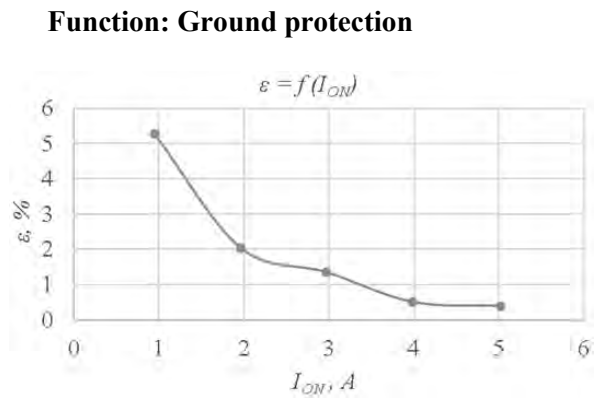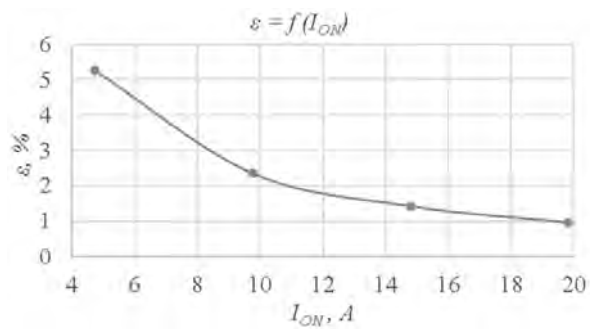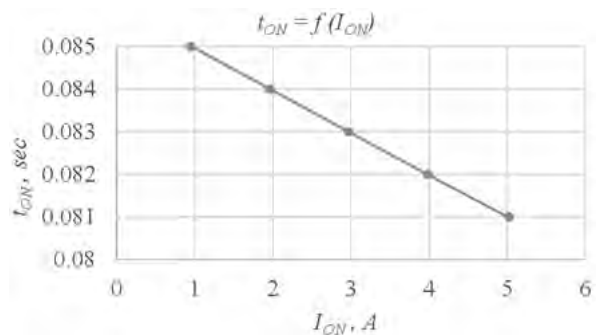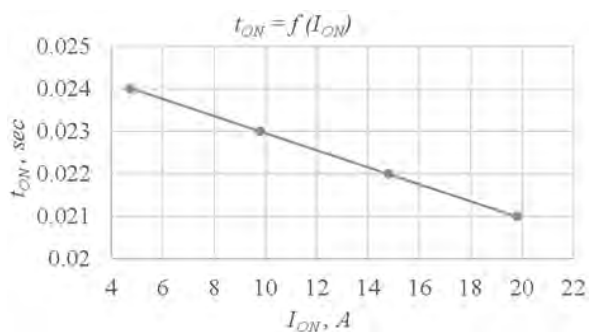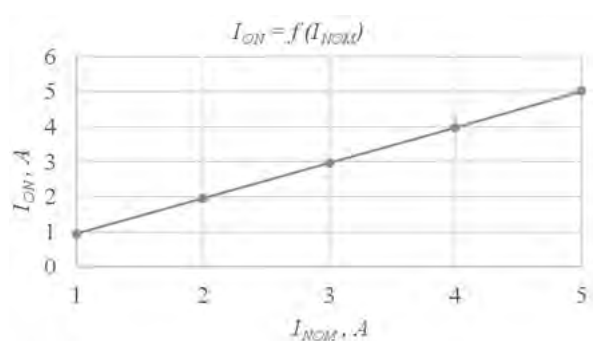

Fig. 9 Dependence between $I_{ON} = f(I_{NOM})$

Function: Ground protection

Fig. 6 Dependence between $I_{ON} = f(I_{NOM})$

Fig. 10 Dependence between $\varepsilon = f(I_{ON})$

Function: Current section

Fig. 7 Dependence between $\varepsilon = f(I_{ON})$

Fig. 11 Dependence between $t_{ON} = f(I_{ON})$

Fig. 8 Dependence between $t_{ON} = f(I_{ON})$

Fig. 12 Dependence between $I_{ON} = f(I_{NOM})$

69

RESULTS AND DISCUSSION

ABB digital relay protection SCU has been studied, with functions of: overcurrent protection, current section and ground protection. It can be used in most automated control and protection systems of circuit breakers (20 ÷ 110)kV. It is compatible with many modules, protections and systems of other manufacturers. Based on the research, the following conclusions were made:

1. The operating parameters I_{ON} и t_{ON}, are compared with the factory parameters and the calculated relative errors ε are compared with the regulatory requirements in the Standard. Studies have shown that as the I_{ON} current increases, the relative error ε when the protection trips is reduced and ranges up to 5%. The requirement of the standard is that the accuracy of relay protection is within 5%, i.e. it meets the regulatory requirements [3,9]:

2. From the performed research of the digital relay protection SCU of the company ABB and research of electromechanical relay protections models: AT31 (OCP), A22 (CS) and RI - 3 (GP) it follows that [11,12]:

- The complexity of the implementation of electromechanical relay protections is significantly greater than that of the implementation of digital ones (wiring, interlocks, hardware, settings, etc.);
- The reliability of the electromechanical relay protections is significantly lower than that of the digital ones, due to the large number of elements involved in the realization of the first ones (measuring relays, timers, auxiliary relays, etc.).
- The relative error ε in electromechanical relay protections reaches 8% and in digital is up to 5%. For the relay protections the relative error needs to be lower than 5% [11,12].

REFERENCES

1. Andreev A., *Relay protection and automation in power systems*, Moscow, 2006.
2. Andreev S., Mehmed-Hamza M., *Guide for laboratory exercises in relay protection,* Varna, 2003.
3. EN 60255-1 (IEC 60255-1) - Measuring relays and protection equipment. Part 1.
4. *Handbook. ABB protection and control device*, ABB GmbH, 2010.
5. Ivanov K., P. Uzunov, *Electrical part of power stations and substations,* 2008.
6. *Manual for laboratory exercises,* Almamater International, Gabrovo, 2001.
7. Mehmed-Hamza M., *Relay protection and automation of electrical energy systems*, Varna, 2019.
8. *Network Protection and Automation Guide*, AREVA, 2005.
9. Ordinance №3 / 09.06.2004, *Structure of electrical installations and power lines*, SG. no. 90 and 91/2004.
10. Penchev S., *Control and measurement in power supply systems. Notes.* Gabrovo.2011.
11. Stamatov D., *Investigation of relay protections for power lines M.V.,* Diplom work, Burgas, 2020.
12. Stefanov N., *Current protections for power lines, Laboratory device*, Diplom work, Burgas, 2017.
13. Vichev S., *Design and operation of relay protections. Notes*, Sofia, 2008.
14. Vichev S., *Relay protection*, Sofia, 2008.
15. Vichev S., *Digital relay protections. Notes*, Sofia, 2008.

TESTING OF SYSTEM FOR SMOOTH STARTING OF ASYNCHRONOUS MOTOR

Mladen Proykov, Vasil Ivanov
E-mail: m_proykov@abv.bg

ABSTRACT

One of the issues related to the proper control of the electric drives of various units is the starting and stopping of motors, due to the unwanted electrical and mechanical transients that occur in the electric drive systems. To avoid these processes, soft starters are most often used to ensure smooth start and stop of asynchronous motors. Under the general name of soft starters, there are many technical solutions that differ from each other in their capabilities, connection schemes, the need for additional devices and the principle of operation. This article aims to examine the operation of the SIRIUS 3RW30 13 soft starter, standard applications of Siemens.

Key words: *electric drive, soft starter, transients, asynchronous motor, smooth starting*

INTRODUCTION

When starting high-power electric drives directly, significant voltage drops are observed and the quality of the electric energy deteriorates. In machines with medium and low power, the direct start can lead to damage to various mechanical devices of the system as a result of a sharp jump in motor torque. Direct starting is not good for the motors, as it reduces their service life. The high starting current creates a lot of problems such as increase of the temperature of the electrical equipment and fluctuation δU. The permissible value of δU for LV networks is ±10% of the nominal voltage [1,2].

Mechanical transients in many cases create bigger problems than electrical ones. In asynchronous motors with cage rotor (AM-cr) it is difficult to match the starting torque of the motor with that of the load. In the first case, the starting torque of the motor may be lower than the resistance torque of the working mechanism and the AM-cr may not be able to start. In the second case, the starting torque of the motor can be much higher than the resistance torque of the mechanism at low speeds. In this case, mechanical shocks occur during start-up, which reduces the life and reliability of the units [3,4].

Soft starters (thyristor voltage regulators) are used to reduce the influence of current on the network and the mechanical parts of the systems. Their principle of operation is to limit the voltage applied to the motor (during the starting process), using triacs. It is regulated by changing the unlocking angle of the triacs. The choice of the characteristics at which to start the motor is made by changing the unlocking angle of the thyristors α = (0 ÷ 120)°. The power supply options are: one-, two- and three-phase, the most functional being the three-phase regulation [6]. It is usually sufficient to reduce the starting current (Fig. 1) to 250% of the nominal current (for direct start it is (500 ÷ 800)% of the nominal current). In this way a gradual increase of the starting current and torque of the AM is obtained. After accelerating the AM to the desired speed, the triacs are bypassed and the machine goes into normal operation [7].
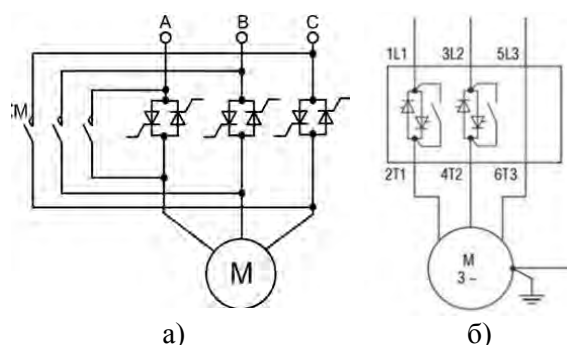

а)   б)

Fig. 1 Soft starter with three-phase (a) and two-phase (b) voltage control.

In addition to offering smooth start-up for almost any application, from simple to advanced drive requirements, such as heavy-duty start, soft starters also have many intelligent features, such as: start, stop, automatic parameterization and status monitoring, communication, compact

design, built-in motor overload protection, etc. Thanks to its maximum functionality, the intelligent soft starter masters the difficult processes of starting and stopping. Fig. 2 shows the starting characteristics of AM-cr at different ways of starting.
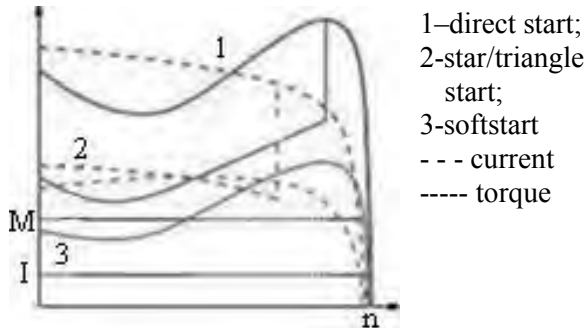

1–direct start;
2-star/triangle start;
3-softstart
- - - current
----- torque

Fig. 2 Start characteristics of AM-cr.

PRACTICAL RESEARCH

The main elements of the study are three: phase AM-cr (Table 1) and SIRIUS 3RW30 13 softs tarter from Siemens AG (Table 2).

Table 1. Nominal data of AM-cr

Nominal voltage	220/380V (D / Y)
Nominal power	0.7kW
Nominal speed	2800min^{-1}
Nominal current	1.64/0.95A (D / Y)
cosφ	0.83
Efficiency	93%
Starting characteristic	Class 10

Table 2. Nominal data of softstarter

Nominal current	3.6A
Nominal voltage	(220 ÷ 480)V, 50/60Hz
Nominal power	1.5kW
Start / stop voltage	$U_S = (40 ÷ 100)\% . U_H$
Control voltage	(110 ÷ 230)V
Start / stop time	$t_R = (0 ÷ 20)$ sec
Auxiliary contact	yes
Thyristor control	2 phase

The SIRIUS 3RW30 soft starters regulate the AM-cr voltage by changing the phase voltage, gradually increasing it in a ramp mode - from a selectable initial voltage to a mains voltage [5]. Smooth start-up reduces the stress on the equipment and leads to its slower wear and therefore to a longer period of operation. The selectable initial voltage value means that the soft starters can be adjusted individually according to the requirements of the specific application.

This two-phase soft starter (Fig. 3) operates in a control method called "polarity balancing". This method prevents the appearance of a DC current component in AC systems controlled by two-phase control soft starters. The current is the result of overlapping currents in the two controlled phases flowing in an uncontrolled phase. This results in asymmetry of the three phase currents during motor start-up and may generate noise in motors at starting voltages below 50%.U_N. The control method used with these soft starters eliminates those DC components that occur during an increase in starting voltage and prevents the occurrence of braking torque.
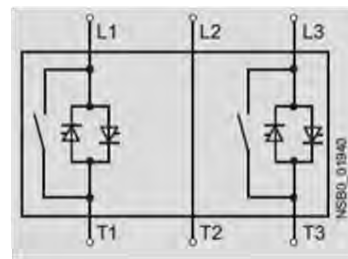

Fig. 3 Thyristor block of the Sirius soft starter

It generates motor starting unified in speed, torque and current increase, thus allowing smooth, two-phase starting of AM. With two-phase control and continuous voltage regulation, the starting current is maintained with minimum values in the three phases throughout the starting time, with no current and torque peaks. The SIRIUS 3RW30 soft starters are suitable for smooth starting of three-phase AM-cr, class 10.

Fig. 4 shows the change of the voltage U_S and time t_R, at different settings of the starting ramp. Fig. 5 shows a photo of the model.
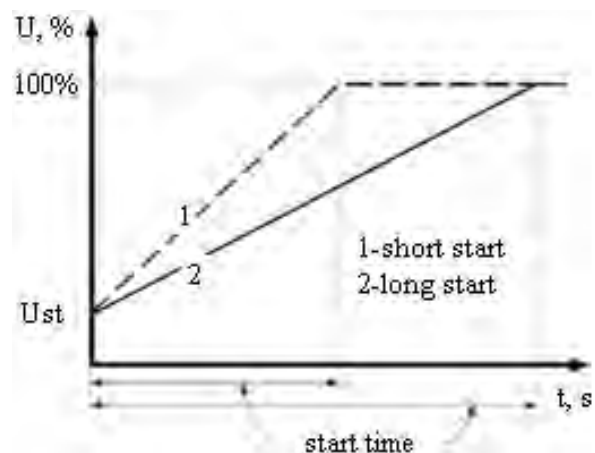

1-short start
2-long start

Fig. 4 Diagrams of U_S voltage and time t_R, at different settings of the AM-cr start-up ramp

The starting characteristics of the AM-cr with different starting schemes and different mode settings are recorded with a Fluke multifunctional measuring device, model Power Log 430 - II, Power Quality and Motor Analyzer.

Fig. 5 General view of the model

The obtained data are visualized and processed with Power Log 430 – II software. They show the change of the parameters u(t), i(t) and cosφ(t) during the transient modes.

Soft start of AM with cage rotor:

Table 3. Relation $I_M = f(n)$, $M_M = f(n)$, $U_S = 50\%.U$, $t_R = 20s$

№	I_M A	M_M N.m	n min⁻¹	№	I_M A	M_M N.m	n min⁻¹
1	1.92	2.06	0	7	2.54	3.69	1994
2	2.32	1.89	551	8	2.37	3.86	2249
3	2.43	1.81	827	9	2	3.6	2545
4	2.54	2.14	1103	10	1.41	3.8	2694
5	2.58	2.66	1379	11	0.848	2.91	2800
6	2.6	3.17	1697	12	0	0	2840

Table 4. Relation $I_M = f(n)$, $M_M = f(n)$, $U_S = 60\%.U$, $t_R = 20s$

№	I_M A	M_M N.m	n min⁻¹	№	I_M A	M_M N.m	n min⁻¹
1	2.31	2.47	0	7	3.05	4.43	1994
2	2.78	2.27	551	8	2.84	4.63	2249
3	2.92	2.17	827	9	2.4	4.5	2545
4	3.05	2.57	1103	10	1.69	4.12	2694
5	3.09	3.19	1379	11	0.85	3.49	2800
6	3.12	3.81	1697	12	0	0	2840

Table 5. Relation $I_M = f(n)$, $M_M = f(n)$, $U_S = 70\%.U$, $t_R = 20s$

№	I_M A	M_M N.m	n min⁻¹	№	I_M A	M_M N.m	n min⁻¹
1	2.69	2.88	0	7	3.56	5.17	1994
2	3.24	2.65	551	8	3.31	5.41	2249
3	3.41	2.53	827	9	2.8	5.3	2545
4	3.56	2.99	1103	10	1.97	4.81	2694
5	3.61	3.72	1379	11	0.848	4.07	2800
6	3.64	4.44	1697	12	0	0	2840

Table 6. Relation $I_M = f(n)$, $M_M = f(n)$, $U_S = 80\%.U$, $t_R = 20s$

№	I_M A	M_M N.m	n min⁻¹	№	I_M A	M_M N.m	n min⁻¹
1	3.07	3.29	0	7	4.07	5.91	1994
2	3.71	3.03	551	8	3.78	6.18	2249
3	3.89	2.89	827	9	3.2	6	2545
4	4.07	3.42	1103	10	2.25	5.49	2694
5	4.13	4.25	1379	11	0.848	4.65	2800
6	4.16	5.07	1697	12	0	0	2840

Table 7. Relation $I_M = f(n)$, $M_M = f(n)$, $U_S = 90\%.U$, $t_R = 20s$

№	I_M A	M_M N.m	n min⁻¹	№	I_M A	M_M N.m	n min⁻¹
1	3.45	3.71	0	7	4.58	6.65	1994
2	4.17	3.41	551	8	4.25	6.95	2249
3	4.38	3.25	827	9	3.6	6.75	2545
4	4.58	3.85	1103	10	2.53	6.18	2694
5	4.65	4.78	1379	11	0.848	5.23	2800
6	4.68	5.71	1697	12	0	0	2840

Table 8. Relation $M_M = f(n)$, $U_S = 50\%.U$, $t_R = 3s$

№	M_M N.m	n min⁻¹	№	M_M N.m	n min⁻¹
1	2.06	0	9	7.65	2240
2	2.94	388	10	7.33	2498
3	2.48	711	11	6.36	2628
4	3.23	1055	12	4.96	2740
5	4.09	1314	13	2.91	2800
6	4.96	1529	14	1.62	2822
7	5.93	1766	15	0.54	2832
8	6.9	1982	16	0	2840

Table 9. Relation $M_M = f(n)$, U_S=50%.U, t_R= 10s

№	M_M N.m	n min⁻¹	№	M_M N.m	n min⁻¹
1	2.06	0	9	3.91	2240
2	2	388	10	4.13	2498
3	2.05	711	11	3.91	2628
4	2.15	1055	12	3.48	2740
5	2.27	1314	13	2.91	2800
6	2.51	1529	14	1.62	2822
7	2.83	1766	15	0.54	2832
8	3.26	1982	16	0	2840

Direct start of AM with cage rotor:

Table 10. Relation $M_M = f(n)$; $I_M = f(n)$

№	I_M A	M_M N.m	n min⁻¹	№	I_M A	M_M N.m	n min⁻¹
1	5.37	6.21	0	9	4.92	7.53	2173
2	5.31	5.71	250	10	4.75	7.78	2361
3	5.26	5.3	480	11	4.52	7.45	2570
4	5.21	5.22	690	12	4.24	4.97	2696
5	5.18	5.38	940	13	3.99	3.73	2737
6	5.13	5.55	1212	14	1.25	3.38	2758
7	5.09	6.29	1546	15	0.85	2.4	2800
8	4.99	7.2	1943	16	0	0	2840

Soft start of AM with cage rotor:
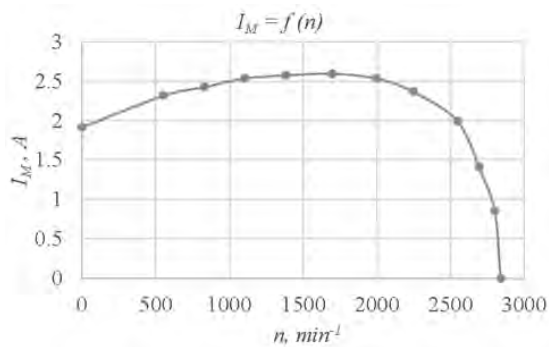
Fig. 6 Graphic $I_M = f(n)$, U_S = 50%.U, t_R = 20s
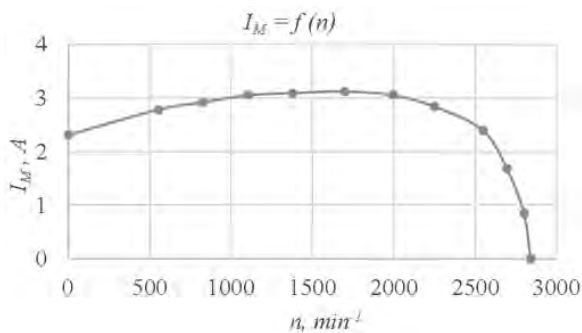
Fig. 7 Graphic $I_M = f(n)$, U_S = 60%.U, t_R = 20s
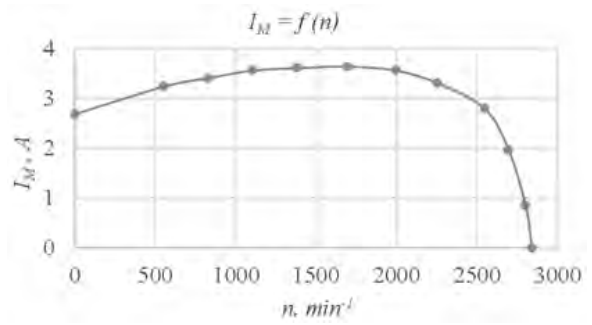
Fig. 8 Graphic $I_M = f(n)$, U_S = 70%.U, t_R = 20s
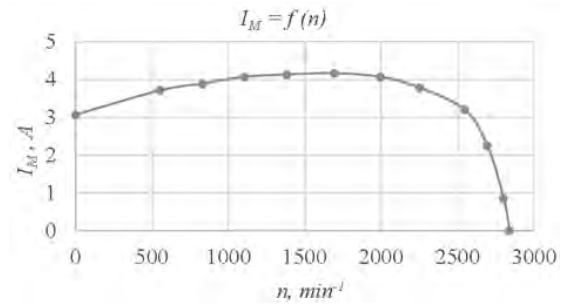
Fig. 9 Graphic $I_M = f(n)$, U_S = 80%.U, t_R = 20s
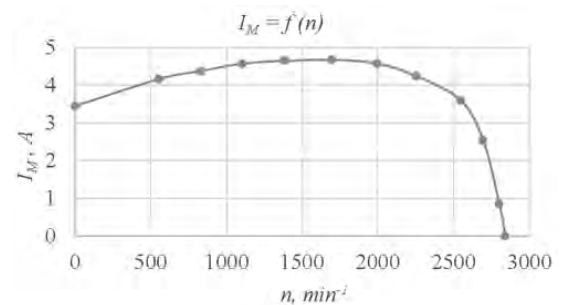
Fig. 10 Graphic $I_M = f(n)$, U_S = 90%.U, t_R = 20s
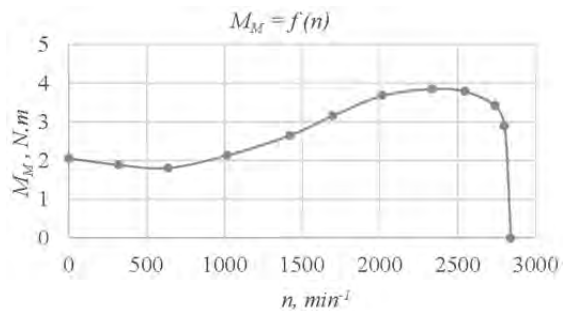
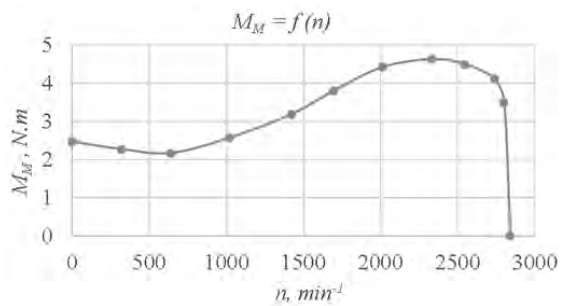**Fig. 11** Graphic $M_M = f(n)$, U_S = 50%.U, t_R = 20s

Fig. 12 Graphic $M_M = f(n)$, U_S = 60%.U, t_R= 20s

Fig. 13 Graphic $M_M = f(n)$, $U_S = 70\%.U$, $t_R = 20s$

Fig. 14 Graphic $M_M = f(n)$, $U_S = 80\%.U$, $t_R = 20s$

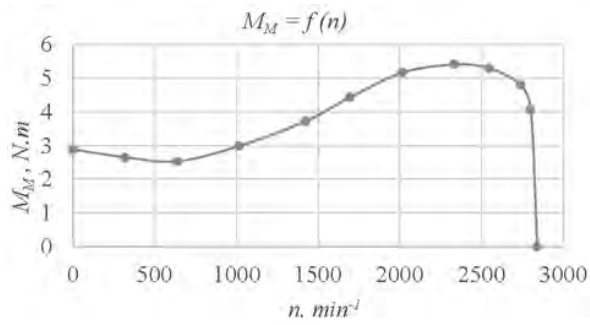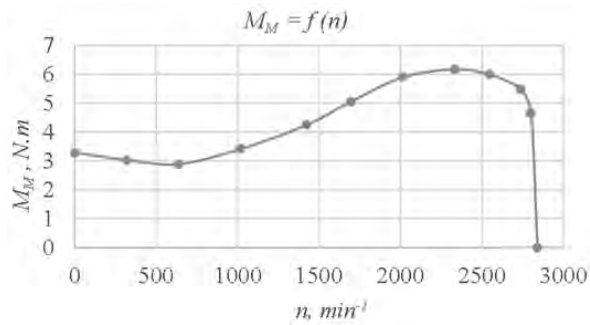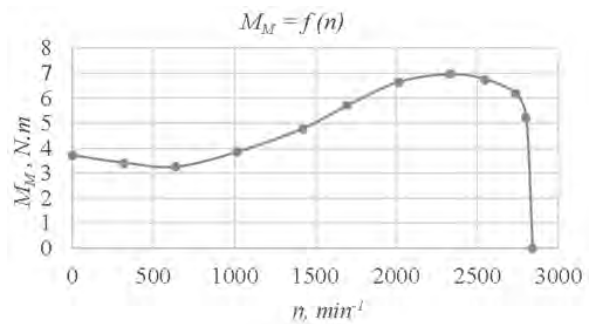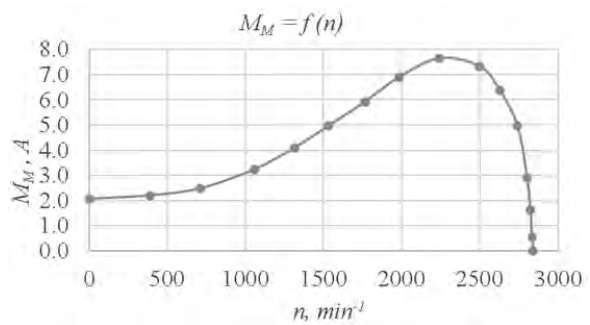**Fig. 15** Graphic $M_M = f(n)$, $U_S = 90\%.U$, $t_R = 20s$

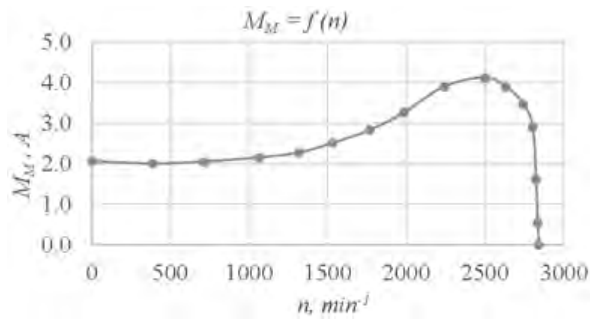**Fig. 16** Graphic $M_M = f(n)$, $U_S = 50\%.U$; $t_R = 3s$

Fig. 17 Graphic $M_M = f(n)$, $U_S = 50\%.U$; $t_R = 10s$
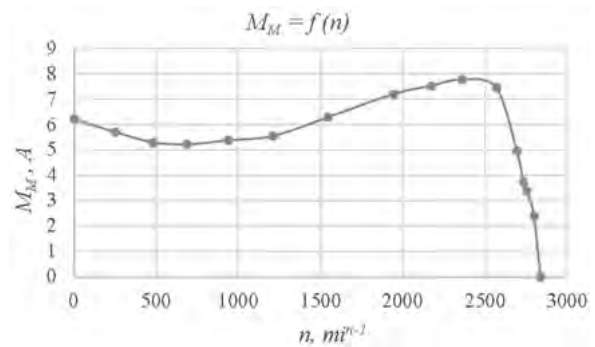
Direct start of AM with cage rotor:
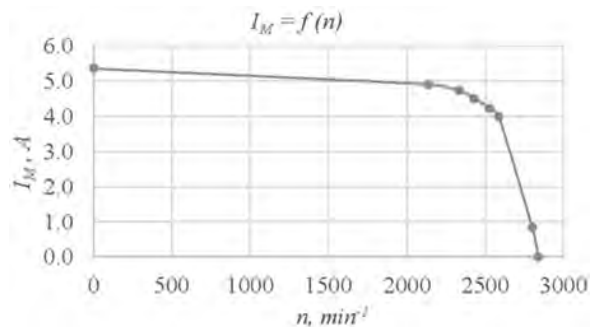

Fig. 18 Graphic $M_M = f(n)$

Fig. 19 Graphic $I_M = f(n)$

RESULTS AND DISCUSSION

A stand for the study of AM-cr with the possibility of direct and smooth starting has been developed. A methodology has been developed for setting different ramps for acceleration of the AM-cr in smooth start mode. The starting characteristics of the AM-cr are obtained at different starting modes. The possibility for optimizing the starting process depending on the load has been proven, in order to reduce the: energy consumption, starting current and mechanical shocks on the motor during start-up.

The following conclusions from graphical dependences can be made:

- the change of the stator current and the torque of AM-cr at direct start is abrupt, as the starting current reaches $6.I_N$ and the starting moment reaches $3.M_N$. This leads to: increased losses of active power; conditions for the occurrence of unfavourable, mechanical shocks on the electric drive; shortening the period of trouble-free operation of the motor and electric drive;

- in case of smooth start-up of AM-cr with reduced, supply voltage, the starting current is in the range of $(2 \div 4).I_N$ and the starting torque is in the range of $(0.71 \div 1.3).M_M$, depending on the selected voltage starting ramp;

75

- the motor sturt-up time mainly affects the starting, mechanical characteristics of the AM-cr. As the starting time t_R increases, an initial decrease is observed, followed by an increase in engine torque. The optimal rotation time is $t_R = 3s$, at which a constantly increasing torque is observed until the nominal value is established.

REFERENCES

1. Yakov V., Electromechanical devices and systems, TU – Sofia, 2010.
2. Dimitrov V., Laboratory system for tests of asynchronous motors with smooth start and stop, Mechanics, Transport and Communications, № 1378, b. 14, N 3/2, 2016,ISSN 2367 - 6620.
3. Dimitrov V., Development of a laboratory system for testing electric motors, Mechanics, Transport and Communications, № 1246, b. 13, №. 3/3, 2015, ISSN 1312 - 3823.
4. Djagarov N, Electric drive, TU–Varna, 2011.
5. Controls – Soft Starters and Solid - State Switching Devices, Siemens AG 2011.
6. Kostov I, Electric drive control, Sofia, 2014.
7. Petleshkov A., Stomanyarski N, Tzvetkova S., Petrova V., Study of the efficiency of electric drives of an asynchronous motor, Mechanics, Transport and Communications, b. 14, №. 1/3, 2018, ISSN 2367 - 6620.

RESEARCH OF AUTONOMOUS LOW POWER SUPPLY SYSTEM

Vasil Ivanov
E-mail: vasil_bi@abv.bg

ABSTRACT

The autonomous power supply system (APSS) is configured, connected to two independent direct current sources and to the low voltage public power supply. This creates a continuous mode of operation for consumers. The application of the gas station is for mountain and sea sites without access to a public network. The power supply is used in security, lighting and telecommunication facilities.

Key words: *the autonomous power supply system (APSS), accumulator batteries (AB), solar panels (SP), public electricity network*

INTRODUCTION

The architecture of APSS shown in Fig. 1 is composed of three independent energy sources: accumulator batteries (AB), solar panels (SP) and public electricity network [1]. The priorities for the directions of energy exchange between the input / output electrical circuits are set by a program from a central voltage inverter model FSP 3kVA.

Fig. 1. Central module-inverter, sources and consumer

- Parameters of the elements of the gas station:
- The solar panels SP are four with a power of 250pW each. They are in a mixed connection scheme and are fixed to the roof.
- The series-connected AB are two of 12V each, to double the voltage to 24V. The capacity of the AB has a nominal value of 280Ah.
- The inverter is FSP 3kVA Plus (24V) for single-phase voltage with the following parameters: a true sine wave frequency of 50 Hz and power of 3kVA.
- The inverter in the installation is connected to the low voltage public energy network and the consumers through fuses on the main panel.
- The intelligent part of the management of the inverter voltage includes a new generation digital signal processor (DSP) with basic algorithms of work:
- Its main function is to convert DC voltage into AC, by applying the law of PWM. It has a high conversion efficiency of up to 98%.
- The controller has an optimal algorithm for tracking the point of maximum power MPPT of the SP [2].
- Another important function is the stabilization of the DC voltage after SP (DC / DC step-down converter model) and a program for optimal charge / discharge mode of the AB.
- Screen analysis of the voltage inverter (DC / AC) operating modes.

The display in Fig. 2 is mounted on the front of the inverter and graphically shows the functional units and their electrical circuits. Below the display are LED indicators and function buttons for control and adjustment.

In the upper part of the display in Fig. 2 the current values of the input indicators (on the left) and the output values (on the right) are visualized in real time.
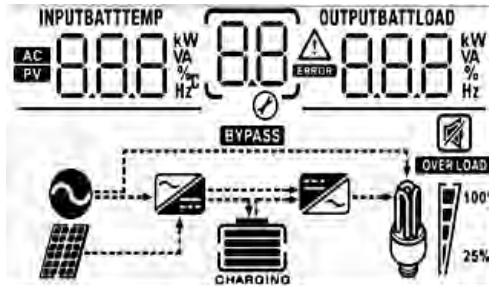
Fig. 2. Display for visualization of current parameters in modern models of voltage inverters

The lower part of Fig. 2 shows a mnemonic diagram of the possible combinations of connecting the components depending on the set mode of operation.

THEORETICAL PART

- **Management of the autonomous power supply system (APSS) regimes**

The intelligent part of APSS includes automatic selection of different algorithms for work. The stages of setting and monitoring of the basic input and output indicators are performed in two ways:
  - via the function keys on the built-in display;
  - installation of the software application on a personal computer.

The graphic interface (GUI) of the EA C consists of five sections:

A. Functional menu with a full set of navigation and adjustment tools;

B. Menu for quick access to sections of frequently used functions;

C. Communication port for connection to the inverter as a physical device;

D. Monitoring information from a user who does not have administrative rights to change the setting of the inverter mode parameters;

F. Main window for current information (monitoring) of the gas station:
  - takes into account the values of the main indicators of the inverter operation;
  - displays real-time basic operational information;
  - registers and records the data from the device and the nominal current information about the performance indicators of the inverter.

Fig. 3. Dialog box divided conditionally into five fields for system management

- Energy direction control between source and consumer:

The depicted five icons in Fig. 4 include: solar panel SP, rechargeable battery AB, DC / AC inverter and consumer [3].
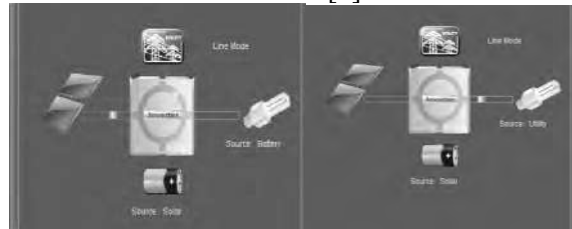

Fig. 4. Part of the dialog box of Fig. 3

The supervision of the operator for the direction of energy interchange in real time is visualized by "hilighting" the electrical connections of Fig.4. The interchange to the AB is a two-way executing algorithm for optimal charge / discharge mode. By "illuminating" the electrical connections, the dynamic change of the direction of movement of the power supply is visualized, depending on the operating mode.

▪ Operation of energy exchange directions.

The arrows in the images indicate the movement (exchange) of electricity between sources and loads.

Fig. 5. First energy mode, second energy mode, third energy mode

First power mode: Charging the AB from the SP or the network;

Second energy regime: The network supplies the load and charges the AB, as well as the SP during the day;

Third energy mode: SP and AB power consumers.

▪ Current parameters of the sources included in APSS.

Account: The voltage from solar panels (SP), voltage and battery capacity (AB) and mains voltage and frequency, etc.

Fig.6. Dialog boxes with instantaneous values for the activity of the sources in real time (on the left) and on the ranges of the nominal parameters (on the right)

The stability control is performed on the most important parameters of the voltage inverter: nominal output voltage and frequency.

▪ Principle of operation and settings through the " smart " software of the gas station.

The options for controlling the basic modes and parameters of the inverter are shown in Fig. 7 [4]:

Fig.7. Dialog box with settings for mode parameters

1. The voltage generated by the solar panels SP is converted by the inverter into alternating and priority power supply to the consumers. When the electricity produced by the JV is greater than the consumed, it is directed by the inverter controller to charge the rechargeable batteries AB.

2. In cloudy weather, the power generated by the SP is reduced or absent. Then the AB is automatically connected to the gas station in parallel as a second source and begins to give the accumulated energy to the consumers.

3. When the intensity of the solar radiation is low or at night and the batteries are discharged to the minimum of their capacity, the inverter automatically (for a period of 20mS) switches the supply of energy from the public electricity system to the electrical loads.

EXPERIMENTAL PART

- **Measurement results parameters**

In the process of experimentation, integrated monitoring of the main parameters by groups was applied:

1. Public electricity network: U network and f network;

2. Solar panels (SP): P SP and U SP;

3. Rechargeable batteries (AB): U AB, I charging and I discharging, capacity C AB in%;

4. Output energy indicators to consumers:

U output, f output, I output, S total and P active power and load in%;

▪ real-time measurements of the firmware data are stored in tables in interval of one hour for a period of 24 hours.
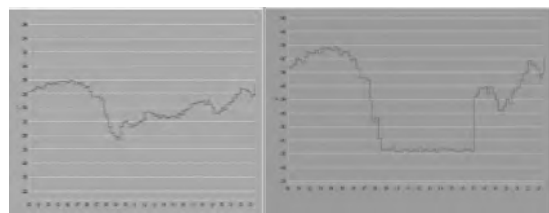

Fig. 8. Graphs of the change of the input $U_{rms} = 230V$. On the left is the mains voltage and on the right is after the inverter

In Fig. 8 there is a stable period (from 8 am to 5 pm) of operation of gas stations in inverter mode. Consumers are powered by solar energy from the SP.

▪ Diagram of the output mains frequency f observed in the period of operation as an inverter (right graph) with a stable frequency of 50 Hz.
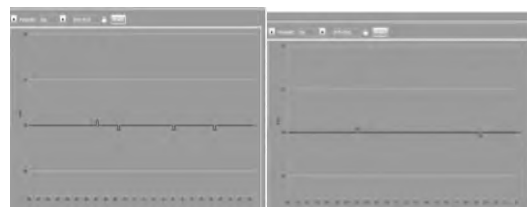

Fig. 9. Diagram of the frequency of the mains voltage $U_{circuit}$. The 50Hz variation on the left graphic has more "bounces" because the recording is from the public network
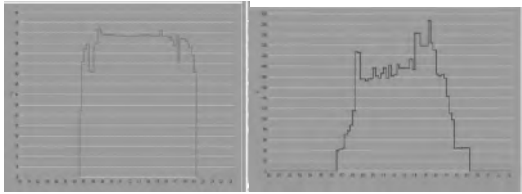
Fig. 10. Voltage graphs from solar panels USP in red and power PSP in blue; The recording was made in inverter mode
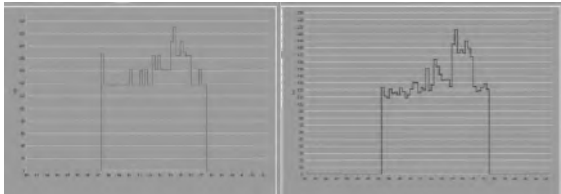

Fig. 11. Diagram of the total power S in red and the active P in blue, obtained from the operation of complex consumers
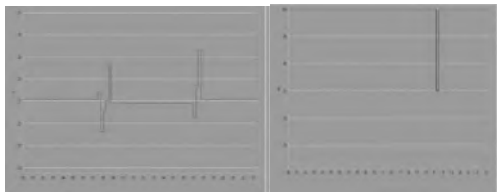

Fig. 12 . The diagram in red is for U_{AB} of AB charge-discharge and in blue for change of the capacity of AB C_{AB} in percentage
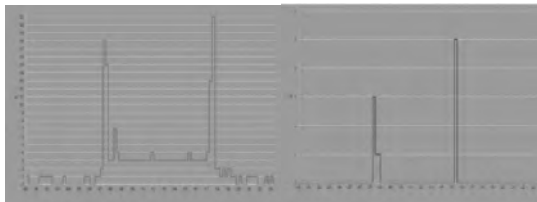

Fig. 13. The diagram in red is from the change of the charging current $I_{charging}$ of AB, and in blue from the change of the discharge current $I_{discharge}$

CONCLUSIONS

The results of the experimental research are related to periodic measurement of the input / output characteristics of the autonomous power supply system with a different number and type of electrical loads and determination of the optimal load. According to the data from the reports, it is possible to generate graphical dependences of the electrical parameters on certain periods of time, which can be used in practical laboratory classes.

▪ The tracking of the point of maximum power is set in the algorithm of the controller. In this way the operation of the solar generator is optimized and the maximum efficiency of the photovoltaic modules is guaranteed.

▪ The built-in software in the inverter allows monitoring of the input and output data and mode parameters, for a long period of time: days, months or a year. The information arrays from the records can be used in sample statistical analyses of changes in electrical parameters, temperature, and intensity of solar radiation during different months and seasons [5].

▪ Application of the implemented project

▪ The autonomous power supply system is connected to the electrical installation of the Laboratory of Electrical Engineering and Electronics in the Inorganic Chemistry Building of the University. One part of the gas station supplies the lighting installation, and the other capacities are switched on when energy is needed for the experiments.

▪ The Autonomous Power Supply System (ALS) is used in the teaching process for laboratory exercises in the disciplines "Electrical Engineering and Electronics", "Renewable Energy Sources", "Photovoltaic Systems", "Alternative Energy Sources", etc.

▪ The autonomous power supply system is used in design, research and experimentation, as well as an application in the development of diploma theses in the Master's programs in the specialties: Electrical Engineering and Electronics.

REFERENCES

[1] Materials from PhD dissertation "*Study of the influence of photovoltaic systems on electrical networks*", certificate № РУ-НС-2017-13, issued on 23.06.2017 to Vasil Borisov Ivanov, Ruse.

[2]. Ivaylo Stoyanov, Vasil Ivanov, Teodor Iliev, Hristo Ivanov, "*Yield and Performance Study of a 1MWp Grid Connected Photovoltaic System in Bulgaria*", Journal of Engineering Science and Technology Review X (X) (201X) ISSN: 1791-2377, doi:10.25103/ jestr.132.43, Research Article.

[3] Vasil Ivanov, "*Modeling of single phase inverter system in simulink software*", Annual of Assen Zlatarov university, Burgas, Bulgaria, 2020, V. XLIX (1)

[4] Vasil Ivanov, Ivaylo Belovski, „*Survey of the impact of the seasons over the effectiveness of solar panels*", Annual of Assen Zlatarov University, Burgas, Bulgaria, 2019, v. XLVIII (1), Book 1, page 96-98, 2019 Burgas 8010, Bulgaria,ISSN2603-3968.

[5] Ivaylo Belovski, Vasil Ivanov, "*Solar powered thermoelectric cooling system*", Assen Zlatarov University, Annual, Vol. XLVII, Book 1, page 101-104, 2018 Burgas 8010, Bulgaria, ISSN 2603-3968.

GENERALIZED NETS MODEL FOR PACKET FLOW V6.0

Liliya Staneva, Dimitar Iliev
E-mail: lanestieva@btu.bg

ABSTRACT

The article describes one of the methods of network protection using the packages of the RouterOS operating system of MikroTik. The method is based on the Routing package in RouterOS v.6 for network protection. The apparatus for generalized net is used for modeling and description of the processes. Generalized nets are one of the most popular techniques for describing processes in a formal and abstract way.

   Key words: *routing package, generalized nets, MikroTik*

INTRODUCTION

Many resources and efforts have been made in recent years to protect network security. The use of secure network devices that are difficult to penetrate through unwanted hacker attacks, are faster and therefore more powerful and at an affordable price for the user is a top priority in the companies providing these devices. This article discusses the equipment provided by MikroTik, which runs on the RouterOS network operating system. A generalized network model of one packet stream in RouterOS V.6 has been created, providing the necessary network protection.

The network operating system RouterOS [1] is designed as an easy-to-use tool for a number of configurations serving network communication. The use of the main functions, such as providing access to the Internet, forwarding through ports, and denying access to certain IP addresses, is achieved through a number of operations. The company also develops specialized packet flow diagrams needed to set up complex configurations and determine the origin of traffic in the router. Flow tracking diagrams are the basis for planning a process and service while finding real reasons why a configuration works or doesn't work. The main attention will be focused on the Packet Flow Diagram, which will be described by a generalized net model.

EXPOSITION

This article presents a generalized net model with a general structure for describing the flow of Routing packets based on the Packet Flow Diagram [2, 3]. The methodology for building generalized networks includes [4, 5, 6]:

   - building a static structure of the modeled process;

   - reflection of the dynamics of the modeled process;

   - description of the functionality of the modeled process for a certain period of time;

   - identification of the data of interest for the modeled function.

Routing flow tracking diagram (Fig. 1).

GENERALISED NET MODEL

A generalized net model with an introduced set of transitions has been developed (Fig. 2):

$$A = \{Z_1, Z_2, Z_3, Z_4, Z_5\}$$

where the transitions describe the following processes:

Z_1= "Pre-processing of the received package";

Z_2= "Deciding to route the received packet";

Z_3 = "The package is in the process of being forwarded";

Z_4 = "Package enters the process of building the connection";

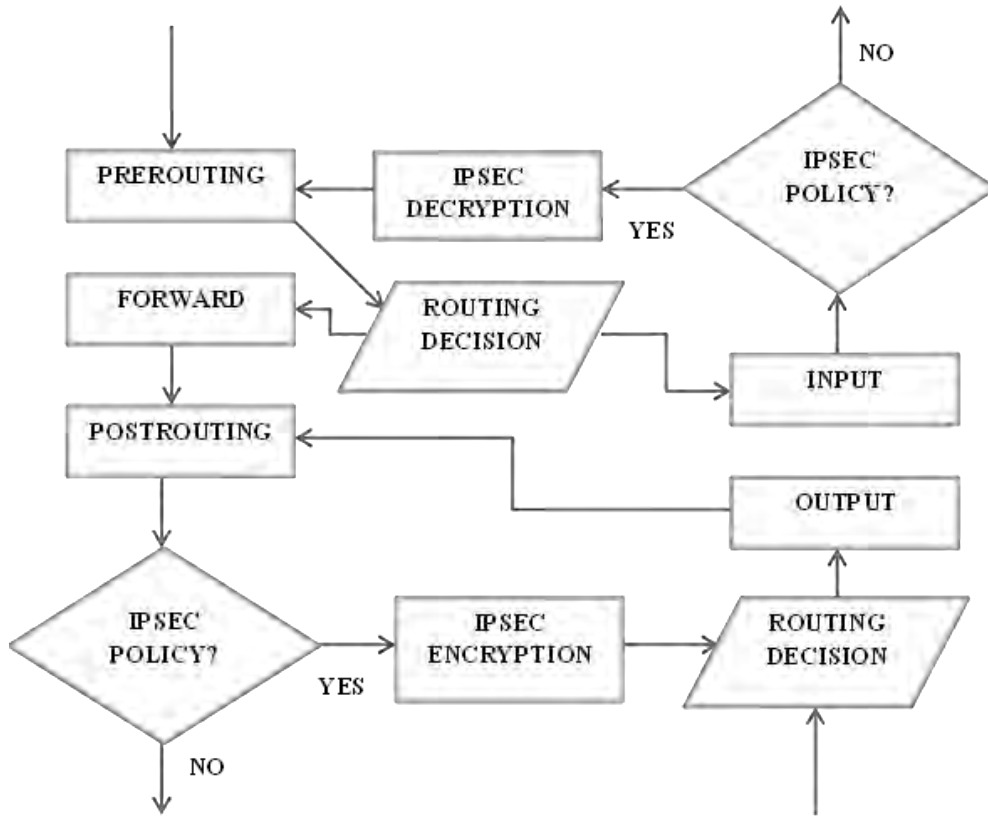Z_5 = "Package enters the output process".
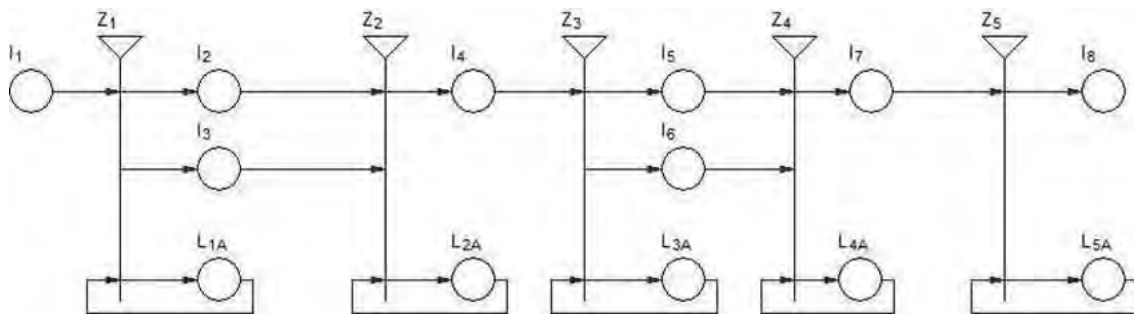
Fig. 1. Routing Diagram

Fig. 2 Generalized net model for processing the received packets

The transitions have the following description:

$$Z_1 = \langle\{l_1, L_{1A}\}, \{l_2, l_3, L_{1A}\}, R_1, \vee(l_1, L_{1A})\rangle$$

where:

$$R_1 = \begin{array}{c|ccc} & l_2 & l_3 & L_{1A} \\ \hline l_1 & false & false & true \\ L_{1A} & W_{1A,2} & W_{1A,3} & true \end{array}$$

$W_{1A,2}$ = "packet processed before routing"
$W_{1A,3}$ = "packet sent by connection tracking"

The token from position l_1 enters position L_{1A} and does not change its characteristics. The token from position L_{1A} is divided into two tokens,

which enter with positions l_2, l_3 and receive the characteristic "processing package".

$$Z_2 = \langle\{l_2, l_3, L_{2A}\}, \{l_4, L_{2A}\}, R_2, \vee(l_2, l_3, L_{2A})\rangle$$

where:

$$R_2 = \begin{array}{c|cc} & l_4 & L_{2A} \\ \hline l_2 & false & true \\ l_3 & false & true \\ L_{2A} & W_{2A,4} & true \end{array}$$

$W_{2A,4}$ – "Routing package available"

Tokens from position l_2 and l_3 enter position L_{2A} and do not change their characteristics. The token from position L_{2A} enters position l_4 and

83

receives the characteristic "packet routing decision has been made".

$$Z_3 = \langle \{l_4, L_{3A}\}, \{l_5, l_6, L_{3A}\}, R_3, \vee (l_4, L_{3A}) \rangle$$

where:

$$R_3 = \begin{array}{c|ccc} & l_5 & l_6 & L_{3A} \\ \hline l_4 & false & false & true \\ L_{3A} & W_{3A,5} & W_{3A,6} & true \end{array}$$

$W_{3A,5}=$ "Packet processed through filter circuit and Mangle"

$W_{3A,6}=$ "Package sent to calculation process"

The token from position l_4 enters a position L_{3A} and does not change its characteristics. The token from position L_{3A} enters positions l_5, l_6 and receives characteristics "verified value in TTL", and "available filtering and calculation package".

$$Z_4 = \langle \{l_5, l_6, L_{4A}\}, \{l_7, L_{4A}\}, R_4, \vee (l_5, l_6, L_{4A}) \rangle$$

where:

$$R_4 = \begin{array}{c|cc} & l_7 & L_{4A} \\ \hline l_5 & false & true \\ l_6 & false & true \\ L_{4A} & W_{4A,7} & true \end{array}$$

$W_{4A,7}$ – "forwarding package available "

The input tokens from position l_5 and l_6 enter position L_{4A}; after the transition the token l_7 coming out of position L_{4A}, has the current characteristic "the package is treated with a tree of tails and simple tails"

$$Z_5 = \langle \{l_7, L_{5A}\}, \{l_8, L_{5A}\}, R_5, \vee (l_7, L_{5A}) \rangle$$

where:

$$R_5 = \begin{array}{c|cc} & l_8 & L_{5A} \\ \hline l_7 & false & true \\ L_{5A} & W_{5A,8} & true \end{array}$$

$W_{5A,8} =$ "The received packet is safe for processing in the router"

The token from position l_7 enters L_{5A}, where it does not change its characteristics. The token from position L_{5A} enters position l_8, where it receives the characteristic "IPsec security packet processed".

CONCLUSION

A new approach is proposed to describe the modeling of the packet processing process in RouterOS with generalized nets. The model allows us to consider different stages of checking the incoming packets in the router, as well as to prevent any potential errors during the workflow.

REFERENCES

1. Boyadjiev A., "*Osnovi na Mikrotik routeros*", *izd*. "Za Bukvite", Sofia, 2016.
2. https://help.mikrotik.com/docs/display/ROS/Packet+Flow+in+RouterOS
3. https://wiki.mikrotik.com/wiki/Manual:Packet_Flow
4. Vardeva I., *Generalized Net Model of an Automated System for Monitoring, Analysing and Managing Events Related to Information Security*, Digital Transformation, Cyber Security and Resilience, Information & Security, vol. 43, numbers 1, 2 & 3 Digilience 2019 Sofia, Bulgaria, ISSN: 0861-5160 (Print), ISSN: 1314-2119 (Online), pp. 257-264.
5. Vardeva I., *How to motivate today's student in the discipline of computer networks with professional extracurricular training*, VIII International Scientific Conference modern cultural and educational space of humanities and social sciences, Russia, 2020, pp. 47-55.
6. Petrov Y., *Determining the area of the automobile tire contact footprint using generalized nets*, Annual of Assen Zlatarov University, Burgas, Bulgaria, 2020, v. XLIX, Book 1, pp. 79-81.

PROGRAM REALIZATION AND VISUAL SIMULATION OF K-MEANS CLUSTER ANALYSIS

Stanislav Popov, Todor Petkov, Veselina Bureva
E-mail: stani_popov@yahoo.com

ABSTRACT

At its core, machine learning is simply a way of achieving artificial intelligence. It is an application of the latter that enables systems to learn and advance based on experience. K-means clustering is one of the simplest and most popular unsupervised machine learning algorithms. MATLAB is used for the programming environment, and random numbers were generated for the input data. The result is related to the formation of the given number of clusters and the visual representation of the individual iterations during the clustering process.
Key words: *K-means clustering, artificial intelligence*

INTRODUCTION

Artificial intelligence is the wide branch of computer science that is specifically concerned with smart machines capable to perform specific tasks based on human intelligence.

Clustering is one of the main methods of gaining insight on the underlying nature and structure of data. The purpose of clustering is to organize a set of data into other clusters. One of the most used clustering algorithms presently is K-means, because of the easiness for interpreting its results and implementation.

The aim of this research is to analyze the process of the K-means algorithm step by step, using program realization and visual simulation in MATLAB in order to illustrate its operation.

DEFINITION OF K-MEANS CLUSTER ANALYSIS

In K-means cluster analysis, the distance of each unit to the centers of the individual clusters is taken into account, and the closest distance determines the affiliation of the unit to the respective cluster [1]. The method requires pre-determining the number of the clusters. The centers of these clusters can be known or estimated from the data. In addition, the centers can remain constant or be updated in the analysis process [2]. For relatively large aggregates, hierarchical clustering methods and random sampling data can be used for initial parameter definition.

The process of the algorithm is divided into several steps [3]:

1) Random k-points are selected, which are the starting centers of the clusters.

2) Each object is connected to the nearest cluster center.

3) The centers of the clusters are recalculated according to their current composition.

4) If the algorithm stop criterion is not met, return to step 2).

The minimum change in the root mean square error is usually chosen as the criterion for stopping the operation of the algorithm. Also, it is possible to stop the operation of the algorithm if in step 2) there are no objects to move from cluster to cluster. The disadvantage of the k-means algorithm is the need to specify the number of clusters for division [4].

PROGRAM REALIZATION OF K-MEANS ALGORITHM IN MATLAB

A program realization of the k-means cluster analysis is presented using MATLAB. For this purpose, the proposed variant is with random numbers, united in 5 classes with 10 elements in each as the aim is to find the centers of the clusters. The functions used in the program implementation are the following: centroide.m (calculates the centers), class5.m (creates a set of 5 classes), plot_centroide.m (plots the centers), plot_linear.m (plots the lines from the cluster elements to the centers), plott.m (displays the

whole simulation) and k-means_random.m (combines the rest of the functions and starts the iterative action of the algorithm.

Fragments of the programming code for each function are presented in the following page.

- K-means_random.m:

```
low = 1;
high = size(x,1);
centres = zeros(k,size(x,2));
index = zeros(1,k);
for var = 1:k
index(var) =   round(low   +   (high   -
low)*rand);
centres(var,:) = x(index(var),:);
end
classes = zeros(high,1);
var_cond = 1;
W = 1;
while W
dist = zeros(high,k);
   . . .
        ant_class = classes;

    for var = 1:high
        [~,index] = min(dist(var,:));
        classes(var) = index;
    end
      colors = rand(k,3);
   . . .
        new_class = classes;
      for c = 1:k
        y = x(classes == c,:);
        centres(c,:) =    sum(y)/size(y,1);
    end
      if ant_class == new_class
        W = 0;
    end
    if var_cond > max_it
W = 0;
end
var_cond = var_cond + 1;
end
classes = new_class;
num_it = var_cond;
figure(1);
. . .
```

- Centroide.m:

```
function centres = centroide(x,classes)
   k = ver_classes(classes);
   centres = zeros(k,size(x,2));
     for c = 1:k
     y = x(classes == c,:);
     centres(c,:) = mean(y);
   end
```

end

- Class5.m:

```
function x = class5(N)
a = 5 * [randn(N,1) + 5, randn(N,1) + 5];
b = 5 * [randn(N,1) + 5, randn(N,1) - 5];
c = 5 * [randn(N,1) - 5, randn(N,1) + 5];
d = 5 * [randn(N,1) - 5, randn(N,1) - 5];
e = 5 * [randn(N,1), randn(N,1)];
x = [a;b;c;d;e];
end
```

- plottCentroide.m:

```
function plottCentroide(c)
 plot(c(:,1),c(:,2),'mx','LineWidth',2,...
        'MarkerEdgeColor','r',...
        'MarkerFaceColor','r',...
        'MarkerSize',10);
end
```

- plott_linear.m:

```
function plott_linear(x,classes,centres)
n = length(classes);
figure(1);
hold on;
for i = 1 : n
pos = classes(i);
plot([x(i,1),centres(pos,1)], [x(i,2),
centres(pos,2)],'g--');
pause(0.05);
end
end
```

- plott.m:

```
function plott(x,classes,colors)
n = length(classes);
figure(1);
 . . .
for i = 1 : n
p = plot(x(i,1), x(i,2),'mx','LineWidth',3);
set(p, 'color', colors(classes(i),:))
end
end
```

VISUAL SIMULATION OF THE ALGORITHM

The visual simulation of the clustering process is made through the plott.m, plott_linear.m and plottCentroide.m functions. When the simulation is started, each iteration of

the algorithm is presented by graphical animation (static pictures are shown in the article).

With a maximum number of iterations equal to 6 and a number of clusters equal to 5, the results shown in Fig. 1, 2 and 3 (next page) are obtained.
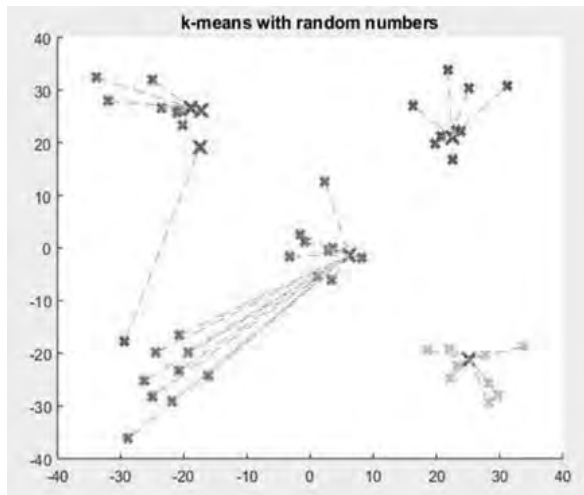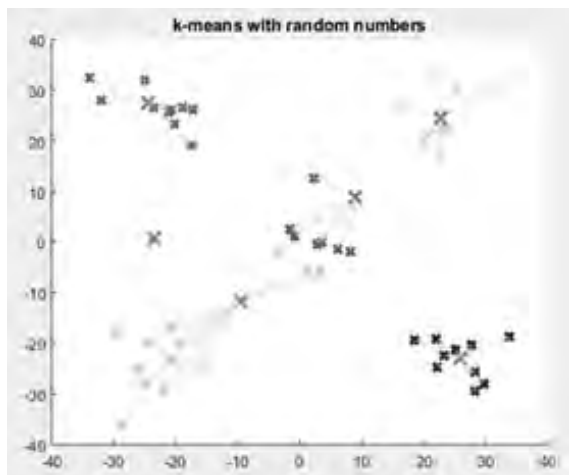

Fig. 1 Iteration one
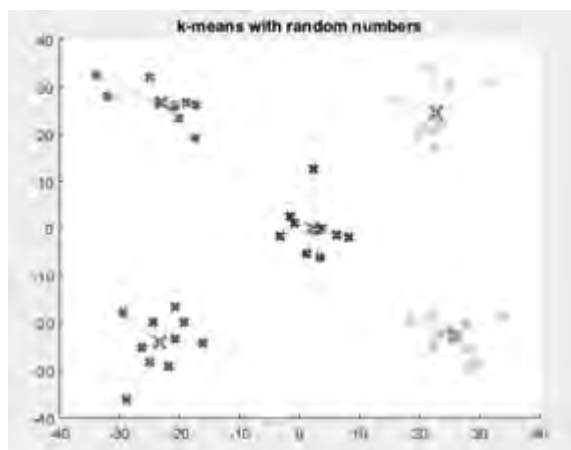

Fig. 2 Iteration two.

Fig. 3 Iteration three

With the parameters set at the beginning, the algorithm ends after 3 iterations (out of a maximum of 6). As can be seen in the graphs, the center of the clusters is marked with "X", the random numbers that must be related to one of the clusters are marked with "*" and their affiliation is shown with "- - -". The whole visualization of the operation of the algorithm is performed by the program code.

In Fig. 3, the five formed clusters can be seen with centers as follows:

- 24.6767372846014, -24.4336054611274;
- 0.471178593955773, -1.10496173346548;
- 25.8047635903735, 22.2068631421341;
- -22.3858309083016, 22.8223928202951;
- -25.1606687149199, -26.5989557975283.

The algorithm finishes in three iterations and divides the data correctly according to the initial criteria.

CONCLUSION

In the current paper a program realization of the K-means cluster analysis is presented. Moreover, the iteration steps of the algorithm are also shown as separate figures, depicting the way how the clusters and their centers are formed. This is realized in MATLAB and the most important sections of the programming code are included in the article, which leads to a better understanding of the algorithm operation.

ACKNOWLEDGEMENTS

REFERENCES

1. Menaga D., Saravanan S., Application of Artificial Intelligence in the Perspective of Data Mining, In: Artificial Intelligence and Data Mining 1st Ed., Academic Press, February 2021, pp. 44-45.
2. Ahmed M., Seraj R., Islam S. The k-means Algorithm: A Comprehensive Survey and Performance Evaluation. Electronics, 2020, 9.1295.10.3390/electronics9081295.
3. Singh R., Bhatia M., Data clustering with modified k-means algorithm. In: 2011 International Conference on Recent Trends in Information Technology (ICRTIT), 3-5 June 2011, Chennai, India :IEEE, pp. 717-721.

4.Moertini V., Venica L., Enhancing parallel k-means using MapReduce for discovering knowledge from big data, In: IEEE International Conference on Cloud Computing and Big Data Analysis, 5-7 July 2016, China: IEEE, 2016, pp 81-87.

CHOICE OF AN ALTERNATIVE FOR INCORPORATION OF DECENTRALIZED SOURCES INTO SMART GRIDS

Mehmed Kadir Hasan
E-mail: mehmedkadirhsn70@gmail.com

ABSTRACT

A methodology for selection of an optimal alternative for connecting decentralized energy sources to smart electrical distribution grids has been proposed. The criteria and the limiting conditions for carrying out the optimization have been substantiated. Variants of connection of decentralized sources to a distribution network have been considered. The method of Pareto optimality has been applied for each of the identified options according to the selected criteria. The obtained results allow to choose the optimal alternative for incorporation of decentralized producers to smart electric grids.

Key words: *smart grid, decentralized energy sources, Pareto-optimal solutions*

INTRODUCTION

A modern trend in the development of power systems is the construction of Smart grids (SGs). The introduction of modern equipment and new technologies, of facilities built on the basis of power electronics, means of communication, computerization and control allows us to construct electrical networks on a fundamentally new basis [1-4].

According to the commonly accepted definition, a smart grid is an electrical network, meeting the requirements for energy efficient and economical operation of power systems with coordinated control and two-way interconnection between its elements: power plants, sub-stations, power lines, storage systems and electricity consumers [5]. The predominant part of the requirements for the smart grids are fulfilled in the electrical networks for high and ultra-high voltage, but in the distribution networks for low and medium voltage, where consumers have unilateral power supply, this problem awaits a solution.

The most suitable generating sources, which can provide the bilateral supply for consumers of low and medium voltage electric networks are built on the basis of renewable energy resources (RES), i.e. decentralized generation (DG). A variant study of the ways to connect decentralized energy sources to electric networks is being conducted. The choice of an alternative

for connecting a decentralized generating source to a smart distribution grid depends on the magnitude of the connected power and reduces to consideration of the following possible technical solutions [1,2]:
- connection to a low-voltage (LV), supplying closely located consumers;
- transformation from low voltage (LV) to medium voltage (MV) and connection to the medium-voltage network;
- connection to a high-voltage (HV) network.

By applying the mathematical theory of games, in works [5,6] relevant criteria are justified and a methodology and software are developed for selection of an optimal alternative for connection of DG to an electrical network. The proposed methodology offers a mathematical apparatus, which objectively chooses an alternative based on pre-justified criteria after expert assessment of their significance.

The methodology for finding the optimal option to connect a DG source to an electrical network by desirability function is recommended for practical calculations and comparative analysis at the design stage [7].

This paper aims to develop a methodology for choosing the optimal alternative for joining a DG source to a smart grid, using the mathematical methods of multi-criteria optimization.

CRITERIA FOR CHOOSING THE OPTIMAL ALTERNATIVE FOR INCORPORATION OF A DG SOURCE INTO SMART DISTRIBUTION GRIDS

The accepted here criteria for selection of the optimal option for connecting a DG source to a distribution smart grid are [5,6]:
- discounted costs;
- energy efficiency;
- throughput capacity of the power lines.

Discounted costs are a major factor in evaluating the different alternatives for joining decentralized energy sources (DES) to a smart grid. The discounted costs R_D are expressed by the equation [8]:

$$R_D = \sum_{t=1}^{T_c} \sum_{i=1}^{n} K_{it} \alpha^{t-1} + \sum_{t=1}^{T_c} \sum_{i=1}^{n} \sum_{j=1}^{m} C_{ijt} \alpha^{t-1}, \qquad (1)$$

where K_{it} is the investment in the i^{-th} element of the scheme in the year t; T_c - the period of operation; n - the number of the elements in the scheme; m - the number of the different types of operational costs; C_{ijt} – the operational costs in the i^{-th} element of the scheme of j-ˉtype for the year t; $\alpha = 1/(1+r)^t$ - is the discount coefficient; t - the step in the calculation; T - the calculation period; r - the discount rate.

The operational costs C_{ijt} in the i^{-th} element of the electrical networks consist of: $j=1$ - maintenance and repair; $j=2$ - reconstruction, modernization, strengthening of sections in order to increase the throughput capacity, etc.; $j=3$ – coverage of the losses of active power in the elements of the electrical net-works.

$$C_{ijt} = \sum_{j=1}^{3} C_{it} = p_1 K_{it} + p_2 K_{it} + (\Delta P_{max} \tau \beta)_{it}, \quad (2)$$

where p_1, p_2 are the standardized values of the operational costs for maintenance and reconstruction of the electrical networks respectively; ΔP_{max} - the active power losses under a maximum load mode; τ - the fictitious duration of the maximum power losses; β - the price of electricity.

Energy efficiency means any reduction of power and electricity losses. Therefore, for each of the studied options, the power losses, which are the second criterion, are evaluated.

The HV distribution networks are open and branched. In general, the power losses $\Delta P_k + j\Delta Q_k$ in these networks for each section k are determined by the equations [8], [9]:

$$\Delta P_k = \frac{\left(\sum_{i=k}^{n} P_i\right)^2 + \left(\sum_{i=k}^{n} Q_i\right)^2}{U_н^2} R_k; \Delta Q_k = \frac{\left(\sum_{i=k}^{n} P_i\right)^2 + \left(\sum_{i=k}^{n} Q_i\right)^2}{U_н^2} X_k. \qquad (3)$$

where P_i and Q_i are, respectively, the active and reactive power flowing through the section; U_n - the nominal voltage; R_k and X_k - the active and inductive resistance of the k- section of the power line; n - the number of sections in the distribution network.

The total power losses for the whole branch $\Delta \dot{S} = \Delta P + j\Delta Q$ are determined by summing the power losses for each section:

$$\Delta \dot{S} = \Delta P + \Delta Q = \sum_{k=1}^{n} \Delta P_k + \sum_{k=1}^{n} \Delta Q_k. \qquad (4)$$

The *throughput capacity of the power lines* needs to be assessed since the LV and MV distribution networks are dimensioned before connecting the DG sources to them. For each branch of the electrical network the flowing current I must be less than the permissible current I_d.

$$I < I_d. \qquad (5)$$

METHODOLOGY FOR CHOOSING THE OPTIMAL ALTERNATIVE FOR CONNECTING DG SOURCES TO SMART DISTRIBUTION GRIDS

The methodology requires the following workflow:
- **Step 1** - the possible alternative options for connecting DG sources to a smart grid are compiled. For instance, for the scheme in Fig. 1 these options are:
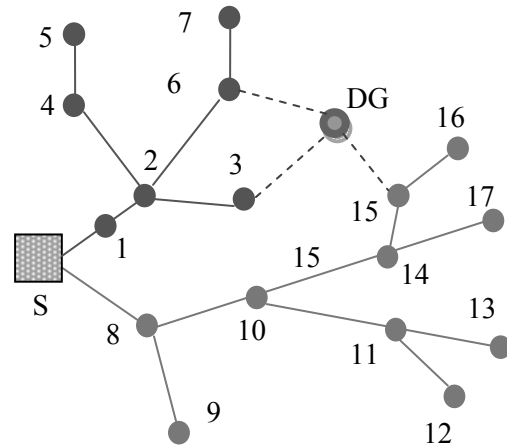

Fig. 1 Options for connecting a DG source to a smart grid: S - power-supplying sub-station; 1-17 - consumer nodes; DG - decentralized source

- Alternative option 1 - connection of a renewable energy source (RES) to node 3;

■ Alternative option 2 - connection of a RES to node 6;

■ Alternative option 3 - connection of a RES to node 15;

● **Step 2** - the criteria for choosing the optimal alternative for connection of DG sources to a distribution smart grid are substantiated: criterion 1 - discounted costs; criterion 2 - energy efficiency; criterion 3 – throughput capacity.

● **Step 3** - The optimization problem is solved with the set of target parameters or the vector criterion $\mathbf{F}(x) = [F_1(x), \ F_2(x), \ ..., \ F_m(x)]$, which, in this case, is formed by two vectors: $F_1(x)$ - discounted costs; $F_2(x)$ - energy efficiency. The third criterion (throughput capacity) is a limiting condition for the optimization.

The solution is considered optimal according to Pareto, if its change can improve more than one target function without worsening the others. In multi-criteria optimization two target functions must be minimized in accordance with the two specific criteria (discounted costs and power losses), making up the vector criterion. The formulation of the vector optimization problem with constraints on the parameters is:

$$\text{opt}_{x \in X} f(x), \qquad (6)$$

where:

$$f(x) = [f_1(x), f_2(x)], \qquad (7)$$

The agreed optimality meeting the two criteria is based on the principle of Pareto-optimality [10,11].

The algorithm for constructing the reachable set and the set of Pareto-optimal points consists of the following:

■ construction of the set of reachable values of the criteria;

■ introduction of the interval constraints x_{min} and x_{max};

■ generation of random points in the permissible parametric range and calculating the criteria in them;

■ depiction of the reachable criteria set;

■ obtaining results from the Pareto selection;

■ representation of the Pareto-optimal set in the criteria space.

● **Step 4** - Calculations for each of the identified alternative options shown in Fig.1. are performed.

● **Step 5** – Choice of an optimal alternative for connecting a DG source to a smart grid.

The problem to be solved seeks the option with minimal costs and power losses in compliance with the limitations for the capacity of the branches of the electrical network. The calculations are performed with specially developed software according to the proposed methodology. The results from the performed calculations, concerning connection of a DG source with a power of 300 kW to a smart grid, show the ratio in relative units, respectively:

• for the alternative option 1: 0.31;
• for the alternative option 2: 0.42;
• for the alternative option 3: 0.37.

The results from the conducted by the developed methodology numerical experiment for connecting DG sources with powers of 600, 900 and 1200 kW, are presented in Fig. 2.
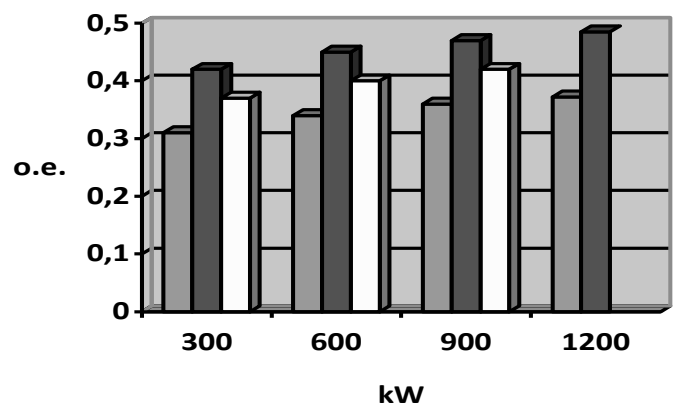

Fig. 2 Results from the conducted numerical experiment

Option 1   Option 2   Option 3

From the performed calculations it turns out that option 1 is the optimal one.

CONCLUSIONS

The criteria for choosing the optimal option for connecting a DG source to a smart distribution grid have been substantiated. These are the discounted costs and the power losses. The limitation in solving the optimization problem for connecting a DG source to a smart grid is the throughput capacity of the branches in the electrical network.

The developed methodology allows to choose the optimal way of joining a DG source, applying the mathematical method of multi-criteria optimization.

REFERENCES

1. Nedelcheva S.I., *Impact of decentralized energy sources on distribution networks*, Sofia, TU-Sofia Publishing House, 2006.
2. Nedelcheva S.I., *Electrical Networks and*

Systems with Decentralized Generating Sources, Sofia, TU-Sofia Publishing House, 2018.

3. Bakardjieva J. *Concept for restructuring medium-voltage distribution networks*. Journal of Notices of TU-Sliven, ISSN 1312-3920, № 4, 2012.

4. Andonov A., J. Bakardjieva. *Selection of partition nodes in medium voltage power distribution networks*. Indian journal of applied research, ISSN - 2249-555X, fev.2014.

5. Hasan M.K., *Optimal configuration of smart electrical distribution networks*. Dissertation. TU-Sofia, 2020.

6. Nedelcheva S.I., M.I.Matsankov, M.K.Hasan, *Choice of an optimal variant for incorporation of decentralized energy sources into electrical networks*. Journal of Multidisciplinary Engineering Science and Technology, ISSN 2458-9403, Reg. No JMESTN42353324, JMEST, Volume. 7, Issue. 4 April – 2020. www.jmest.org

7. Hasan M.K., *Variant study of the connection of decentralized generating sources to the electricity distribution network*. ISSN 1312-3920, Journal of Notices of TU-Sliven, №1, 2021.

8. Andonov AG, YN Bakardjieva, *Criteria for selection of an optimal configuration and a sectioning unit in the branches of a medium-voltage distribution network*, Journal of Energetica, № 6, 2012.

9. Nedelcheva SI, *Electrical Networks*, Sofia, Published by TU-Sofia, 2005.

10. Statnikov, R.B., J.B. Matusov, *Multicriteria Optimization and Engineering*, Chapman & Hall, New York, 1995.

11. Lotov A.V., *Pareto frontier visualization in multicriteria optimization problems*, Moscow Institute of Physics and Technology, 2013
.

GENERALIZED NETS MODEL FOR MARKING PACKETS FOR FURTHER PROCESSING

Ivelina Vardeva, Stoyan Dimitrov
E-mail: ivardeva@btu.bg

ABSTRACT

The article describes the mangle method used to mark packets and connections, as well as several special changes that can be applied to network traffic passing through the MikroTik firewall. The apparatus for generalized networks was used to describe the processes of the method. Generalized networks are used by means of constructing flexible and structured models of systems in which time-parallel processes consisting of multiple interacting components take place.
Key words: marking package, mangle rule, generalized net

INTRODUCTION

The mangle rule is used for packet and connection marking as well as a few special changes that can be applied to traffic passing through the MikroTik firewall.

Mangle rule is a kind of 'marker' that marks packets for future processing with special marks. Many other facilities in RouterOS make use of these marks, e.g. queue trees, NAT, routing. They identify a packet based on its mark and process it accordingly. The mangle marks exist only within the router, they are not transmitted across the network.

In the present research we develop Generalized Net [1, 3] models for marking packets for further processing. Indexed matrices are used to describe the states of the token [2]. The generalized network is built of many transitions, containing conditions under which the nuclei pass from the input to its output places [1, 3].

EXPOSITION

The main functions that are available there are to place special marks on packages or links. Depending on the type of marking, bookmarks can be used for other services within the router itself. For example, packet marking, links, and routing marks can be used as filter conditions, packet marking can be used in Queues quality management or QoS, and routing marks in routing tables. Under the terms of the Mangle policy, predefined chains are also available that determine when to place the marker. The chains are:

• Forward - marking is performed before a filter in the forward chain;

• Input - marking is performed before a filter in the input circuit;

• Output - marking is performed before a filter in the output circuit;

• Postrouting - marking is performed before a filter in the src-nat circuit;

• Prerouting - marking is performed before a filter in the dst-nat circuit;

Diagram mangle rule for packet and connection marking is shown in Fig. 1.

The actions that can be performed after creating appropriate conditions are twenty, and those that place markers are:

• mark-connection - puts a marker, which is set to the parameter new-connection-mark, on the whole connection, for which compliance is found in the conditions;

• mark-packet - places a marker, which is set to the new-packet-mark parameter, on each package for which compliance with the conditions is found;

• mark-routing - sets a marker that is set to the new-routing-mark parameter. Such tokens are used in managing the routing process through policies.
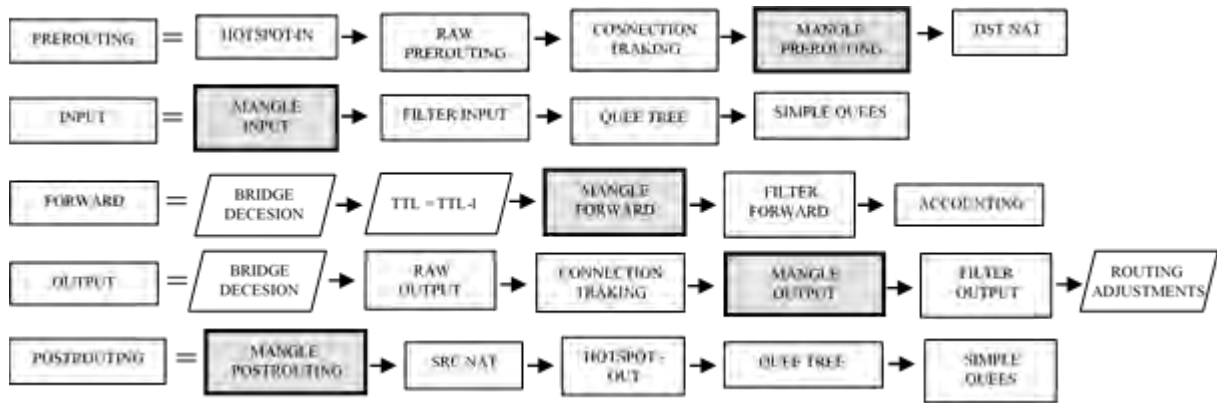
Fig.1. Diagram mangle rule for packet and connection marking

This article presents a model described forward chain when using mark-connection and mark-packet. Rules must first be applied to mark the required connections, and then a rule must be executed to mark the packets in them [4, 5, 6]. Thus, it will not be necessary to process all traffic by the packet marking rule presented in Table 1.

Table 1. Packet marking rule

```
/ip firewall mangle
add action=mark-connection chain=forward connection-state=new src-address=192.168.100.0/24 \
passthrough=yes new-connection-mark=netN
add action=mark-packet chain=forward connection-mark=netN new-packet-mark=clients-netN \
passthrough=yes
```

Thus, the first rule checks the IP header and look for compliance in the new requests, adding a connection token in those for which there is compliance. The next rule no longer checks the IP header of each packet, but will simply check the connection token and mark the packets if it finds a match. The latest action added by MikroTik in Mangle is called route: its function is to redirect packets to the IP address specified in the rule on the next router, ignoring the normal routing process. The route action can only be used with the prerouting circuit because it works before the routing process decides.

As illustrated in Fig. 2, we study a GNs model containing four transitions, which correspond to the following aspects of the above-described mangle rule for forward chain:
$A = \{Z_1, Z_2, Z_3, Z_4, Z_5, Z_6\}$,
where the transitions describe the following processes:
Z_1= "Represents the chain forward";
Z_2= "Represents the bridge decision";
Z_3= "Represents the TTL";
Z_4= "Represents the mangle forward";
Z_5= "Represents the filter forward"
Z_6= "Represents the accounting"
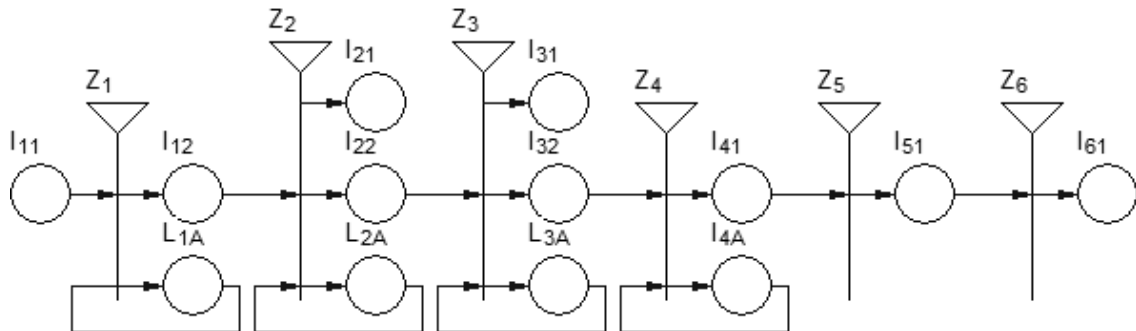
GENERALISED NET MODEL

Fig. 2 Generalized net model for processing the received packets

In place l_{11} token α with characteristic "received package for chain forward".

What follows is a description of the transitions of the net.

The transitions have the following description:

$Z_1 = \langle \{l_{11}, L_{1A}\}, \{l_{12}, L_{1A}\}, R_1 \vee (l_{11}, L_{1A}) \rangle$,
Where:

$$R_1 = \begin{array}{c|cc} & l_{12} & L_{1A} \\ \hline l_{11} & false & true \\ L_{1A} & W_{L_{1A},l_{12}} & true \end{array}$$

$W_{L_{1A},l_{12}} =$ "there is a package from a forward chain".

When the predicate $W_{L_{1A},l_{12}}$ has truth value "true" the α token from place l_{11} enters place L_{1A} with characteristic "*request to forward chain*".

$Z_2 = \langle \{l_{12}, L_{2A}\}, \{l_{21}, l_{22}, L_{2A}\}, R_2 \vee (l_{12}, L_{2A}) \rangle$,
Where:

$$R_2 = \begin{array}{c|ccc} & l_{21} & l_{22} & L_{2A} \\ \hline l_{12} & false & false & true \\ L_{2A} & W_{L_{2A},l_{21}} & W_{l_{2A},l_{22}} & true \end{array}$$

$W_{L_{2A},l_{21}} =$ "bridge decision is rejected",

$W_{l_{2A},l_{22}} =$ "bridge decision is allowed".

In place l_{12} token α obtains the characteristic "available is package from bridge decision". After transition α token enters l_{22} the place obtains the characteristic "*allowed incoming package*".

$Z_3 = \langle \{l_{22}, L_{3A}\}, \{l_{31}, l_{32}, L_{3A}\}, R_3 \vee (l_{22}, L_{3A}) \rangle$,

Where:

$$R_3 = \begin{array}{c|ccc} & l_{31} & l_{32} & L_{3A} \\ \hline l_{22} & false & false & true \\ L_{3A} & W_{L_{3A},l_{31}} & W_{l_{22},l_{32}} & true \end{array}$$

$W_{L_{3A},l_{31}} =$ "verified TTL is reject".

$W_{L_{3A},l_{32}} =$ "verified TTL is allowed".

In place l_{22} token α obtains the characteristic "verified the incoming package from TTL". After transition α token enters l_{32} the place obtains the characteristic "allowed TTL from package".

$Z_4 = \langle \{l_{32}, L_{4A}\}, \{l_{41}, L_{4A}\}, R_4 \vee (l_{32}, L_{4A}) \rangle$,

Where:

$$R_4 = \begin{array}{c|cc} & l_{41} & L_{4A} \\ \hline l_{32} & false & true \\ L_{4A} & W_{L_{4A},l_{41}} & true \end{array}$$

$W_{L_{4A},l_{41}} =$ "packed is marked".

In place l_{32} token α obtains the same characteristic "allowed TTL from package". When the predicate $W_{L_{4A},l_{41}}$ has truth value "true" the α token from place l_{41} enters place with characteristic "*marked packed with mangle rule*".

$Z_5 = \langle \{l_{41}\}, \{l_{51}\}, R_5 \vee (l_{41}) \rangle$,
Where:

$$R_5 = \begin{array}{c|c} & l_{51} \\ \hline l_{41} & W_{l_{41},l_{51}} \end{array}$$

$W_{l_{41},l_{51}} =$ "filter forward is available".

When the predicate $W_{l_{41},l_{51}}$ has truth value "true" the α token from place l_{51} enters place with characteristic "*proceed filter forward*".

$Z_6 = \langle \{l_{51}\}, \{l_{61}\}, R_6 \vee (l_{51}) \rangle$,
Where:

$$R_6 = \begin{array}{c|c} & l_{61} \\ \hline l_{51} & W_{l_{51},l_{61}} \end{array}$$

$W_{l_{51},l_{61}} =$ "accounting is available".

When the predicate $W_{l_{41},l_{51}}$ has truth value "true" the α token from place l_{61} enters place with characteristic "*accounting*".

CONCLUSION

Creating complex tasks related to traffic authorization, routing through policies, etc. impose a requirement to work with various elements of RouterOS. This type of tasks requires not only to achieve the desired result, but also to optimize the available resources to attain good results.

The presented GN model describes the place of special marks on packages or links depending on the type of marking or bookmarks. The developed model can help examination, analyzing and optimizing the flowing processes in exchanging such data in the router rules.

REFERENCES

1. Atanassov K., Generalized nets, World Scientific, Singapore, 1991
2. Atanassov K., Index Matrices: Towards an Augmented Matrix Calculus, Springer, Berlin, 2014

3. Atanassov K., On Generalized Nets Theory, "Prof. M. Drinov" Academic Publ. House, Sofia, 2007

4. Boyadzhiev D., MikroTik RouterOS Basics (book), FOR THE LETTERS, ISSN: 978-619-185-252-9, 2016, Sofia

5. Petrov Y., Determining the area of the automobile tire contact footprint using generalized nets, Annual of Assen Zlatarov University, Burgas, Bulgaria, 2020, v. XLIX

6. Staneva, Liliya Anestieva. "Minimising using the Method of Quine-McCluskey with Generalised Nets." 2019 29th Annual Conference of the European Association for Education in Electrical and Information Engineering (EAEEIE). IEEE, 2019